Energy & Environmental Science

ROYAL SOCIETY OF CHEMISTRY

REVIEW

View Article Online
View Journal | View Issue

Cite this: *Energy Environ. Sci.*, 2021, **14**, 3352

Up-scalable emerging energy conversion technologies enabled by 2D materials: from miniature power harvesters towards grid-connected energy systems

Konstantinos Rogdakis, *[ab] Nikolaos Karakostas[a] and Emmanuel Kymakis *[ab]

Breakthrough discoveries in high-throughput formulation of abundant materials and advanced engineering approaches are both in utter need as prerequisites for developing novel large-scale energy conversion technologies required to address our planet's rising energy demands. Nowadays, the rapid deployment of Internet of Things (IoT) associated with a distributed network of power-demanding smart devices, concurrently urges for miniaturized systems powered by ambient energy harvesting. Graphene and other related two-dimensional materials (GRM) consist a perfect fit to drive this innovation owing to their extraordinary optoelectronic, physical and chemical properties that emerge at the limit of two-dimensions. In this review, after a critical analysis of GRM's emerging properties that are beneficial for power generation, novel approaches are presented for developing ambient energy conversion devices covering a wide range of scales. Notable examples vary from GRM-enabled large-scale photovoltaic panels and fuel cells, smart hydrovoltaics and blue energy conversion routes, to miniaturized radio frequency, piezoelectric, triboelectric, and thermoelectric energy harvesters. The insights from this review demonstrate that GRM-enabled energy harvesters, apart from enabling the self-powered operation of individual IoT devices, have also the potential to revolutionize the way that grid-electricity is provided in the cities of the future. This approach is materialized by two complementary paradigms: cross-coupled integration of GRM into firstly, a network consisted of a vast number of miniaturized, in-series-connected harvesters and secondly, into up-scaled, multi-energy hybrid harvesters, both approaches having the potential for on-grid energy generation under all-ambient-conditions. At the end of the discussion, perspectives on the trends, limitations and commercialisation potential of these emerging, up-scalable energy conversion technologies are provided. This review aims to highlight the importance of building a network of GRM-based, cross-scaled energy conversion systems and their potential to become the guideline for the energy sustainable cities of the future.

Received 23rd December 2020,
Accepted 10th May 2021

DOI: 10.1039/d0ee04013d

rsc.li/ees

Broader context

An aggressive technological deployment will soon affect the planet's energy landscape, demanding a swift transformation from the predominant use of fossil fuels to that of renewable energy installations. With its concurrent arrival the Internet-of-Things (IoT) promises to create a largely distributed global network of wireless sensors and wearables connected to the "cloud": Humankind is exploiting new technological platforms able to impact sustainable development and prosperity toward Industry 4.0 revolution. These platforms will create a robust demand of energy for their supply with power, making a battery-free operation mandatory together with low manufacturing cost and reduced environmental impact. Herein, we review recent the research progress on novel energy conversion systems enabled by Graphene and other related two-dimensional materials (GRM). It is shown that GRM-enabled "harvesters" span across a wide range of scales. The demonstrated prototypes include self-powered miniaturized IoT devices, which convert electromagnetic radiation, heat, vibrations, solar power, and water-dynamics energy into electricity, to large scale renewable energy installations. A step further towards on-grid electricity generation in smart cities of the future is highlighted by a two-fold complementary approach: use GRM to establish large networks consisted of multiple, in-series-connected miniature energy harvesters or develop up-scaled multi-energy harvesters. In addition, challenges and perspectives for future research are also highlighted, toward energy sustainable communities.

[a] *Department of Electrical & Computer Engineering, Hellenic Mediterranean University (HMU), Heraklion 71410, Crete, Greece. E-mail: krogdakis@hmu.gr, kymakis@hmu.gr*
[b] *Institute of Emerging Technologies (i-EMERGE) of HMU Research Center, Heraklion 71410, Crete, Greece*

1. Introduction

The planet's energy landscape must be transformed from the predominant use of fossil fuels to that of emerging energy

conversion technologies that will enable the reduction of CO_2 emission that has been associated with climate change. In this respect, the European Commission's Green Deal initiative proposes a new development strategy that aims to preserve the planet for future generations.† This strategic long-term vision for climate neutral societies requires a drastic reduction of greenhouse gas emissions by 2050.‡ Central role toward this development is expected to be played by emerging renewable technologies and their system integration using smart energy grids, power to X approaches (like for instance hydrogen/methane), efficient energy storage solutions and corresponding distributed networks. To «decarbonise» the world, clean energy conversion large-scale systems with high stability and resilience should become the main priority for energy generation. With such a transformative approach we are accelerating our progress towards sustainable communities at minimum environmental impact.

In the near future, the Internet-of-Things (IoT) smart devices' technology is expected to grow exponentially creating numerus networks consisted of a multitude of data sources and sensors.§ Powering billions of nodes in the IoT network ecosystem constitutes one of the most challenging tasks. Integrating energy harvesting capabilities into the IoT systems, is a potential route to overcome this demanding power supply issue and allows for significantly lowered installation costs (no need for wired units or a battery). Consequently, a great priority in the field of IoT is the development of stable energy sources with a high efficiency-to-weight ratio, capable not only to transform the IoT nodes into completely self-powered systems but also, collectively all the nodes together, to contribute on grid electricity.[1–8]

In the last few decades, smart ways to convert abundant ambient energy into electricity were investigated, taking advantage of the available high frequency electromagnetic radiation, heat, vibrations, solar power, and various forms of water energy.[9–21] Graphene and other related two-dimensional materials (GRM) are an excellent material class to drive this innovation because of their extraordinary properties that emerge at the limit of two-dimensions (2D), such as strong light-matter coupling, tuneable optical bandgaps and various ferroicities emergency (*i.e.*, emergent piezoelectricity). The spatial quantum confinement effects anticipated at 2D limit provide a perfect platform to investigate unconventional device architectures with unprecedented characteristics and unique functionalities.[22–33] Small-scale energy conversion IoT devices enabled by GMR, have therefore the potential to revolutionize flexible sensors, printable electronics and healthcare applications.[21,34–37]

On the side of large-scale energy harvesting systems enabled by GRM, novel architectures have been demonstrated as a viable competition to conventional technologies for on-grid electricity generation. Notably examples range from photovoltaics (PVs),[38–45] photo-electrochemical/thermal systems,[46–48] hydrovoltaics[49] and blue energy harvesters,[11,50] to novel fuel cells (FC).[51–54] Despite the fact that the power conversion efficiencies (PCE) of GRM-enabled devices do not exceed currently those of more mature systems (*i.e.*, Silicon (Si), III–V semiconductors, *etc.*), GRM-enabled hybrid architectures offer an unprecedented combination of scalability, modularity and long-term chemical stability that is expected to provide new routes of multifunctional harvesting.[12,55–62] The combination of GRM's ultrathin form-factor

† https://ec.europa.eu/info/strategy/priorities-2019-2024/european-green-deal_en.
‡ https://ec.europa.eu/clima/policies/strategies/2050_en.
§ https://www.idc.com/getdoc.jsp?containerId=prUS45213219.

Konstantinos Rogdakis

Konstantinos Rogdakis is the Team Leader of Innovative Printed Electronics at the Institute of Emerging Technologies of the Hellenic Mediterranean University (HMU) Research Center. He has served at various academic research positions in high reputation European institutions including the Foundation of Research and Technology in Greece, the Institut Néel CNRS in France and the London centre for Nanotechnology – UCL. He obtained his PhD in Nanoelectronics from Grenoble Institute of Technology in France, in 2009. His current research interests include 2D materials engineering in various printed device concepts including high performing solar cells, functional sensors as well neuromorphic computation architectures towards energy efficient, intelligent Internet of Things and wearable systems.

Emmanuel Kymakis

Emmanuel Kymakis is the Vice-President of the Hellenic Mediterranean University (HMU) Research Center, Director of the Nanotechnology Division of the Institute of Emerging Technologies and Professor of Advanced Electronic Materials & Devices at the Dept. of Electrical & Computer Engineering of HMU. He obtained his PhD in Engineering from the University of Cambridge in 2003. He and Prof. Gehan Amaratunga are the inventors of the polymer-nanotube solar cell. His research lies at the interface between nanotechnology and electrical engineering and is centred on the development of printed electronic and energy devices. He was named as a 2014 ChemComm Emerging Investigator and has received two National Excellence Awards. He is currently the Director of the Post-Graduate Program "Nanotechnology for Energy Application" and the leader of the Energy Generation WP of the FET-Flagship Initiative Graphene.

with their manufacturing compatibility with large-scale printing or wafer-level GRM transferring processes promises to set new standards in on-grid electricity generation.[21,39,44,45,63–73]

In this review, we summarize the recent developments on the utilisation of GRM in emerging energy conversion device applications, mainly highlighting the high potential of this approach towards on-grid energy generation. Our approach bridges the well-explored area of developing small-scale GRM-enabled energy harvesters for powering IoT devices,[1,5,7,17,19,35,74–82] with recent research directions on GRM-enabled large-scale energy conversion installations. First, the whole bouquet of the emerging properties expected at the 2D limit of GRM intimately coupled to smart energy harvesting are discussed. Then, we briefly review GRM's high throughput formulation techniques focusing on upscaled inks/pastes production and wafer-scaled transferring of 2D materials to suitable substrates. Next, we present an overview of GRM-enabled small- and large-scale harvesters. Notably, we recognize the low PCE of currently available GRM-enabled harvesters, both on small- and large-scale, however, a multitude of in-series-connected devices, as well as hybrid multi-harvesting architectures – a process unattainable by conventional technologies, could assist in overcoming this hurdle. We also provide a perspective on the potential of combining the two approaches toward their eventual integration in a single macroscopic energy grid, where each network's node could contribute to on-grid electricity. Fig. 1 constitutes a summary of this review depicting GRM-enabled energy conversion technologies across different demonstrator's scales: from powering miniaturized IoT devices to large scale installations such as solar farms, towards smart cities of the future. We believe that this review can furnish some valuable references for the future development of GRM-enabled, cross-scaled, high-performance, energy harvesters with practical application capabilities toward on-grid energy generation.

2. Overview of GRM's emerging properties at 2D limit, formulation techniques, device manufacturing and main applications

The physical, chemical, and optoelectronic properties of GRM are remarkably modified compared to their corresponding bulk structures, when their thickness is scaled down to a single or

Fig. 1 Vision of future energy sustainable cities utilizing cross-scaled, GRM-enabled renewable energy sources. This approach extends across different demonstrator's scales: from powering single miniaturized Internet of Things (IoT) devices or integrating them into a wider network able to contribute to city's energy needs, to large scale installations for on-grid electricity generation. Notably, already demonstrated GRM-enabled solar farms (see Fig. 15 for real demonstrations)[38–45] and fuel cells[51–54] for the hydrogen (H_2) or methanol economy and their associated mobility to stationary power stations, can cover the main energy needs of the city and transportation, respectively. Furthermore, demonstrated salinity gradient plants and streaming potential harvesters installed at rivers/sea boundaries,[49] as well as various smart ways of harvesting water energy such as evaporation- or moisture-based,[11,50] all enabled by GRM, can revolutionize the way grid-electricity is provided in the near future.

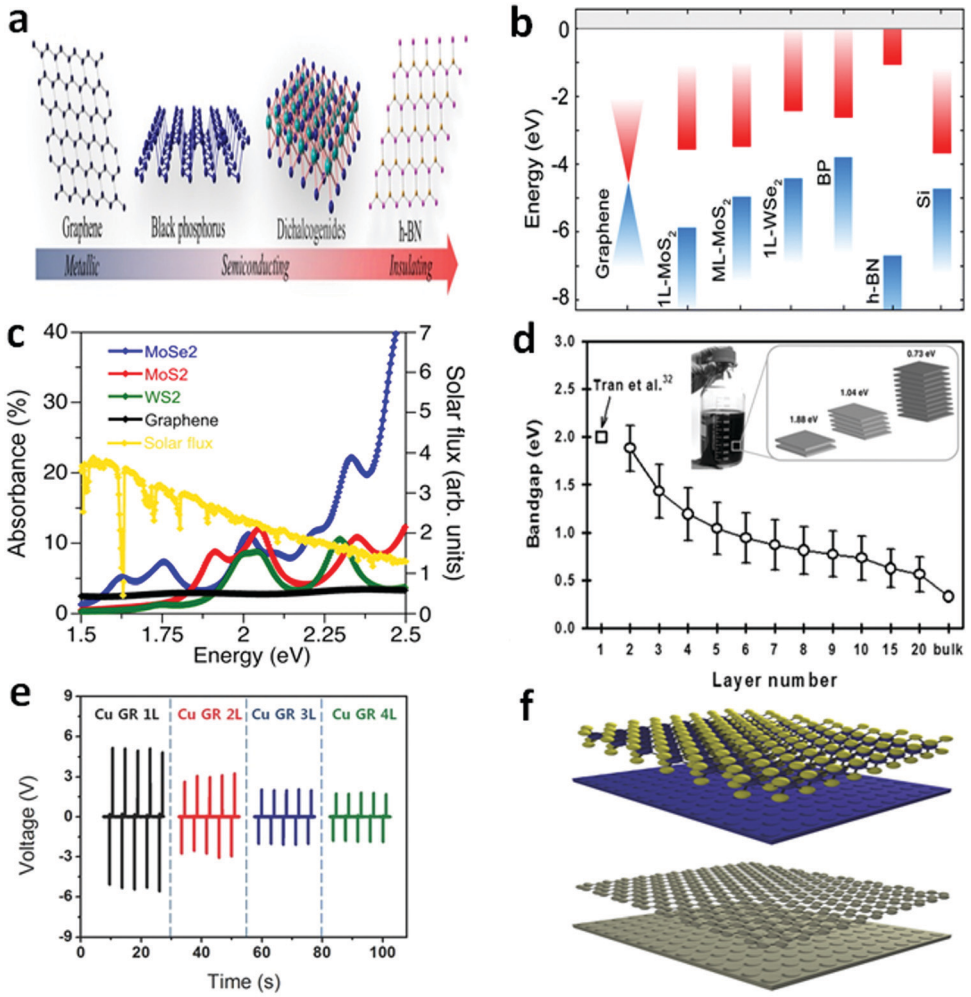

Fig. 2 GRM's emerging properties at 2D limit. (a) Schematic illustrations of prototypical 2D materials ranging from metallic to insulating. (Reproduced with permission.[124] Copyright 2019 Elsevier.) (b) Schematic band diagram of key GRM according to the available literature values of the work function and band gap. (Reproduced with permission.[93] Copyright 2018 Royal Society of Chemistry.) (c) Absorbance of three TMDC monolayers and graphene. (Reproduced with permission.[125] Copyright 2013 American Chemical Society.) (d) Energy bandgap of phosphorene with different thicknesses. (Reproduced with permission.[87] Copyright 2016 Wiley-VCH Verlag GmbH & Co. KGaA, Weinheim.) (e) Graphene-based ferroicity (triboelectricity) emergency at 2D limit. (Reproduced with permission.[126] Copyright 2014 Wiley-VCH Verlag GmbH & Co. KGaA, Weinheim). (f) Two dimensional materials employed as building blocks to fabricate GRM-enabled heterostructures. (Reproduced with permission.[94] Copyright 2018 Wiley-VCH Verlag GmbH & Co. KGaA, Weinheim.)

few atomic layers (Fig. 2). A vast number of 2D layered materials with varying chemical composition, atomic structure and electronic properties are available, as shown in Fig. 2a. Corresponding energy band diagrams of selected GRM showing their approximate energy band alignment are depicted in Fig. 2b. Enhanced Coulomb interactions arise due to the reduced spatial dimensionality, resulting in novel complexes and peculiar physics appearance at GRM surfaces or corresponding interfaces.[24,25,83] Furthermore, the high surface to volume atoms ratio of GRM results in high sensitivity to environmental conditions, enabling functional properties tuneable by a variety of external stimuli. Examples of fascinating emergent properties observable at room temperature with the potential to overwhelm conventional technologies include the indirect-to-direct energy band gap (E_G) transition (Fig. 2b), increased optical absorption (Fig. 2c), a layer-dependent direct E_G values (Fig. 2d) and electrostatic gate tunability, immunity from lattice mismatch, efficient charge separation and collection, lower spontaneous radiation loss, as well as emergent ferroicities (Fig. 2e) absent in the original bulk structures.[23,83–87] A detailed discussion of these fascinating properties and their relevance to efficient electricity generation upon various external stimulus will be presented per material family in Section 3.[22,24,88–99]

Ever since the discovery of graphene, plenty of 2D materials have been investigated, such as graphene oxide (GO) and derivatives,[100–102] graphdiyne,[103] group-VA semiconductors,[104] phosphides,[105] transition metal dichalcogenides (TMDC),[106–110] transition metal carbides/carbonitrides (MXenes)[78,111–113] and black phosphorous (BP), just to name a few.[74,87,114,115] The absence of an inherent E_G in graphene restricts its applicability

as a light active layer in energy conversion systems. Other 2D materials, however, exhibit a great properties diversity including insulating, semiconducting and metal-like 2D behaviour (Fig. 2a) that complement those of graphene. Moreover, the versatility of combining graphene with other functional components provides a powerful strategy to design artificial heterostructures (Fig. 2f) exhibiting tuneable properties towards unique device functionalities such as p–n and tunnelling diodes, light-emitting diodes/transistors and PV elements.[4,24,27,88,89,91,115–123]

A prerequisite for the massive deployment of GRM-enabled energy harvesters, and devices with commercialization potential in general, is the wide availability of high-throughput formulation techniques able to attain high GRM production volumes at low cost. At this point, it is noted that this review focuses on GRM-enabled energy harvesting demonstrators, thus an exhaustive presentation of GRM general properties, material formulation techniques, device fabrication methods and applications not related to energy conversion, is out of the manuscript's scope. Interested readers can refer to relevant excellent studies available in the literature.[63,67–69,114,127–133]

Material inks based on GRMs can be produced through liquid-phase exfoliation methods (*e.g.*, ultrasonication, flash graphene synthesis and wet-jet milling for scaling up), providing production rates compatible with massive applications.[68,70,127,134] Sedimentation-based separation approaches are used to tune on-demand the lateral dimensions size and the thickness of the exfoliated materials. Typical examples of wet-jet milling inks are shown in Fig. 3a, including graphene, Tungsten Disulfide (WS_2) and hexagonal boron nitride (h-BN).[68] The inset table shows the pressure and time required to process 10 mL of

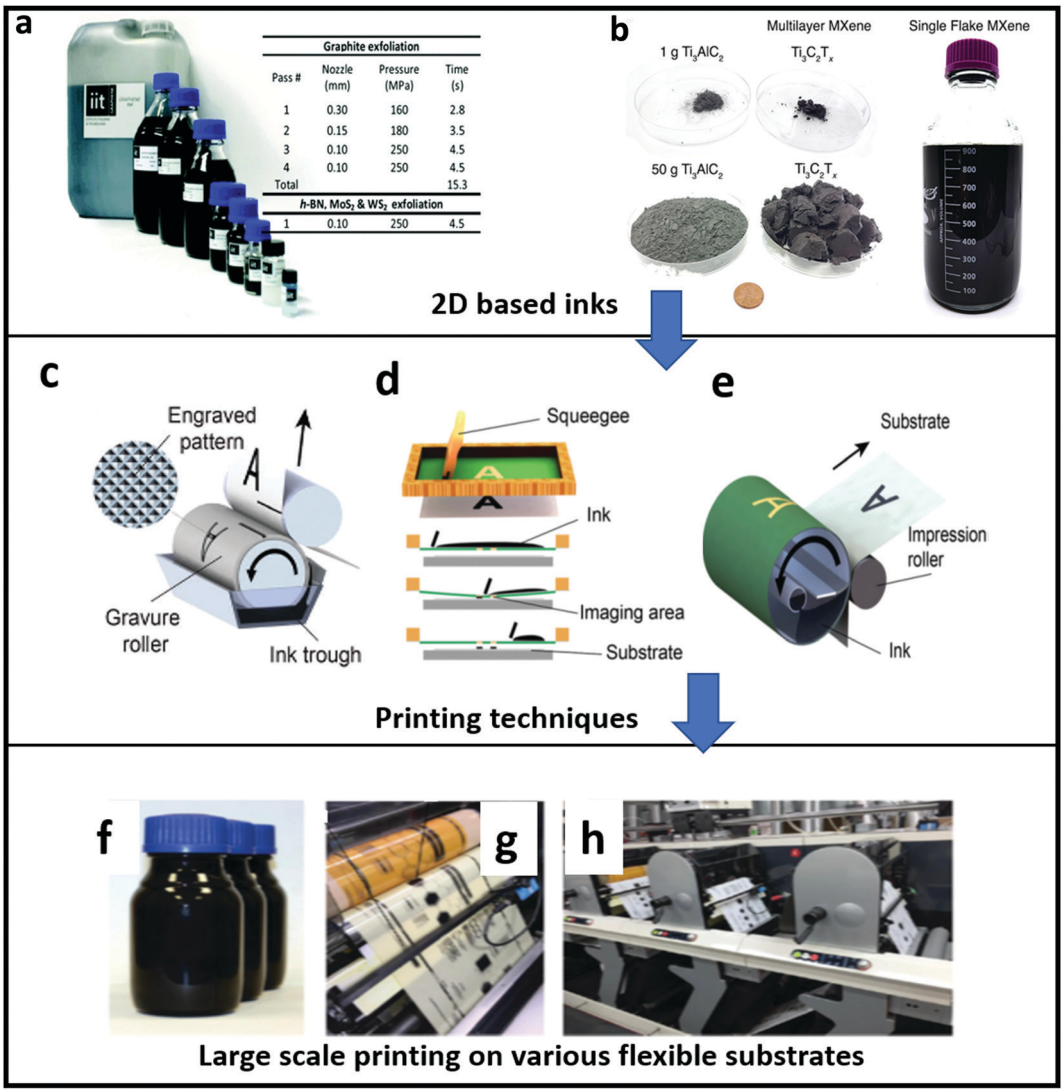

Fig. 3 GRM's production using solution processing and industrially compatible printing techniques. (a) Graphene, WS_2 and h-BN dispersions produced by wet-jet mill. (b) Images of the precursor Ti_3AlC_2 used in synthesis of the 1 and 50 g $Ti_3C_2T_x$ batch sizes. A 1 L solution of delaminated $Ti_3C_2T_x$ solution (10 mg mL^{-1}) is also shown. (Panels a and b are reproduced with permission.[68] Copyright 2018 Royal Society of Chemistry.) Schematics of (c) gravure printing, (d) flat-bed screen printing, and (e) R2R screen printing. (f) Graphene/carbon flexographic ink used for printed device on PET (g) or paper (h) substrates. (Panels c–h reproduced with permission.[67] Copyright 2018 Royal Society of Chemistry.)

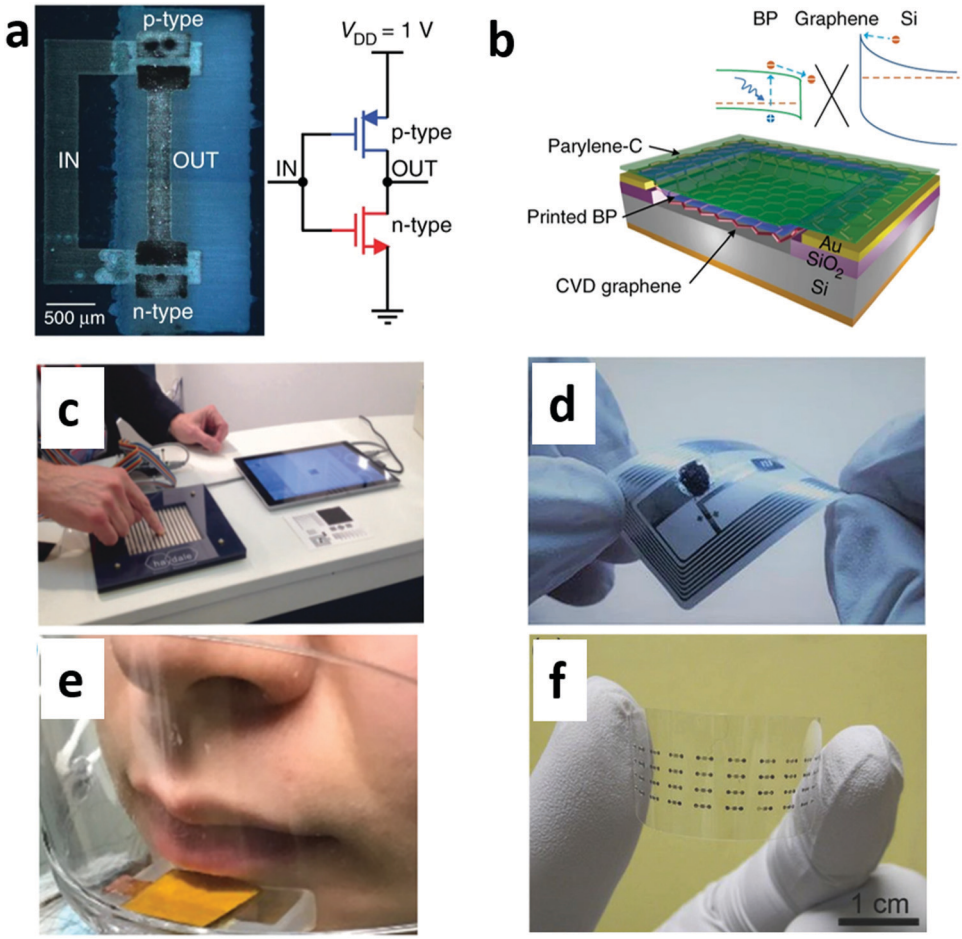

Fig. 4 Printed electronics, photonics, sensing and energy storage applications. (a) Fully inkjet-printed logic. Optical microscopy image (dark field) of an integrated circuit demonstrating an all inkjet-printed complementary graphene inverter as shown in the schematic. (Reproduced with permission.[150] Copyright 2017 Springer Nature.) (b) Schematic of the Graphene/Si Schottky junction/inkjet-printed BP photodetector arrays across a silicon wafer and the device band diagram configuration. (Reproduced with permission.[149] Copyright 2017 Springer Nature.) (c) Haydale graphene pressure sensors demonstration. (Haydale©).¶ (d) Photograph of sensor tag under twisting enabled by rGO. (Reproduced with permission.[152] Copyright 2017 Springer Nature.) (e) Application for respiration detection. (Reproduced with permission.[153] Copyright 2017 American Chemical Society), and (f) photograph of an array of graphene supercapacitors on PET (Reproduced with permission.[154] Copyright 2017 Wiley-VCH Verlag GmbH & Co. KGaA, Weinheim.)

layered crystals in the specific solvent. Images of selected bulk precursors for 2D titanium carbide MXene ($Ti_3C_2T_x$) material formulation and corresponding ink dispersions are presented in Fig. 3b, prepared using a custom-designed chemical reactor. This large-batch synthesis can produce up to 5 L of this MXene solution.

Therefore, it becomes apparent that solution-based processing offers routes to an upscaled production of 2D-layered semiconductor inks prepared in various solvents, while being compatible with different printing methods. Manufacturing techniques include gravure printing (Fig. 3c), flat bed (Fig. 3d) or roll-to-roll (R2R) (Fig. 3e) screen printing.[67] Currently, high quality printed layers of graphene have been demonstrated using these large scale printing technologies achieving films with very high mobilities values and at high printing resolution, achieving features size of ~20 μm. Printing trials using a graphene/carbon flexographic ink (Fig. 3f) on either a polyethylene terephthalate (PET) or on paper substrates are shown in Fig. 3g and h, respectively, using a commercial graphics printing press. Nevertheless, much work is still required for gravure and flexographic inks, other than graphene, in terms of ink formulation, electrical performance and the control of printing parameters. Scalable, highly quality synthesis of 2D heterostructures using solution-based processing remains a big challenge in the field, despite few reported chemically synthesized 2D heterostructures that elaborate a micromechanical stacking – a process however with limited industrial potential.

Numerous GRM-based manufacturing companies have been recently established worldwide providing specialized inks towards functional coatings deposition, aiming at their integration in (opto-) electronics, sensing and energy storage applications, providing new routes in the market of future flexible and stretchable electronics[4,38,39,46,63,71,92,95,124,127,128,131,132,134–148]

¶ Piezoelectric graphene ink enables thin-film pressure sensors of any size, available at: https://spectrum.ieee.org/nanoclast/semiconductors/materials/piezoelectric-grapheneink-enables-thin-film-pressure-sensors-of-any-size.

Representative examples of GRM-ink enabled devices are shown in Fig. 4. Going beyond individual electronic elements such as transistors or sensors, demonstrations of more complex printed electronic circuits have been reported.[67,149–151] Examples include 2D-material active heterostructures with graphene, WS_2 and h-BN inks, and use them to fabricate all inkjet-printed flexible and washable field-effect transistors on textile. This enabled fully inkjet-printed electronic circuits, such as reprogrammable volatile memory cells,[151] complementary inverters and OR logic gates (Fig. 4a).[149,150] The graphene/h-BN heterostructure FETs on polyester textile show mobility values up to 91 $cm^2 V^{-1} s^{-1}$, withstand up to $\sim$4% strain and are washable for up to at least 20 cycles.[150] The viability of the printed graphene/h-BN heterostructures FETs for electronic circuits was also demonstrated with fully printed complementary inverters, logic gates and rewriteable volatile memory. Moreover, junctions formed by graphene/WS_2/graphene exhibiting the higher electrical resistance that was interpreted as logic '0', while the graphene/graphene junction corresponding to lower resistance was interpreted as logic '1'.[151] On the field of optical sensing, a hybrid photodetector structure was demonstrated by inkjet-printing of BP flakes, integrated with a graphene/Si Schottky junction.[149] Fig. 4b shows an image of the printed devices across a Si wafer, while the inset schematically shows the structure of this hybrid device. The device exhibited a photoresponsivity of up to 164 mA W^{-1} at 450 nm, while even responding to a 1550 nm light that is beyond Si E_G, due to the layer-thickness dependent E_G of BP.

The company Haydale has recently demonstrated GRM enabled thin film pressure sensing panels (Fig. 4c).[67] In this panel design, printed graphene/binder composite was 'sandwiched' between a printed electrode matrix, enabling matrix's detection of resistance changes of the composite material upon pressure, while simultaneously indicating the location of touch. It was recently reported a flexible wireless gas sensor enabled by reduced graphene oxide (rGO) decorated with silver nanoparticles as the gas-sensitive material, embedded within a LCR circuit (Fig. 4d).[152] The reflectance of the sensor changes when NH_3 gas molecules are absorbed by the Ag nanoparticles-decorated rGO, since the impedance of the wireless sensor circuit is modified. The results showed that the sensor has a fast response time and recovery time, and also good repeatability.

A graphene-based pressure sensor was demonstrated being suitable for detecting various human motions, including in pulse detection, respiratory detection, voice recognition, as well as various intense motion detections.[153] In figure Fig. 4e, an application example is depicted where the tester wears a transparent mask with an integrated graphene pressure sensor. The gas pressure produced by each breath increases the resistance of the pressure sensor, showing a respiration rate of about 16 times min^{-1} before exercise, and 68 times min^{-1} after exercise. Besides, this real-time detection can help to monitor some respiratory and heart diseases quite significant in wearable devices for healthcare. On the energy storage applications, an array of graphene supercapacitors printed on PET (Fig. 4f) was shown to deliver a specific capacitance of 85 F g^{-1} at a current density of 100 A g^{-1} exhibiting excellent fabrication yield and limited variation in performance reveal the high reliability of the fabrication process.[154] Coupled with the high spatial resolution of printed devices as shown above, these results offer practical implications for printed electronics enabled by GRM.

Non-solution-based processing techniques, such as epitaxial Chemical Vapour Deposition (CVD) have already proven (Fig. 5a) to be capable of preparing high-quality 2D materials including even lateral and vertical heterostructures. Optical and Raman characterization confirm the upscaling potential and the high-quality of the growth process, as seen in Fig. 5b and c, respectively. Critical role on the final material quality is played by the growth duration (Fig. 5d) and substrate type (Fig. 5e and f). The scalable growth of wafer-sized GRM at low production cost, while being compatible with CMOS wafer processing, is expected to boost GRM's applications in high-performance electronics and optoelectronics.[63–65,155] Moreover, using CVD techniques, high-quality 2D stacks on a large-scale can be precisely adjusted with clean interfaces, potentially leading to novel physics and emergent properties, inaccessible in single layer systems.[46,47,65,66,89,95–97,121,131,144,146] The recently booming advances in angle-dependent physics of 2D heterostructures consist a notable example.[85]

Recent breakthroughs on GRM's transferring processes from an initial substrate where growth is performed, to any targeted substrate are expected to boost further the GRM-based device applications, and bring GRM closer into the semiconductor manufacturing lines.[66,88,143] A generic processing for GRM integration by adhesive wafer bonding in CMOS technologies was recently demonstrated by Quellmalz *et al.*, by either transferring a GRM monolayer or even heterostructure (Fig. 6a).[66] They demonstrated field-effect devices enabled by graphene exhibiting high carrier mobilities. To achieve this high performance, they fabricated a graphene/molybdenum disulfide (MoS_2) heterostructure by transferring upscaled CVD graphene (grown on copper foils) and MoS_2 ultrathin layer (from SiO_2/Si) to silicon wafers.

Wang *et al.* recently reported a new conceptual setup for continuously transferring graphene films, as shown in Fig. 6b.[143] This approach is universal applicable to any GRM. Their method can convert pristine graphene dispersion (solvent-exfoliated) into ultrathin graphene film transferable on various substrates of different material type. In the left part of Fig. 6b, an Illustration of the continuous transfer setup is depicted, whereas the continuous transfer process at contact angle of 30° is presented in the middle section of Fig. 6b. In the right part of Fig. 6b, a typical image of a transferred pristine graphene film on PET is depicted. This novel approach offers several advantages compared to other CVD transfer methods, such as applicability to various substrates allowing for different patterns to be formed, and being a fast, low-cost way to produce continuous, uniform, ultrathin films. These fascinating results on transfer methodologies indicate the compatibility of GRM with CMOS integrated circuits, paving the way for further progress in electronics, photonics, and energy applications.

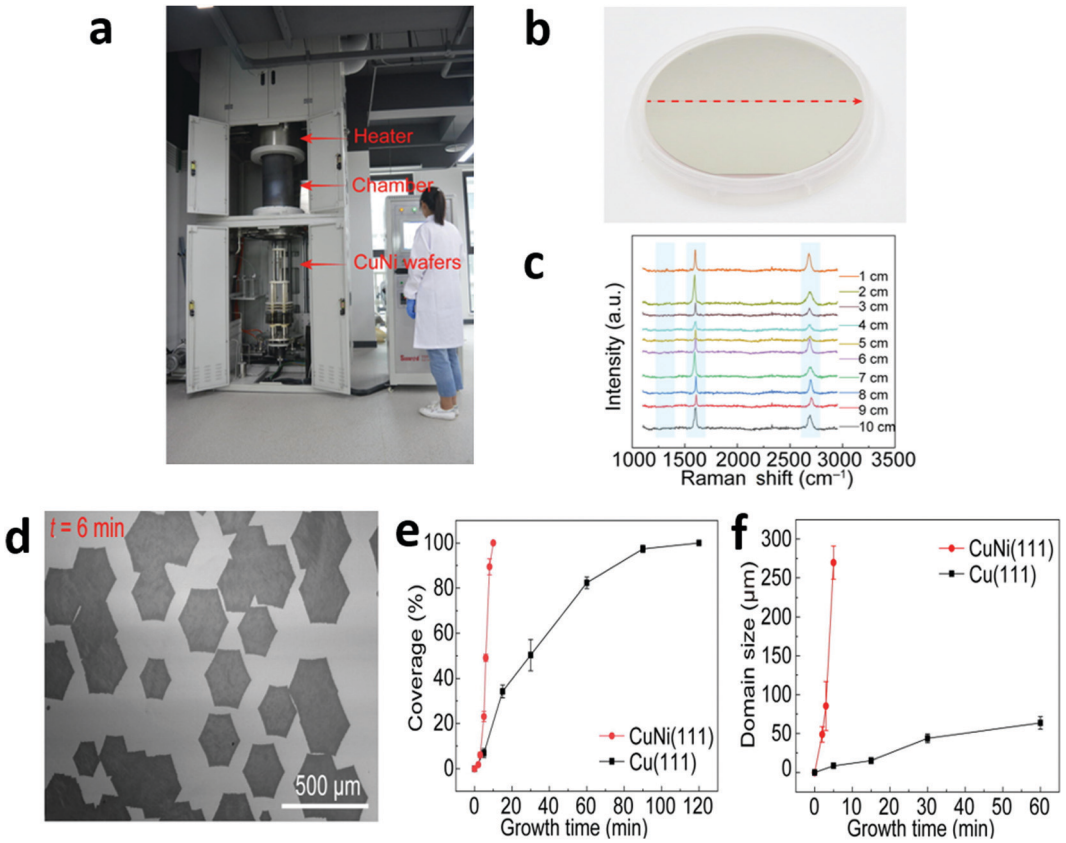

Fig. 5 Wafer-scale GRM production. (a) Pilot-scale CVD furnace for scalable growth of single-crystal graphene wafers on CuNi(111). (b) Photograph of a graphene/CuNi(111) wafer. (c) Raman spectra of graphene grown on a CuNi(111) wafer at varied positions in (b). (d) SEM images of graphene grown on CuNi(111) with t = 6 min. (e) Coverage of graphene grown on Cu(111) and CuNi(111). (f) Domain size of graphene grown on Cu(111) and CuNi(111). (Reproduced with permission.[71] Copyright 2019 Elsevier).

3. GRMs as a gigantic playground for energy conversion technologies

3.1 Enhanced light–matter interaction in GRM and their heterostructures enabling high performing PV and optoelectronic devices

A solar cell (SC) converts the energy induced by an absorbed photon directly into electricity through the PV effect. This light–matter interaction creates electron–hole pairs in the active material, while suitable transport layers assist in charge separation and eventually extraction to an external circuit. For the evaluation of a SC performance, its power conversion efficiency (PCE) is determined[156] as the fraction of incident power (P_{inc}) that is converted to electricity and is defined as: PCE = $V_{oc}I_{sc}$FF/P_{inc} where V_{oc} is the open-circuit voltage, I_{sc} is the short-circuit current and FF = $(V_{mp}I_{mp})/(V_{oc}I_{sc})$ is the fill factor with V_{mp}, I_{mp} as the voltage and current at maximum power output of the SC.

Silicon is by far the most widespread semiconductor in SC design. The success of Si is based on its small E_G, accessibility at low cost, high PCE and non-toxicity. Traditional wafer-based Si PV devices (n–p–n or p–i–n configuration) have dominated the market and have demonstrated PCE values up to 26.7% for back-contact heterojunction crystalline Si SC, setting the standards for any other, newer PV technology.[157] IoT-oriented applications require PV units characterized by flexibility, light weight form and low manufacturing cost, rendering therefore bulky, rigid Si technology unsuitable. To address this issue, perovskite PVs (PePVs) and organic PVs (OPVs) are now at the forefront of PV technologies due to their flexibility, high efficiency, and low fabrication costs enabled by industrially compatible large-scale printing processes (Fig. 3).[39,41]

GRM can be inserted as either the active or buffer layer, where the optimum configuration depends on the type of SC and the specific requirements of the targeted device application. Graphene shows remarkable optical and electronic properties, particularly an enormous intrinsic mobility (200 000 cm^2 V^{-1} s^{-1} estimated at room temperature).[158] It does not have a bandgap (without doping, Fig. 2b) but absorbs ~2.3% of the incident radiation throughout solar spectrum, a paradox at first look that was explained in terms of the fine-structure constant (Fig. 2c).[159] The semimetal graphene has been employed across different sections in inorganic and OPV, as transparent conductive electrode, active layer, transport interlayer for effective carrier extraction and as counter-electrode.[148] The van der Waals bonding between separate layers helps the formation of efficient junctions with reduced interfacial defects.

Semiconducting TMDC have E_G in the range of 1.0–2.0 eV that corresponds to the visible – near infrared part of the

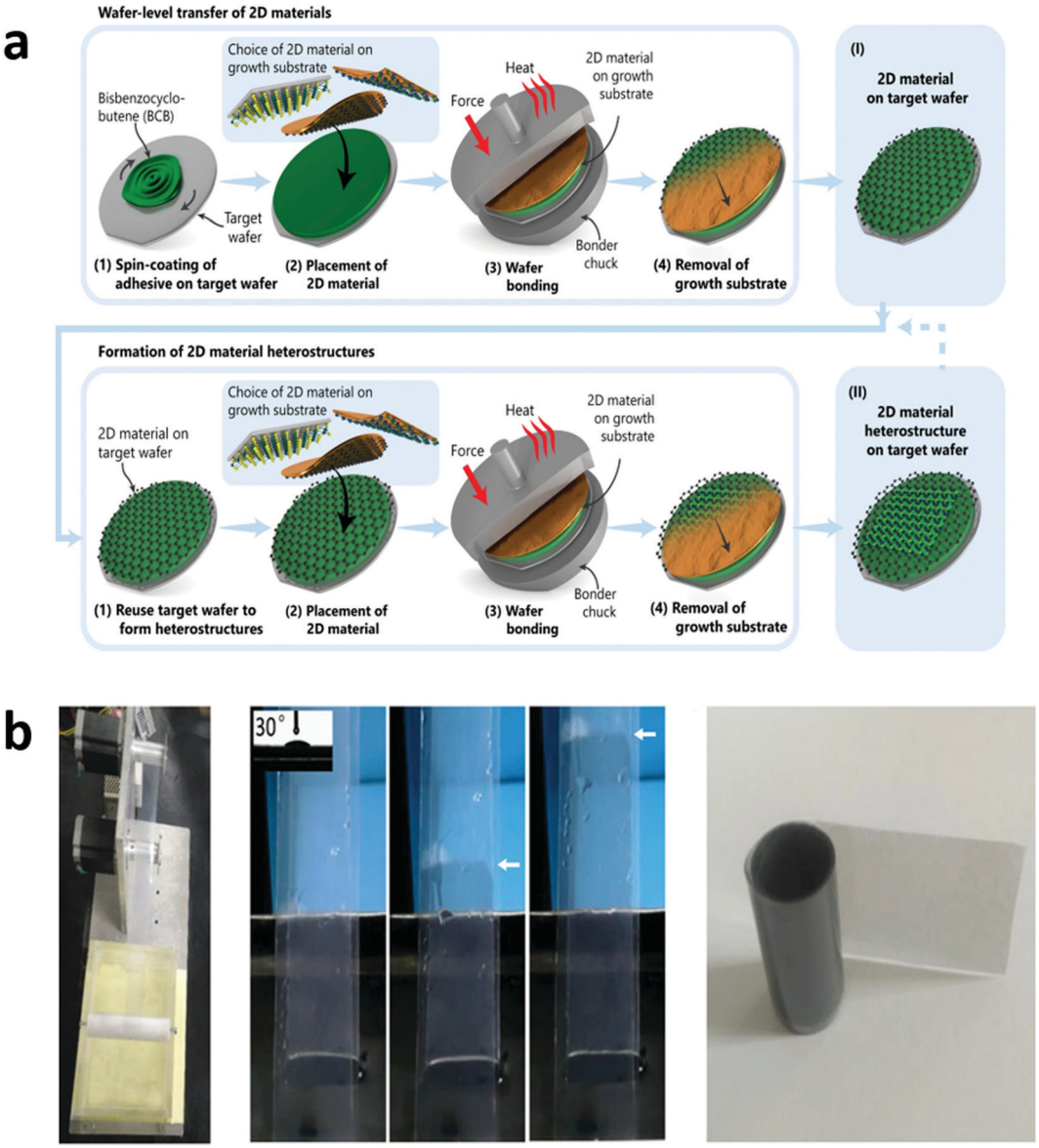

Fig. 6 Transferring 2D materials at different flexible substrates. (a) Schematics illustration of the methodology for wafer-level transfer of 2D materials and formation of heterostructures. The whole process includes either wafer-level formation and transfer of (I) single 2D material or (II) 2D material heterostructures. (Reproduced with permission.[66] Copyright 2021 Springer Nature.) (b) (left) Illustration for the designed continuous transfer setup. (middle) Continuous transfer process. (right) Photograph of transferred pristine graphene film on PET. (Reproduced with permission.[143] Copyright 2019 Wiley-VCH Verlag GmbH & Co. KGaA, Weinheim.)

spectrum. They have E_G structures corresponding to indirect transitions in their bulk forms, with their value increasing for decreasing number of layers and eventually convert to direct transitions at monolayers level. Their versatile optical properties and high transparency, the good charge carrier mobility and conductivity, in combination with high stability make them attractive for PV and photo-catalysis applications. Molybdenum and tungsten dichalcogenides (*e.g.*, MoS_2, $MoSe_2$, WS_2 and WSe_2) are currently the most researched TMDC. The most appealing material is MoS_2 exhibiting a direct bandgap 1.8 V at the monolayer level[160] and having a room temperature mobility of 200 $cm^2\ V^{-1}\ s^{-1}$ (Fig. 2b).[161] It is calculated that a MoS_2 monolayer can absorb 5–10% of the incident solar light or the same fraction as 50 nm of Si or 15 nm of GaAs (Fig. 2c).[125] Such a performance is essential for inserting a material in ultrathin SC architectures.

BP is a layered allotrope of phosphorus, is the precursor of the 2D material phosphorene that was first isolated in 2014 by micromechanical cleavage[162,163] (the same method used in 2004 for graphene). Currently it is more conveniently obtained by liquid exfoliation,[114,129,130,164–166] and CVD[167] procedures. Phosphorene shows high carrier mobility (up to $\sim$1000 $cm^2\ V^{-1}\ s^{-1}$ in few-layers),[165] and anisotropic electronic properties. It has thickness-dependent E_G ranging from 2.0 eV for

monolayer phosphorene to 0.3 eV for bulk BP (Fig. 2d), therefore it displays a wide light absorption range, from ultraviolet to near-infrared. It balances between the characteristics of graphene and TMDC and has a promising potential in the field of energy generation and storage. For example, it has been theoretically estimated that PCE values of around 18% could be achieved in a SC having an active layer with a bilayer stack of BP together with a monolayer MoS_2.[168] The stability issues of phosphorene, however, together with the high-density charge traps have considerably delayed the progress.[169]

An external quantum efficiency of 0.3% was achieved from gate-tunable p–n diodes fabricated by the combination of p-type BP and n-type monolayer MoS_2.[170] More recently, efficient hybrid heterojunction OPV using BP and PCBM (phenyl-C_{61}-butyric acid methyl ester) as active materials were reported with PCE of 8.3%.[171] A similar improvement in the efficiency of OPV incorporating BP in the active layer (donor PTB7-Th and PC71BM acceptor) has been attributed to high hole carrier mobility of BP.[172] Additionally, BP quantum dots were used with the purpose of light harvesting enhancement as well to assist the charge extraction in organic[173] and dye sensitized PV devices.[174] In comparison with reference devices, 12% and 20% PCE increase was observed, respectively.

It is possible to combine TMDC with metals[175,176] and make a Schottky junction SC or stack two different TMDCs and make p–n junctions serving as the PV active area.[92,93,116,125,144,177,178] The relatively low efficiencies of these devices are attributed to the nanometer thickness of the material that results in low light absorbance. Recently, high quality vertically stacked Sb_2Te_3/MoS_2 heterostructures were reported (Fig. 7a) to exhibit ultra-high current rectification ratio up to 10^6 (Fig. 7b) and typical photon-to-electron conversion efficiency reaching 4.5%, key performance indicators for optoelectronic applications (Fig. 7c).[144] A high performing hybrid PV photodetector based on $MoTe_2$/MoS_2 vertical heterojunctions[90] was reported exhibiting fast response time of 60 μs and high photoresponsivity of 46 mA W^{-1} at room temperature. This novel self-powered PV photodetector with fast response and broad detection wavelength range is promising for light sensing, on-chip logic circuits, and related applications.

A proof-of-concept on light-to ionic power harnessing driven by a coupled photon-carrier–ion transport was reported recently in a novel GRM binary multi-heterostructure with a potential for light-controlled ionic circuits, artificial photosynthesis, and biomimetic energy conversion.[179] The heterostructure is consisted of sequentially stacked WS_2 and MoS_2 multilayers with sub-1 nm interlayer spacing, as depicted in Fig. 7d. A photovoltaic potential difference is established between the two parts upon visible light illumination, initiating a net interlayer ion transport in equilibrium electrolyte solutions. Tuning of the process towards optimizing the power generation is achieved by varying the light intensity (Fig. 7e), ionic concentration and composition (Fig. 7f), and electrolyte pH. Under optimized conditions, an uttermost power density of nearly 2 mW m^{-2} can be achieved.

2D perovskites are also developed as counterparts of 3D structures, being compatible with compact devices schemes. These low dimensional structures enable enhanced device stability by replacing the small cations like Cs^+, Rb^+, methylammonium (MA), formamidinium (FA^+) that are used in 3D perovskites structures, with aromatic or aliphatic alkyl ammonium spacer cations.[181] As the 2D perovskites are sandwiched between the organic molecules the steric effect is making them resistant to degradation by moisture penetration but at the cost of a wider optical band gap.[182] The stability of 2D perovskite based heterostructures is increased further due to their low-ion migration.[183] 2D perovskites have currently inferior PCE (up to 18%)[184] compared to their 3D counterparts but significant progress has been made in very small time. Moreover, the minimized lead content in 2D perovskites affects less negatively the environment compared to 3D perovskites. Using therefore either standalone layered 2D perovskites or 2D layers on the surface of typical 3D materials is a way to improve both the stability and performance across an extensive array of configurations.[185,186]

A very promising alternative is the fabrication of novel hybrid heterostructures based on the combination of GRM with 2D perovskites (Fig. 7g) targeting to combine advantages of both low dimensional systems into a single stack.[187–189] In these hetero-structured systems, quantum confinement effects allow tailoring band alignments of the heterointerface and subsequent interfacial charge transfer. Four orders of magnitude higher photoresponsivity and faster photo-response compared to bulk structures were reported (Fig. 7h).[180] Furthermore, a variety of lateral heterostructures based on 2D perovskites ($MAPbI_3$) and GRM were shown to exhibit record-high light-emission efficiency and high electron–hole extraction rate enabled by the strong interfacial coupling.[187]

The aforementioned literature reports emphasize the high potential of the emerging optoelectronic properties of various GRM towards PV and optoelectronic applications. Moreover, the ultra-compact design of printable perovskites and their integration with GRM offer many possibilities to discover new properties and functionalities towards developing various power harvesters for either miniature IoT and wearable systems, or upscaled energy harvesting systems. Engineering approaches for PV with enhanced performance include interfacial incorporation of 2D active interlayers such as graphene and TMDC, optimization of GRM's doping and surface functionalization, and also the possibility of inserting passivation layers such as 2D insulating crystals towards 2D semiconductor/2D insulator/3D semiconductor architectures.[18,118,190–192]

3.2 Enhanced strain-charge coupling and electrification in GRM for mechanical energy harvesting

Piezoelectric properties. Mechanical energy harvesting is a promising functionality suitable for either powering miniature IoT devices or even allow for large-scale energy harvesting upon multiple devices integration. In particular, the associated piezoelectricity lays the ground for attributing the mechanical phenomena as the lingua franca of modern electronics. On the macroscopic scale, it is broadly employed to achieve electromechanical coupling in a plethora of sensors and actuators. Studies have shown many promising 2D materials including

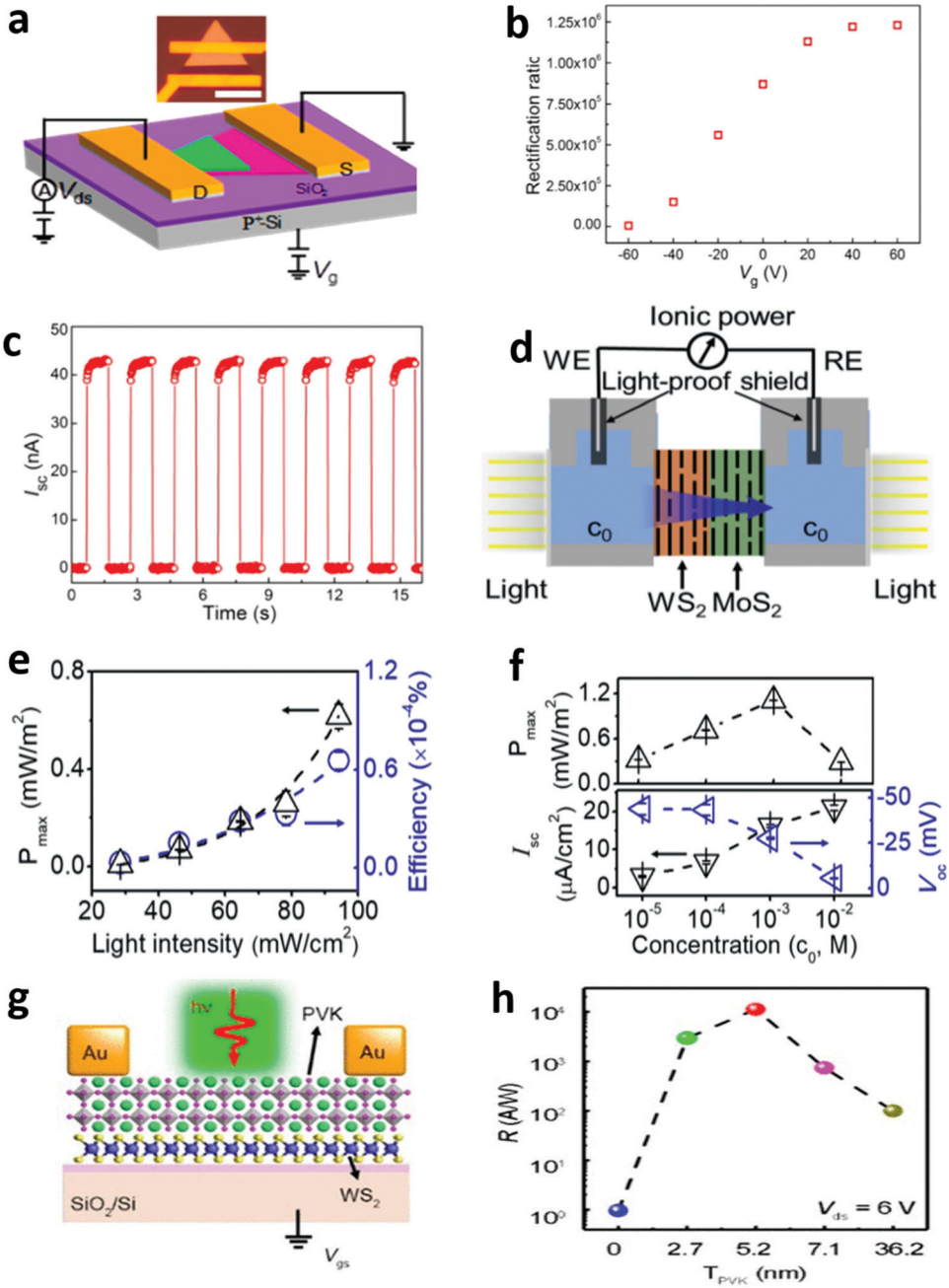

Fig. 7 Emerging optoelectronic properties and novel optoelectronic devices enabled by GRM heterostructures. (a) Schematic diagram of the Sb_2Te_3/MoS_2 heterostructure-based photovoltaic device. (b) The extracted rectification ratio as a function of back gate voltage V_g. (c) Photocurrent response of the p–n junction with periodically switching on and off the light (power density: 30.7 mW cm^{-2}; wavelength: 520 nm). (Panels a–c reproduced with permission.[144] Copyright 2019 Elsevier.) (d) Schematic of a light-to-ionic power generation device. (e) Light intensity dependence of the maximum ionic power density and corresponding energy conversion efficiency. (f) Concentration dependence of P_{max}, I_{sc}, and V_{oc}. (e) pH dependence of P_{max} and its efficiency. (Panels d–f are reproduced with permission.[179] Copyright 2021 Wiley-VCH Verlag GmbH & Co. KGaA, Weinheim). (g) Schematic illustration of the three-terminal back-gate device based on 2D perovskite/WS_2 heterostructures. (h) Thickness dependent photoresponsivity. (Panel g and h are reproduced with permission.[180] Copyright 2019 American Chemical Society.)

h-BN, TMDCs, group III and IV monochalcogenides and even chemically modified graphene.[26,30,31,79,80,193–202] Single or few layers of them exhibit piezoelectricity, a property missing from their 3D precursors. It is attributed to the lattice distortion caused by strain and the consequent charge polarization in the crystal. Piezoelectricity appears in materials which do not have centro-symmetry in their crystal structure, and they are non-metallic (*i.e.*, have a non-zero E_G). The effect's magnitude depends on the number of layers, typically declining when more than one layer is present (Fig. 2e).

The experimental observation of piezoelectricity in mechanically exfoliated monolayer (2H-) MoS_2 was reported in 2014.[196,203]

It was shown that periodically stretching and releasing of MoS_2 monolayers, with AB stacking structure, produces oscillating piezoelectric voltage and current outputs.[196] Not surprisingly, it can also induce changes in the band structure of MoS_2.[196,204,205] A layer dependence effect has been experimentally detected; while the monolayer MoS_2 exhibits strong piezoelectricity the bilayer and bulk flakes have a piezoresistive response.[196,204] For MoS_2, which is the most studied 2D TMDC material for piezoelectricity, the strain-induced dipoles have reversed directions in adjacent layers.[196] This way the piezoelectric contribution of each layer is counterbalanced by the next layer and odd-numbered two-dimensional materials have piezoelectric effects (odd–even effect). For odd-layer samples the piezoelectric output is large and decreases roughly as the inverse of the number of layers. The origin of this ''odd–even effect'' is linked with the asymmetric modulation of carrier transport by strain under opposite drain bias in a single-layer device, an effect that is cancelled in even-layer or bulk films. This novel piezotronic behaviour observed in a single-layer device was explained by asymmetric Schottky barrier heights resulting from strain-induced polarization in systems with broken inversion symmetry. MoS_2 layers having a AA stacking, thus the 3R-MoS_2 crystal structure, support identical directions of strain-induced dipoles in adjacent layers, thus resulting in strong piezoelectric effect in multilayer structures. Nevertheless, 3R-MoS_2 structure is thermodynamically unstable.

The same polarization pattern was recently observed for h-BN using electrostatic force microscopy and eventually justifying the piezoelectricity prospects of the material.[197] In Fig. 8a, a topography of a representative region with bubbles and creases is shown. The dashed line separates a monolayer area (main part of the image) from a bilayer terrace (bottom right corner). It was calculated that h-BN has efficiency (piezoelectric coefficient) comparable to the bulk values of conventional piezoelectrics such as ZnO, AlN, and lead zirconate titanate ceramics. Phosphorene has also been predicted to possess piezoelectricity and lately positive experimental evidence was presented for the case of multilayer BP.[74] Optical images of multilayer BP piezoelectric device are shown in Fig. 8b, whereas corresponding direct-current electrical characterization under applied strains along the armchair and zigzag directions are depicted in Fig. 8c. Current–voltage measurements demonstrated a piezotronic effect, and cyclic compression and release of BP flakes showed an intrinsic current output as large as 4 pA under a compressive strain of -0.72%. The piezoelectric signals superimpose and counteract each other depending on the direction of polarization. Notably, single layer materials cannot be considered ideal for actual piezoelectric devices due to their limited mechanical durability for continuous operation and demanding fabrication conditions. Additionally, by utilizing more layers at once the materials eventually recover centrosymmetry and piezoelectricity is suppressed.[74] The interest for the material is strong but researchers have to overcome the fact that handling and integration of phosphorene to devices is difficult because of the fast oxidation in the air.[206]

The reorientation of individual layers of the TMDC WSe_2 (turbostratic stacking) has been demonstrated to be a way to produce bilayers with high piezoelectric performance and excellent mechanical durability.[198] Efforts are currently focused on the improvement of the energy conversion efficiencies, mainly by refining the interface properties and optimizing the device structure. Actually, a screening of crystallographic data has shown that within a sample of around 50 thousand structures there were already 325 structures of potentially piezoelectric 2D materials identified by an appropriate algorithm.[207] In a recent theory report, a strong out of-plane piezoelectricity was predicted for M_2CO_2 MXenes system that is highly desirable for ultrathin piezoelectric cantilevers and diaphragms.[208]

There is always the prospect of extending the field of research as many existing inorganic materials are under evaluation. For example, Indium selenides (α-In_2Se_3 and γ-InSe) that also have non-centrosymmetric, 2D-layered crystal structure with an AA stacking symmetry, maintain the same polarization orientation between adjacent monolayers and thus display increasing piezoelectric coefficients as thickness increases and at the same are quite stable.[26] This property is an intrinsic solution to the general problem of lower response of multilayer crystals allowing multilayer structures to exhibit higher polarized charge densities and thus piezoelectric effects, independently of odd- or even-layer number, than 2D piezoelectric materials with inversion centres.[209–211]

Triboelectric properties. Humans knew for thousands of years that rubbing amber to a piece of cloth would make it ''snatch'' and lift small light objects. Electric charging by rubbing an object to another was the first electricity manifestation controlled by humans. Actually, the modern term ''electric'' is derived from the ancient Greek word for amber (elektron). Triboelectric effect is the term describing this contact-induced electrification, due to which a material gets charged when it is in frictional contact with a different one. It is a highly complex process in which many small scale physical and chemical factors are contributing, such as material deformations, fracturing, heat generation, electron and ion transfer. Since there has been no definite association between the effect and some fundamental properties of the materials, there is also no inclusive theory that can precisely predict the occurrence and the magnitude of triboelectricity. The typical tool for evaluating the materials is the empirical ''triboelectric series'' that is made by ranking materials according to their tendency to lose or gain electrons when in contact to each other.[212,213] During such an interaction one of the two substrates will always gain electrons while the other substrate will lose electrons.

From this perspective, 2D layered materials have been investigated, separately or in combination with various polymers. Most of the GRM are placed in the negative side of the triboelectric series, *i.e.* they would rather gain electrons from most materials, due to their charging polarities.[80,214] Besides, GRM based on their work-function tunability and thus the capability of controlling the triboelectric charging process through chemical doping, offer new ways towards thin and flexible triboelectric devices.[80] One effective approach is to use GRM that can capture electrons readily as dopants into bulk friction materials. In Fig. 8d, the output results of various

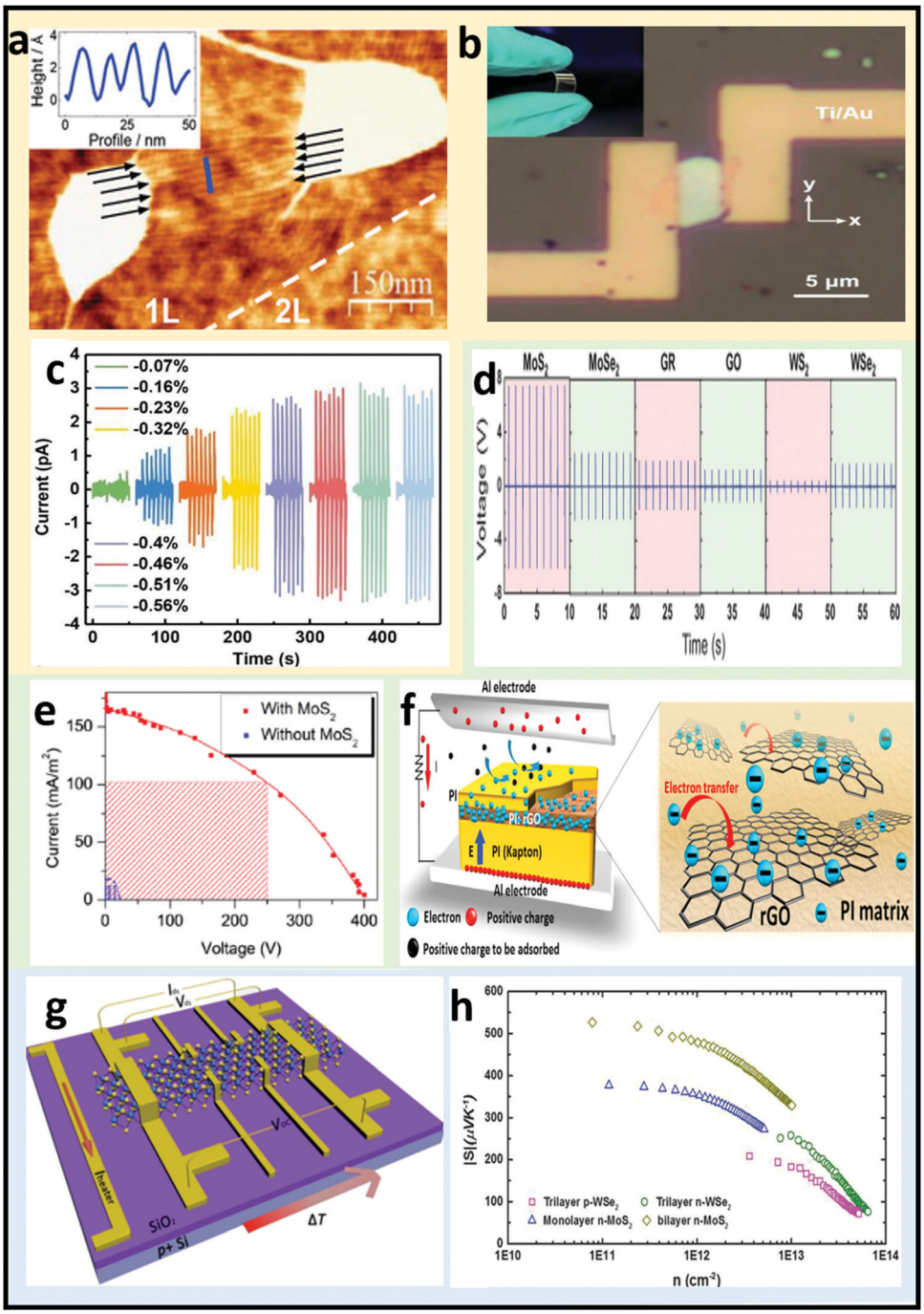

Fig. 8 Novel energy conversion approaches based on piezoelectricity, triboelectricity and thermoelectricity of GRM. (a) Monolayer h-BN on graphene. (Reproduced with permission.[197] Copyright 2020 WILEY-VCH Verlag GmbH & Co. KGaA, Weinheim.) (b) Optical microscopy image of flexible multilayer BP piezoelectric device and electrodes in the armchair orientation. Inset: Photo of the flexible PET substrate. (c) Short-circuit current response of the armchair oriented BP device under periodic strain. (Panels b and c are reproduced with permission.[74] Copyright 2020 WILEY-VCH Verlag GmbH & Co. KGaA, Weinheim.) (d) Output voltage signals of 2D material–nylon TENG. (Reproduced with permission.[80] Copyright 2018 WILEY-VCH Verlag GmbH & Co. KGaA, Weinheim.) (e) Curves of the output peak current as a function of the output peak voltage for the TENG with and without monolayer MoS_2. (Reproduced with permission.[81] Copyright 2017 American Chemical Society.) (f) (left) Illustration of the vertical contact-separation mode device with a PI:rGO film. The right panel shows a schematic diagram of electron transfer from the PI layer to the rGO sheets. (Reproduced with permission.[216] Copyright 2017 Elsevier.) (g) Back-gate induced thermoelectric measurement setup for monolayer, bilayer and trilayer MoS_2. (Reproduced with permission.[217] Copyright 2017, American Physical Society.) (h) Seebeck coefficient of trilayer p-type, n-type WSe_2, and monolayer, bilayer MoS_2 as function of carrier concentration (Reproduced with permission.[75] Copyright 2018, WILEY-VCH Verlag GmbH & Co. KGaA, Weinheim.)

GRM-enabled triboelectric films and their relative characteristics are shown. Amongst them, MoS_2 is a competitive candidate as a charge-trapping agent due to its quantum confinement effect, appropriate energy level and large specific surface area. MoS_2 exhibits the highest output voltage and current values reaching up to 7.48 V and 0.82 μA, respectively, indicating that MoS_2 is triboelectrically the most negative among the investigated GRMs so far.[80] A direct comparison of the output peak current as a function of the output peak voltage is depicted in Fig. 8e for films with or without MoS_2 indicating the superior performance of the GRM-enabled device. The area of the largest rectangle defined by the current–voltage curve corresponds to the maximum peak power density. In particular, devices with integrated MoS_2 reached a maximum peak power density value of 25.7 W m^{-2} at a resistance of approximately 5 MΩ, which is 120 times larger than that of the case without MoS_2.[81]

As a step further, an enhanced DC output can be realized by using various MoS_2 multilayer-based heterojunctions with movable substructures. It was shown that the tribo-excited energetic charge carriers can overcome the interfacial potential barrier triggering electrical conduction with an optimized power output, while the direction of the DC power was controlled by the band bending in the surface charged region of MoS_2.[215] Interfacing this multilayer system with high-k dielectric layers of different thickness or composite polymers offers another degree of freedom of controlling the voltage and current output. In addition, other materials, such as rGO and GO, were also capable of becoming electron-trapping sites in the bulk friction layer toward large triboelectric enhancement.[216] A schematic view of a vertical contact-separation mode device with an electron-trapping layer is shown in Fig. 8f. The bottom part of the device is made of a glass substrate onto which an Al electrode and a negative friction composite layer. The polyimide (PI) multilayer stack consists of three different layers: (PI)/(PI:rGO)/PI stacked structure. The integration of the rGO led to the suppression of triboelectric electron loss through capturing and storing the generated electrons in the rGO sheets, an effect resulting from the strong interaction between the PI layer and the rGO. This hybrid approach that suppresses the recombination between triboelectric electrons and positive charges, thus increasing the electron density in the friction layer, allowed to reach a maximum output power density of 6.3 W m^{-2}, which was 30 times larger than the reference sample.

3.3 Emergent thermoelectric properties for waste thermal energy harvesting at ultra-high conversion efficiencies

The thermoelectric (TE) effect, otherwise known as "Seebeck effect" is the direct conversion of a temperature gradient between two dissimilar electrical conductors or semiconductors to an electrical voltage. When the sides of TE materials are exposed to different temperatures, a voltage is created across the two sides of the material. Conversely, when a voltage is applied, a temperature difference can be created, known as the "Peltier effect". The efficiency of a TE material is represented by the dimensionless figure of merit: $zT = S^2\sigma T/\kappa$ where S is the Seebeck coefficient, σ is electrical conductivity, κ is the thermal conductivity, and T the temperature. An appropriate material is one that exhibits a large Seebeck coefficient, high electrical conductivity (thus high density and mobility of charge carriers) in combination with low thermal conductivity. One can intuitively realize that such a combination is not a trivial case since these requirements are usually met separately by semiconductors, metals and glasses.[218,219] TE devices are made by combining an n-type and p-type semiconductor to a junction. A heat source at one side makes ("pushes") charge carriers to conduct heat to the cold side, moving electrons (in the n-type) and holes (in the p-type), eventually generating a voltage difference. A TE device can also be operated in reverse as a heat pump for cooling purposes. Thermoelectric devices are used as a way to produce electricity from waste heat or for cooling in specialized applications. More than half of the energy utilized worldwide is lost as waste heat.[218] It is of great value therefore, both economically and environmentally, to exploit waste heat and recover an extra amount of noble electrical power. Waste heat is also abundant in places such as industry, automobiles and heating or cooking installations.

With several decades of practical applications for TE materials, it has been established to be a worthy choice to select nanostructured materials such as those based on Bi_2Te_3 and its alloys for achieving good electrical and low thermal conductivity with an acceptable efficiency.[218,220] These 2D-layered nanostructures have much lower thermal conductivity along the cross-plane direction than the in-plane direction.[221,222] Many new ideas have been inspired by the novel and rich physics in GRM, not only in fundamental TE studies but also for its practical purposes. Carbon materials, such as carbon nanotubes or graphene, are promising materials for TE energy harvesting due to their excellent flexibility, good stability, and high-power factor.[76] Graphene has high thermal conductivity and relatively low Seebeck coefficient, a combination, however, unfavourable for TE devices. Nevertheless, as a 2D archetypal material it has been the subject of extensive research aiming to improve its efficiency[223–226] and provide better understanding of the emerging phenomena[227–230] in 2D-layered substrates. As the thermal conductivity of graphene is dominated by phonons (lattice vibrations) it could be manipulated by the introduction of zigzag edge-disorder in graphene nanoribbons[223,226,228] or periodic holes[229] and lattice defects.[225,231] High degrees of functionality is offered by GO, a material that can be easily reduced to rGO by reducing oxygen presence during growth, resulting to high performing TE devices with tuneable conductivity type, band gap, and thermal conductivity.[75,76,232] Besides, hybrid approaches such as TE matrix/graphene composites could effectively achieve optimized TE performances due to various mechanisms. In particular, efficiency modulation based on geometric factors gives surprisingly high projected zT = 3–4.[233,234] These studies indicate that graphene can be engineered to achieve high-performance as a TE material.

Apart from graphene-based materials, BP and TMDC have been investigated as promising TE materials owing to their large effective mass. Their associated high electronic power factor performance is mainly attributed to the increase in

degeneracy of band valleys, or the so-called band convergence, induced by the strain.[75] Specifically, the TE properties of TMDC have been investigated both experimentally and theoretically.[75,235–241] A typical setup for the direct measurement of the TE voltage for few-layer MoS_2 is illustrated in Fig. 8g. The experimental work on TMDC has so far focused on two compounds—MoS_2 for n-type and WSe_2 for p-type, and their heterostructures.[75,235] Having a phonon mean free path of about 10 nm the monolayer MoS_2 exhibits a lower thermal conductivity compared to graphene.[240,241] It was observed that monolayer MoS_2 has 2–3 orders of magnitude smaller thermal conductivity than graphene, which makes it a promising TE material. Both Seebeck coefficient and power factor of tri-layer WSe_2 are comparable to that of n-type MoS_2 (Fig. 8h).[75,235]

BP exhibits a strong in-plane anisotropic behavior demonstrating a distinguished behavior for charge and phonon degrees of freedom. Because of its ridged structure, the electrical conductivity, and the thermal conductivity are different in the zigzag and in the armchair direction of the lattice.[242–246] Actually, they were found to exhibit an orthogonal behavior: while the electrons prefer to propagate along the armchair direction, the phonons prefer to move along the zigzag direction. Single crystal BP flakes show a larger Seebeck coefficient than the bulk material (510 $\mu V K^{-1}$ at 210 K *versus* 340 $\mu V K^{-1}$ at 300 K).[245] Although these values are currently low for real TE applications, doping approaches with Sb[247] and decoration with Au nanoparticles[246] has been proposed as ways to dramatically increase the efficiency and reduced the degradation of BP, respectively, making fabrication of TE devices less difficult.

In 2014, Zhao *et al.* reported a surprizing high TE performance for a layered and highly anisotropic crystalline SnSe.[248] The reported exceptional efficiency is due to the ultralow thermal conductivity even when the SnSe undergoes phase transition at $T > 750$ K. The high zT value of 2.6 at 923 K for the p-type material[248] can be paired with that of 2.2 at 773 K for an n-type[249] SnSe doped with Bi, having a preferable crystallographic axis orientation. The production of high-performing polycrystalline SnSe is currently the focus of the research targeting improved mechanical properties at minimum production cost being compatible therefore with an industrial scale-up.[218,250–252] In terms of high temperature operation, developing GeTe-based devices[16] can be of great interest in the future, due to its high conversion performance and good mechanical properties, as well as the ability for pairing n-type and p-type legs. In fact, theoretical calculations predict an extremely promising TE performance (possible $zT > 4$) in n-type GeTe, while recent experimental findings support a quality factor as high as 0.3, 0.9,and 1.5 at 300, 500, and 700 K, respectively.[233]

3.4 GRM surface as photo-catalytic and a photothermal energy conversion platform

Photocatalytic reactions are part of promising long-term technologies such as water splitting for hydrogen production, carbon dioxide reduction or photocatalytic pollutant degradation. In the simplest configuration, upon excitation of the semiconductor by an incident photon (with energy higher than its E_G) an electron–hole "pair" is generated. However, photogenerated excited states are not stable and the charge carriers can eventually recombine. In order to participate in photocatalytic reactions, the electron and hole are dissociated and transported across the surface to reduce or oxidize the reactants adsorbed on the semiconductor. A strongly related class of reactions that often share the term photocatalysis, are those that require an externally applied potential, which are typically denoted as photo-/electrocatalytical reactions.[253] The ideal technical scheme for a complete water cycle consists of water splitting for fuel generation *via* the hydrogen evolution reaction and oxygen evolution reaction producing gaseous hydrogen and oxygen molecules, respectively. This process is usually followed by the power generation based on the reverse process that is the core of FC operation. Carbon dioxide emissions from fossil fuel consumption is an issue frequently associated with anthropogenic climate change. A practical solution could be the capture and direct conversion (photocatalytic reduction) of CO_2 to another form of fuel or energy product like carbon monoxide (CO), formate ($HCOO^-$), methanol (CH_3OH), methane (CH_4), ethylene (C_2H_4). Photocatalysis, in a similar manner, could also provide the means for degradation of pollutants.

Many GRM have been employed in photocatalysis research.[253,254] TMDC, like the low cost MoS_2, have gained increasing attention. The exposed edges of GRM constitute the active sites for many heterogeneous reactions.[255] Although MoS_2 at its bulk form has a small indirect E_G (non-favorable, 1.3 eV), going down to few-layer MoS_2 gives rise to a direct, larger E_G, suitable for solar power harvesting (1.8 eV for single layer).[160] MoS_2 has received extensive attention in hydrogen evolution reactions as the atomic hydrogen is efficiently absorbed on the active sites $\left(\Delta G_H^\circ \approx 0\right)$ making it a potentially good catalyst.[256–258] To improve the overall activity, significant effort has been made in creating nanospheres, nanoflowers, and 2D sheet films.[259–262] Sekar *et al.* have recently demonstrated the integration of large surface area and high conductivity graphene-based derivatives along with MoS_2 aiming at developing hybrid electrodes for supercapacitors with improved electrocatalytic performance towards hydrogen evolution reaction applications.[260] In Fig. 9a, the rate performances of rGO, pristine MoS_2 (termed as M), nitrogen doped graphene quantum dots (N-GQDs) (termed as MQ) and MoS_2-rGO (termed as MG), as well as the combination of 3D-MoS_2 nanospheres and N-GQDs, anchored with rGO nanostructures (MoS_2-N-GQDs-rGO: termed as MQG) electrodes at various current densities are shown. Compared to pristine MoS_2-modified electrode (162.7 $F g^{-1}$), the MQG-modified electrode exhibited a higher specific capacitance, superior cycling stability with the capacitance retention of 75.8% after 1000 cycles. The MQG composite nanostructure material was tested as electrocatalyst for hydrogen evolution reaction in 1 M KOH exhibiting promising performance compared to reference samples.[260] Additional impedance measurements allowed to estimate the internal resistance and to investigate the charge transfer kinetics and ion diffusion process of the electrodes. By performing data fitting using an equivalent circuit, Sekar *et al.*

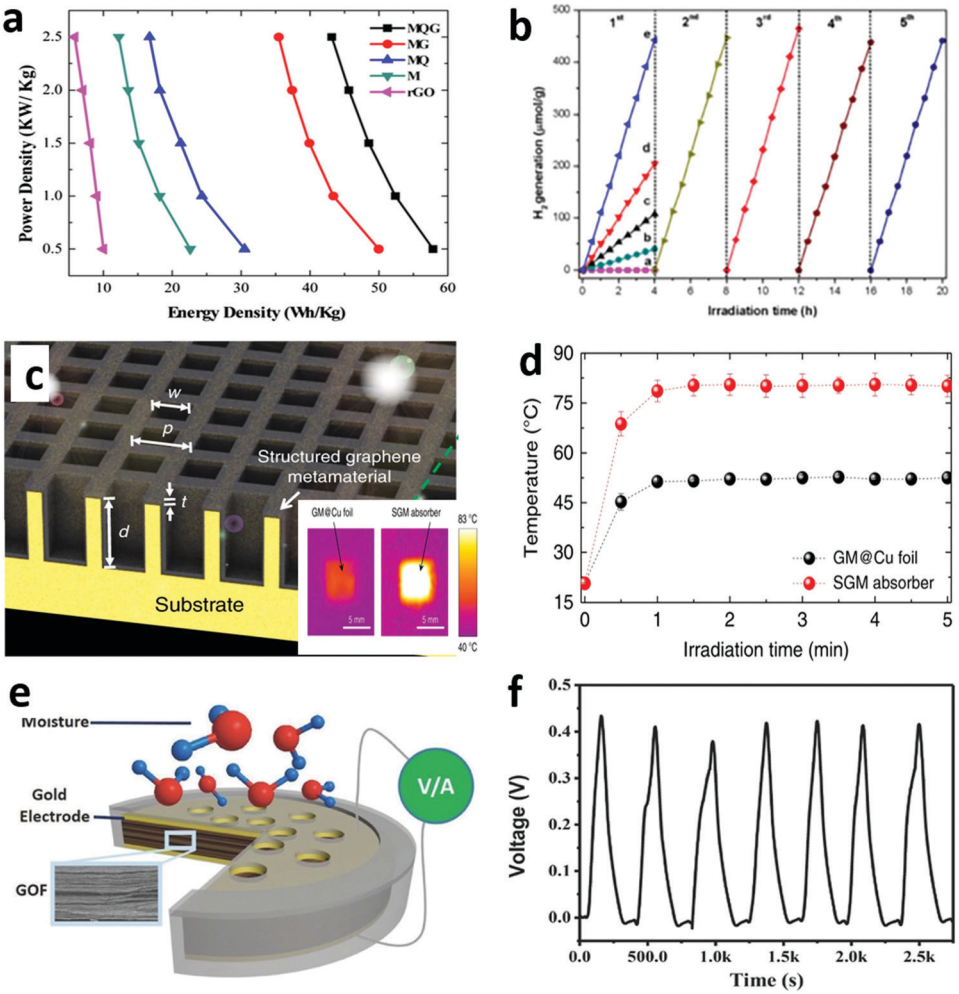

Fig. 9 GRM surface as photo-catalytic and photothermal energy conversion platform, as well as water-related power harvesting. (a) Rate performances of rGO enabled electrodes at various current densities. (Reproduced with permission.[260] Copyright 2020 Elsevier.) (b) Stable H_2 generation from water under visible-light irradiation using (i) MoS_2, (ii) g-C_3N_4, (iii) Fe_3O_4@SiO_2@MoS_2, (iv) MoS_2/g-C_3N_4, and (v) Fe_3O_4@SiO_2@MoS_2/g-C_3N_4. (Reproduced with permission.[263] Copyright 2019 Royal Society of Chemistry.) (c) Experimental setup for solar steam energy generation. Inset shows thermal images of the flat graphene enabled metamaterial on Cu foil and SGM absorber under sunlight illumination in an open environment. (d) Temperatures of the flat graphene enabled metamaterial on Cu foil (black) and SGM absorber (red) after various periods of illumination. (Reproduced with permission.[264] Copyright 2020 Nature). (e) Schematic of a GO-enabled MEG setup. (f) V_{oc} output of the GO generator in response to the periodic change of relative humidity (RH ~70%) at room temperature. (Panels e and f are reproduced with permission.[265] Copyright 2018 WILEY-VCH Verlag GmbH & Co. KGaA, Weinheim.)

concluded that rGO and N-GQDs supporter played a key role in decreasing the charge transfer resistance.

Graphitic carbon nitride (g-C_3N_4) is a metal free photocatalyst, while exhibiting good chemical stability, low-cost and narrow band gap of 2.7 eV. It is therefore a promising H_2 generator under solar light irradiation.[255] The performance of bulk g-C_3N_4 is restricted by the high recombination rate of the excited charge carriers, a specific surface area smaller than other 2D materials, and low solar light absorption efficiency.[263] In order to overcome these obstacles and improve the photocatalytic activity, various strategies have evolved, including surface modification,[266,267] mesoporous structures,[268] doping[269,270] and design of heterojunction composites[271] obtained by mixing g-C_3N_4 with rGO or GO, which function as either a support material, an electron collector or carrier.[100,272,273] Hybrid composites were prepared based on a mixture of Fe_3O_4, SiO_2, MoS_2 and g-C_3N_4 (termed as Fe_3O_4@SiO_2@MoS_2/g-C_3N_4), exhibiting an extended range of light response, an intimate contact interface, improved separation speed of carriers, and higher photocurrent density.[263] Specifically, a H_2 evolution rate of 110.72 μmol h^{-1} g^{-1} was measured under visible-light, which was approximately 11- and 4-fold higher than those of pure g-C_3N_4 and Fe_3O_4@SiO_2@MoS_2, respectively (Fig. 9b). The improved performance characterized by good recoverability and photoactivity, is attributed to the unique transfer mechanism of the photogenerated electrons in the MoS_2/g-C_3N_4 photocatalysts, where carriers migrate from the conduction band of MoS_2 to the valence band of g-C_3N_4.[274]

Phosphorene based on its inherent properties displays a wide light absorption range from ultraviolet to near-infrared

making it very appealing for solar photocatalysis applications.[275–279] However, it is considerably less stable than graphene, with a tendency to oxidize towards P_xO_y. The oxidative degradation of the material in ambient conditions is still a puzzling obstacle towards practical applications.[206] The presence of the lone pair of electrons on the edge of the phosphorene (the active sites of oxygen adsorption) is suggested to be the cause of the degradation process. The development of effective passivation strategies is under continuous investigation with efforts targeting encapsulation,[280–282] 2D heterostructure formation,[283] doping or chemical modification of the crystal edges.[206,284]

The photothermal materials absorb incident light energy and convert it to heat. They are useful in many fields such as solar energy harvesting, photothermal therapy, water desalinization, just to name a few.[285,286] Depending on the application type, specific optical absorption properties of GRM are required. For example, materials having an E_G corresponding to the visible region are promising in solar energy harvesting and water desalinization. 2D materials used in photothermal therapy are required to absorb near-infrared photons (700 nm to 980 nm, 1000 nm to 1400 nm)[287] that can penetrate biological tissues. Upon irradiation with an intense light source they release heat in the form of vibrational energy, which kills the targeted cancer cells. Since they are cleared by renal filtration it is not a surprise that small size materials have low tissue retention and are preferred for this reason. BP has wide absorption across the ultraviolet and near-infrared region including the optimal biological window. BP has been studied in the form of quantum dots,[288] integrated in nanospheres[289] and BP-Au nanosheets[290] with high photothermal ablation efficiency. Remarkably, while the degradation of BP in water and oxygen limits many of the applications of the material it also provides a convenient way to biodegradability because BP is eventually oxidized *in vivo* to nontoxic products.[206,289] Graphene attracted great attention as a photothermal absorber when a high uptake by tumors was reported, based on *in vivo* studies in mice. The researchers used small graphene sheets with polyethylene glycol functionalization for better stability in biological solutions. Irradiation with 808 nm laser at a low power density of 2 W cm^{-2} resulted in the photothermal ablation of the tumors.[291] Furthermore, GO, rGO, MoS_2 and the MXene Ti_3C_2 have been also functionalized and effectively tested in analogous ways.[292–295]

The thermal absorption efficiency of Ti_3C_2 is very impressive and the material was estimated to yield 100% thermal energy conversion. To this end, the efficiency of stacked MXene thin membrane with variable thickness was tested for interfacial water steam generation.[296] Using a simple vacuum filtration process, a self-floating MXene-PVDF composite, thin membrane was prepared incorporating variable MXene loading amounts (1.0 and 2.0 mg). This hybrid system showed relatively high diffuse reflection in the visible light range demonstrating an equilibrium temperature around 75 °C, while the reference PVDF substrate had at equilibrium only 30 °C. The experiment revealed that the water evaporation is faster with increasing MXene mass, producing a light-to-water evaporation efficiency of 84% under one sun irradiation, which is among the highest reported values for similar photothermal evaporation systems toward water-based energy conversion applications.

Furthermore, artificially designed assemblies consisting of layered light-responding components arranged in repeating patterns (as metamaterials), were recently reported to demonstrate 90% solar energy to thermal conversion efficiency.[264] The schematic representation of the 3D structured graphene metamaterial (SGM) absorber is shown in Fig. 9c, characterized by the following structural parameters: the depth (d) of trenches, the thickness (t) of the graphene metamaterial layer, the width (w) of the hole, and the period (p) of the structure. Fig. 9d depicts the comparison between the photothermal performance of graphene enabled metamaterial on Cu foil (black data) and SGM (red data) under solar simulator illumination. The temperature of each sample reveals an abrupt increase during the first minute, while thereafter both samples reach a saturation value. The temperature of graphene enabled metamaterial on Cu foil sample increases from 20 °C to ~52 °C, while the SGM absorber is increased significantly up to ~80 °C. This study demonstrated the 3D SGM allows significant improvement of solar energy collection efficiency and reducing the thermal radiation loss for solar-selective absorption.

3.5 GRM for various forms of water-energy harvesting

Water, that covers more than 70% of the earth's surface, contains tremendous amount of energy in various forms that remains currently unexploited. As a complementary approach to the established renewable energy technologies, energy generated by water constitutes an attractive solution for both distributed miniature energy harvesters and large-scale installations. For up-scaled energy production enabled by a conventional water massive flow, hydroelectric power plants incorporate water turbine-based generators. On the other hand, a great amount of water energy that is still wasted, is also stored in the low-frequency flow of water including the motion of raindrops, tide dynamics, or osmotic effects in salinity gradients found in river/ocean boundaries. Amongst the various means of harnessing electrical power from water energy, evaporation-induced electricity seems to be the most efficient way offering the advantage of independency on weather conditions or day-time/night-time cycle like PV processes. Moreover, during its process the ambient temperature and waste thermal energy are reduced in favour of water circle contributing therefore to less environmental impact.

Osmotic energy (also known as blue or salinity gradient energy) can provide an efficient power source by transforming chemical energy of salinity gradients in useful work – it is estimated based on thermodynamics that 0.8 kW h m^{-3} can be produced at the river/ocean interface, rendering this approach very appealing despite its low magnitude compared to established fossil fuels technologies.[11] The two established approaches for blue energy harvesting are the pressure-retarded osmosis and conventional reverse electrodialysis. Both approaches are based on charged ion driven flow through ion-selective, partially permeable membranes with variable thickness, porous diameter

and density, which separate two reservoirs filled with fresh and salty water generating a chemical potential difference.[297] One advantage of reverse electrodialysis is the direct conversion of water energy into electrical energy that offers large-scale viability, however the requirement of a hydroturbine increases significantly the manufacturing costs of the water-based power plant. Although the aforementioned approaches are very appealing, they require external stimulus of pressure, salinity-gradient, or the development of sophisticated membranes, thereby restricting their current wide usage.[11,50,298]

Other approaches exist with less demanding infrastructure requirements based on triboelectric, electrokinetic, or piezoelectric effects towards transforming the motion of water into electrical energy.[15,299] Specifically, an electronic double layer is formed at the interface between a charged solid surface and a fluid. The structure of this double layer contains a Stern layer sessile on the solid surface and a diffusion layer rich in counterions.[11] Upon an external stimuli, the diffusion layer can be modified generating a relative motion between fluid and solid – a process termed as electrokinetic effect. There is a variety of electrokinetic effects induced by water-solid interactions, including the motion of ionic liquids induced by a pressure gradient through a narrow channel that generates a voltage in the fluid, called as the streaming potential, the drawing or splashing potential enabled by droplets motion that can be used to harvest rainfall energy, as well as a moisture-induced mechanism that is based on materials expansion upon water adsorption and contraction on desorption, outputting mechanical work in analogy to a steam engine.[15,49,299–302]

GRM's peculiar surface properties and their high surface-to-volume atoms ratio provide a versatile platform for energy harvesting on interaction with water unattainable by conventional technologies.[11,15,49,50,297,298] Pivotal role in GRM's water energy conversion properties is played by their enhanced (tribo-) electronic interaction with water molecules. Notably example constitutes the transformation of ambient waste thermal energy into useful work based on natural evaporation-induced electricity with the potential of producing an average energy flux as high as 80 W m^{-2}.[303] This water-based energy generation scheme has been demonstrated both on the level of miniature harvesters (covered in Section 3) and upscaled installations towards on-grid electricity (covered in Section 4).

GRM-enabled membranes for osmotic energy harvesting systems have been demonstrated, exhibiting unique advantages compared to conventional systems. Membranes formed by GRM possess increased surface area, while their suitable functionalization allows much larger pores to be attained minimizing at the same time membrane's fouling effects – all these together have the potential to outperform conventional technologies. Specifically, GRMs have demonstrated several orders of magnitude higher performance than bulky conventional membranes giving a boost on the field owing to their peculiar surface fluid dynamics.[50,297] The molecular thickness of GRMs can strongly increase the ion-concentration gradient leading to large power densities. In a seminal work, atomically thin MoS_2 membranes with nanopores in the range 2–20 nm demonstrated an outstanding power density of 10^6 W m^{-2}. Lower power density values by at least three orders of magnitude, have been reported in other GRM systems including h-BN, GO and graphene, where the high GRM ionic bond character leads to the enhanced conversion efficiency.[297] Furthermore, GRM offer the potential of surface or pores functionalization controlling on demand properties such as superhydrophobicity enabling thus nanogenerators with enhanced efficiencies.[9,15,49,300]

The streaming potential was recently extended to drawing potential that can be used to harvest rainfall energy.[49] A splash between a falling raindrop and tilted graphene generates an electric voltage one order of magnitude higher than that induced by drawing a droplet of similar size, attributed to the high-speed spreading of the raindrop.[11,300,301,304] Compared with droplets, waving water is more abundant and contains much more energy, which can be harvested in a manner like that of the drawing potential.[305] Moisture induced electricity generation (MEG) reports have demonstrated GRM having response to water vapour and a controlled large moisture variation of up to 90%.[15,101,102] In a notable example, a direct electric generation process has been demonstrated in a GO structure.[265] In Fig. 9e, the schematic of a GO-enabled MEG device is shown, where a piece of GO is sealed into a coin battery shell with the inlet of moisture on the top side. Upon the water vapor stimulation and by using a single piece of GO, the directional movement of charged hydrogen ions through the GO film will induce an open circuit voltage output of up to 0.7 V (Fig. 9f) and a short circuit current density of 25 μA cm^{-2}. Benefiting from GRM's tunability, the generated electric voltage of these devices has increased from about 35 mV in 2015 to a considerable value of 1.5 V in only four years. Moreover, large-scale assemblies of MEG have shown adequate output voltage (28 V) and power for driving commercial electronics devices, such as calculators, LEDs, liquid crystal display (LCD), *etc.*, opening the past for self-powered IoT devices and on-grid energy generation, topics that will be discussed in Sections 3 and 4.[15]

4. Self-powered miniaturized devices enabled by GRMs for Industry 4.0

Miniature energy harvesters to be used as energy sources are in urgent need due to the rapid development of wearables and IoT electronics that will allow e-platforms to be applied in the Industry 4.0 revolution. While IBM predicted that by 2035 one trillion IoT devices would be connected to the internet, Global System for Mobile Communications association set a new lower estimate to 25 billion by 2025. These numbers surpass considerably the currently connected IoT devices, estimated in 10 billion, which confirms the slower-than-expected progress of the technology required for its deployment. Powering billions of devices is indeed, one of the most challenging bottlenecks in achieving the future vision of IoT. Most of these devices use a battery as their power source, and therefore by

transforming them to energy autonomous systems offers more comfort for the user by removing any wiring units and the need of frequent battery replacement, allows for lowering installation costs and light weight devices, while eventually reduces the environmental impact of this technology deployment by avoiding any battery usage.

There is abundant ambient energy available to be harnessed by smart harvesters, including electromagnetic radiation, especially at radiofrequencies (RF), bio-mechanical energy, waste thermal energy and various forms of water energy. Mechanical energy harvesters include piezoelectric nanogenerators (PENG) and triboelectric nanogenerators (TENG), whereas thermoelectric generators (TEG) and RF harvesting devices convert thermal and electromagnetic energy to electricity, respectively. The atomic thickness and large-scale manufacturing capability of GRM have inspired novel, emergent ways of energy harvesting that promises not only to provide the required power for IoT systems, but also upon connecting in-series multiple harvesters to contribute to on-grid electricity generation. The enhanced piezoelectric properties of GRM enable their application in flexible PENG and TENG, capable of converting bio-mechanical energy from the ambient environment to electricity by transforming motion and mechanical stress into electrical signal and accumulated charge, respectively. Even though the above harvesters are strongly depending on ambient conditions thus exhibiting variable outputs, these conversion approaches are useful for both indoor and outdoor environments providing an abundant up-scalable source of always-on energy generation.[306,307]

4.1 GRM enabled mechanical energy harvesters

Piezoelectric energy nanogenerators. Monolayers of MoS_2 were used as an active layer in PENG exhibiting a peak output voltage and current of 15 mV and 20 pA, respectively, when strained by 0.53%. Overall, these PENG generated a power density of 2 mW m^{-2} offering an energy conversion efficiency of 5.08%.[196] One route for maximizing the performance of these miniature harvesters is the in-series or parallel connection of multiple devices. Toward this, arrays of four MoS_2 flakes connected either in series or parallel were fabricated demonstrating an enhancement in output voltages or currents, respectively. Fig. 10a shows an image of flexible MoS_2 PENG, where sulfur (S) passivation was suggested as a way to increase the output peak current and voltage by a factor of 3 (100 pA) and 2 (22 mV), respectively, originating in the reduction of the charge carrier density upon S-passivation (Fig. 10b).[308] An optical microscope image of the electrode configuration is depicted in the inset. The measured piezoelectric coefficient of the pristine monolayer MoS_2 is 3.06 ± 0.6 pm V^{-1} (red circle) while that of the S-treated monolayer MoS_2 is 3.73 ± 0.2 pm V^{-1} (blue triangle), which is higher value than that of the α-quartz that is 2.3 pm V^{-1} (black quadrangle).

The observation of the band-piezoelectric effect in biaxial-strained graphene that arises from the charge transfer along a work function gradient, provides a versatile platform for graphene based PENG.[309] A ternary piezoelectric rubber composite enabled by graphene, lead zirconate tinanate, and polydimethylsiloxane (PDMS) was shown to exhibit significant performance enhancement compared to reference material (Fig. 10c).[310] In this configuration, the piezoelectric 2D material acts as the nanofillers of the final composite structure,[311] while the optimized mechanical structure of the metal electrodes (panel I) using symmetric design of serpentine patterns on both sides of the electrodes (panel II) led to excellent stretchability even when mounted on the skin without exhibiting any irritation (panels III and IV). In particular, the graphene embedded ternary composite exhibited a maximum power density of 972.43 μW cm^{-3} under human walking, while demonstrating excellent mechanical tolerance to bending, stretching, and twisting for thousands of cycles.

Following a similar hybrid approach, flexible PENG based on dispersion of BN flakes into an elastomer matrix were reported.[312] The resulted PENG demonstrated an output V_{oc} and I_{sc} reached up to ~9 V and ~200 nA, respectively, depicting output power values of ~0.3 μW. In an attempt to avoid using lead in PENG systems, a directly grown barium titanate nanoparticles on GO were used aiming at the synergistic interplay of the combined materials towards boosting the piezoelectric response of the hybrid PENG.[313] The GRM enabled structure exhibited better morphology due to homogeneous size distribution, passivated oxygen vacancies and better GO crystallinity after hybridization and reinforced mechanical properties leading to enhanced performance. A proof-of-concept demonstration of a hybrid PENG integrated with a wearable glove validated the concept applicability indicating great potential for real applications.

Notably, WSe_2 bilayers produced with turbostratic stacking exhibit strong piezoelectricity (higher compared to monolayers) generating an output voltage of 85 mV and outstanding mechanical durability at a strain of up to 0.95%.[198] The harvested energy of integrated WSe_2 PENG was used to operate a small LCD without external bias. Good piezoelectric performance has been demonstrated also by multilayer InSe integrated in flexible sensors with excellent reliability and stability, enabled by an asymmetric Schottky junction tunable by a piezo-phototronic effect.[209,211] These wearable sensors were used for the real-time monitoring of a human's pulse and breath (Fig. 10d), while benchmarked against commercial products showing competitive performance (Fig. 10e).[26] The piezotronic sensor based on few-layer In_2Se_3 are attached on skin at the wrist (top right) and chest (bottom right) for monitoring arterial pulse and breath, respectively. Left panel in Fig. 10e indicates the measured transient arterial pulse signals, while the right panel the signals zoomed in black rectangle shown in left panel (P1, square symbols; P2, triangle symbols).

PENG fabricated using SnS monolayers were recently demonstrated depicting a peak output voltage of ~150 mV at 0.7% strain, with a significantly higher power density of ~24 mW m^{-2} compared to state of the art devices (Fig. 10f).[314] The voltage output of tensile bending and relaxing mode action are depicted in the inset. The stable and flexible atomically thin SnS having a remarkable carrier mobility of ~35 cm^2 V^{-1} s^{-1} and piezoelectric coefficient of ~26 pm V^{-1}

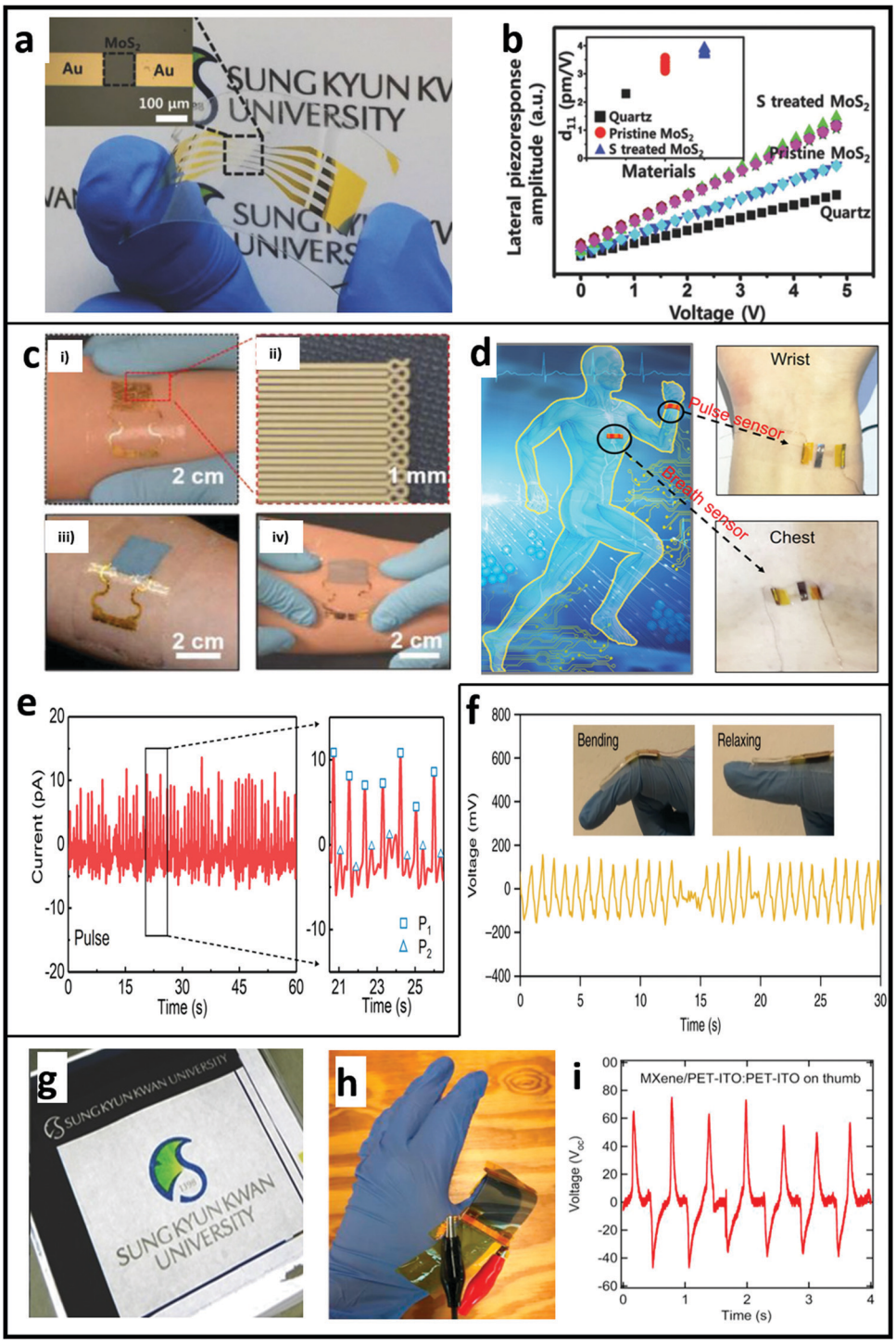

Fig. 10 Small-scale PENG and TENG demonstrators enabled by GRM. (a) Photographic image of the MoS_2 nanosheet-based flexible piezoelectric device on a PET substrate. (b) Lateral piezoelectric response of the pristine monolayer MoS_2, S-treated monolayer MoS_2, and α-Quartz, using lateral Piezoresponse force microscopy methods. (Panels a and b are reproduced with permission.[308] Copyright 2018 WILEY-VCH Verlag GmbH & Co. KGaA, Weinheim) (c) flexible PENG for wearable applications. Panel (i): optical image of the in-plane electrodes for piezoelectric thin films with PI supporting layer and PDMS substrate. Panel (ii): enlarged optical image of the electrode pattern. Panels (iii) and (iv): optical images of the rubbery piezoelectric electronics attached on the surface of forearm, and deformations together with skin. (Reproduced with permission.[310] Copyright 2019 WILEY-VCH Verlag GmbH & Co. KGaA, Weinheim) (d) realtime monitoring of physiological signals (left). (e) Real-time monitoring of arterial pulse signals (panels d and e Reproduced with permission.[26] Copyright 2019 American Chemical Society). (f) Output measurement in a practical wearable device application based on SnS PENG. (Reproduced with permission.[314] Copyright 2020 Nature.) (g) Driving a commercial LCD using graphene enabled TENG. The left panel presents the OFF state, and the right panel presents the ON state of the LCD units. (Reproduced with permission.[126] Copyright 2014 WILEY-VCH Verlag GmbH & Co. KGaA, Weinheim.) (h) MXene-based flexible TENG mounted on a thumb for harvesting energy from simple human muscle movements. (i) V_{oc} varying between −40 and 70 V was generated by the TENG mounted on the thumb. (Panel h and I reproduced with permission.[316] Copyright 2018 Elsevier.)

can be implemented into a variety of systems for efficient energy harvesting. PENGs functionalized with graphene oxide were used to generate a considerable amount of power from various human body movements like walking, foot tapping and bending.[315] The GRM enabled demonstrator exhibited a better electromechanical response of 62 V (peak-to-peak) and 48.3 mW cm^{-2} power generation using finger tapping as compared to 20 V and 23.4 mW cm^{-2}, respectively, for the reference sample. Demonstrations of such devices in sensing and energy harvesting from daily body motion indicate potential applications in self-charging wearable electronics for healthcare monitoring and in skin-electronics related areas.

Triboelectric energy nanogenerators. Graphene and its derivatives, taking in advantage of their flexibility, durability and high transparency, have been also used in TENG. This dual functionality was studied by Kim *et al.* combining graphene layers with a PET film resulting in flexible devices with impressive performance, namely output voltage 5 V and current density 0.5 μA cm^{-2}.[126] As a proof of concept, they were able to power an LCD screen without any external energy source (Fig. 10g). The LCD screen was turned on when the TENG were stressed vertically therefore outputting the required threshold voltage. In another report, α TENG, enabled by a R2R transferring of CVD grown graphene to plastic substrates, was operated as a wearable device harvesting energy by the movement of a wrist, exhibiting maximum output voltage and current density of 22 V and 0.075 μA cm^{-2}, respectively.[64]

In a recent study, TENG were fabricated incorporating fluorinated MXene (Fig. 10h) exhibiting superior triboelectric behaviour with high voltage up to 650 V and an output current density of (0.6 μA cm^{-2}) (Fig. 10i).[316] Their performance was comparable to the widely used negative triboelectric polytetrafluorethylene and capable of harvesting electrical power from simple muscle movements (*e.g.*, texting) even when the device is flexed by ~30°. An ultrathin, flexible and transparent TENG based on combining graphene and parylene films was recently developed.[82] This GRM-enabled TENG has a good mechanical stability and fast response when triggered under vertical impacts at different frequencies. Owing to its ultrathin characteristic and biocompatibility, this TENG could be conformably attached onto the finger joint for bending detection, showing application potential for attachable curvature monitoring in various situations.

4.2 Waste thermal energy harvesters enabled by GRM

A graphene-based flexible TEG consisting of seven units with a wristband-type structure was fabricated by assembling an rGO film on a 3D-printed PDMS grid.[232] The schematic of this graphene-based TEG is shown in Fig. 11a. This flexible demonstrator exhibited an output voltage of 57.33 mV g^{-1} at ΔT of 50 K, while a peak power density of 4.19 μW g^{-1} is achieved at temperature of 15 °C (Fig. 11b). Nanoporous graphene was also incorporated in a TEG structure by Yang *et al.*, as depicted in Fig. 11c.[317] The TEG is comprised of two graphene-based electrodes each one contacting the hot and cold sides, respectively. Due to the high σ and large specific surface of nanoporous graphene-based electrodes, a voltage of 168.91 mV was obtained under ΔT = 35 K, corresponding to a S of 4.54 mV K^{-1}, much larger than those of the traditional TEG.

Recently, a solar TEG system mounted on window-shades consisted of 15 undoped graphene bars in-series was demonstrated. In Fig. 11d, a schematic of the TEG with corresponding electrodes' structure, as well as a thermal image under sunlight and the principle of operation of the experiment are shown.[318] Each graphene bar had one end exposed to a solar simulator (under illumination of AM 1.5G) generating 0.25 mV output voltage. By applying 5× light concentration, the output voltage was further enhanced to 0.85 mV resulting to a Seebeck coefficient of about 50 μV K^{-1}. Under daily light experiments, the highest generated voltage was reported to be 1.87 mV (52.6 mV m^{-2}), opening the path for novel building integrated energy conversion technologies. Moreover, in the same study, another application of GRM-enabled TEG consisting this time of six graphene films connected in series was reported. This flexible TEG with a thickness of 100 μm was integrated in a smart phone (Fig. 11e) aiming at not only dissipating the heat generated by the device but also recycling thermal energy. The maximum output TE voltage during the device operation was reported to be 1.3 mV (Fig. 11f). The direct correlation between the output voltage and the phone temperature revealed that the core temperature of phone was decreased by about 1.4 °C after inserting the graphene film revealing the high potential of the approach.[318]

As a demonstration of a functional all-printed TEG device, a structure consisting of 20 inkjet-printed graphene legs connected by inkjet-printed silver was reported (Fig. 11g).[77] The corresponding Seebeck coefficient of a single leg was calculated at 55.4 μV K^{-1} (Fig. 11h). A direct comparison of the reported Seebeck coefficient values as a function of the electrical conductivity between several recent studies is shown in Fig. 11i. This summarizing figure compares the room-temperature TE properties of inkject-printed graphene (red data), large-area solution-processed graphene (green data), other 2D material (TMDs, purple data), and graphene-conductive polymer films (GNC, blue data) in comparison with established tellurides TEGs (orange data). Dashed lines represent contours of constant power factor. The benchmarking indicates that inkjet-printed graphene exhibits the best TE power factor at an ≈230% improvement, while concurrently achieving the highest Seebeck coefficient among the solution-processed graphene structures. While the performance is found to be comparable to those of state of-the-art graphene-conductive polymer films, the thermostability and mechanical durability of all-graphene structures present a clear advantage over polymeric materials and conventional Bi_2Te_3. Furthermore, inkjet-printed graphene surpass the inorganic semiconducting MoS_2 and WS_2 that exhibit high S (≈ 80 μV K^{-1}) but low σ, while the metallic $NbSe_2$ is shown to be moderately higher in performance due to its high σ regardless of its low S (≈14 μV K^{-1}).[77]

4.3 GRM enabled RF energy harvesters towards 5G era

The rapid development of telecommunications and the associated photonic integrated circuits technology, pinpoints RF

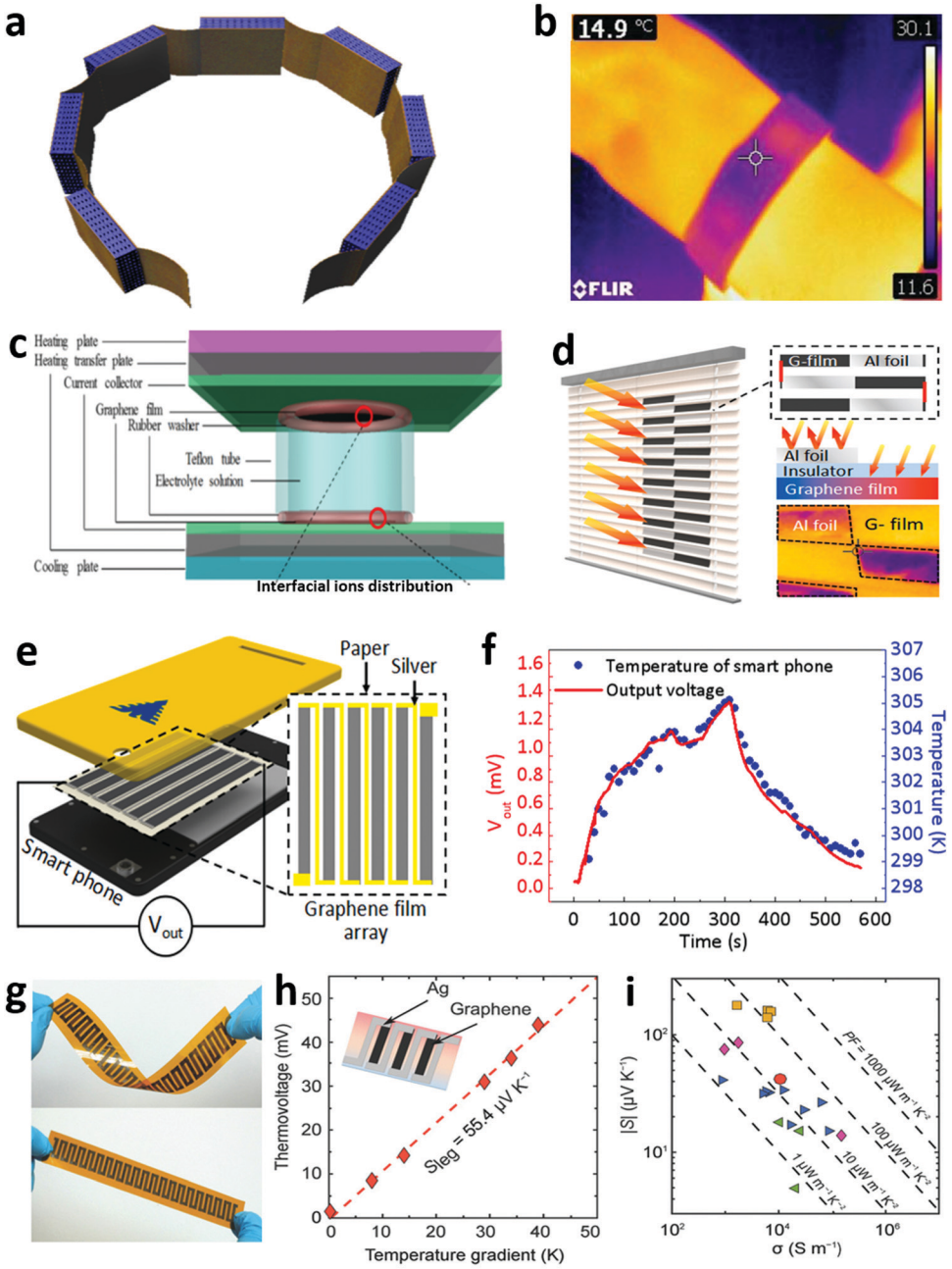

Fig. 11 Small-scale demonstrators of TEG energy converters enabled by GRM. (a) Schematic of the design of the graphene-based TE generator. (b) Thermal infrared spectrum of the generator of a wristband type. (Panels a and b are reproduced with permission.[232] Copyright 2018 Elsevier) (c) schematic illustration of the closed thermoelectric cell. (Reproduced with permission.[317] Copyright 2019 American Chemical Society.) (d) Graphene film used on mobile phone cooling and radiative TE generation. (f) The voltage output measured with different temperatures of the smart phone. (g) Photographs of an inkjet-printed device consisting of 20 silver and graphene legs bent (above) and as is (below). (Panels d–g are reproduced with permission.[318] Copyright 2019 Elsevier.) (h) Voltage response of the device as a function of temperature gradient. Inset: A schematic image of the printed device geometry. (i) $|S|$ *versus* σ for different printed TEG technologies. (Reproduced with permission.[77] Copyright 2018 WILEY-VCH Verlag GmbH & Co. KGaA, Weinheim.)

energy as a very promising energy source. RF signals possess a long-range propagation and their ubiquity nature renders a perfect match for achieving wireless power solution for autonomous IoT devices within 5G technology era. Converting RF energy into DC power is usually achieved by rectennas, a system consisted of an antenna for collecting electromagnetic radiation in the form of alternating current waves from the environment, that are fed into an ultrafast diode with nonlinear current–voltage characteristics. This non-linearity is a requirement for RF signals rectification process that generates eventually the DC power that can be used to power electronic circuits.

2D materials including graphene and MoS_2 have been reported to be very promising for fabricating high performing flexible RF diodes, a key element towards rectenna development.[319] A breakthrough on a fully flexible and integrated rectenna based on MoS_2 monolayer was recently demonstrated.[13,320] The device schematic of the GRM-enabled rectenna is shown in Fig. 12a. The output voltage as a function of the input RF power is presented in Fig. 12b, delivered to the device at four different frequencies (2.4 GHz, 5.9 GHz, 10 GHz and 15 GHz).

Using this novel rectenna setup an output voltage of 3.5 V can be achieved with an input of 5 mW RF power, demonstrating a 40% the maximum output efficiency as

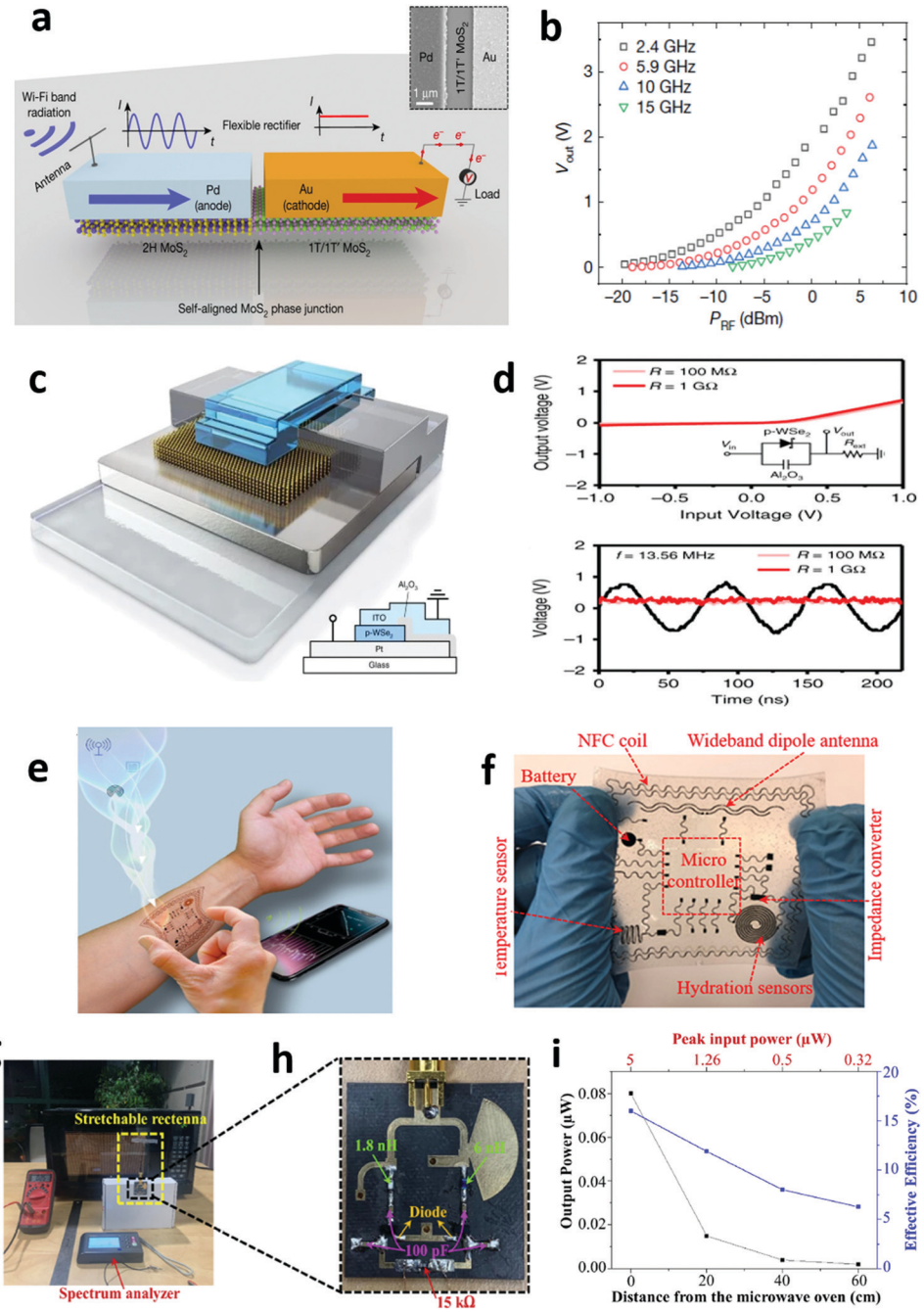

Fig. 12 RF energy harvesting devices enabled by GRM (a) flexible rectenna based on a MoS_2 Schottky diode. (b) Output voltage at variable frequency. (Panels a and b) are reproduced under a Creative Commons Attribution License (CC BY 4.0).[322] Distributed by Exclusive Licensee Science and Technology Review Publishing House. (c) Device schematic of WSe_2 Schottky diode. (d) DC/AC characteristics of ITO/p-WSe_2 Schottky diode. (Panels c and d are reproduced with permission.[321] Copyright 2020 Nature.) (e) Illustration of the laser fabricated device enabled by graphene for wireless communication and ambient RF energy harvesting. (f) Laminating/transferring the device on flexible substrates. (g) Experimental setup to measure the energy harvesting performance of rectennas. (h) A rectifier is designed to match 50 U input over the frequency from 2.0 to 2.5 GHz. (i) Measured output power and effective efficiency as a function of the peak input power. (Panels e–h are reproduced with permission.[19] Copyright 2021 Elsevier.)

compared to 50–60% for conventional, expensive, and complex CMOS rectennas. Furthermore, the demonstrated cut-off frequency of 10 GHz allows a flexible rectifier to operate in the X-band under zero external bias, thus going beyond rigid silicon-based Schottky diodes.

A monopole patch RF antenna based on 2D $NbSe_2$ was recently reported to achieve an outstanding performance.[321] A 3D device schematic diagram along with 2D device cross section is shown in Fig. 12c. The Static V_{in}–V_{out} curve performed by sweeping V_{in} from −1 to +1 V is presented in the top panel of Fig. 12d. In the inset, the device circuit is schematically shown, where an external resistance of 100 MΩ and 1 GΩ is used. In the bottom panel of Fig. 12d, V_{in} (black)–V_{out} (red) plots are depicted revealing a half-wave rectification obtained from the diode circuit when a parallel capacitor is connected at a frequency of 13.56 MHz. This GRM enabled antenna, despite its thickness is below the skin depth of metal antennas, demonstrated exceptional performance characterized by a small return loss (−46.5 dB), high radiation efficiency (70.6%), and frequency tunability (from 2.01 to 2.80 GHz).

A solution processed $Ti_3C_2T_x$ MXene microstrip transmission line was recently reported to enable low-energy attenuation and patch antennas with high-power radiation at frequencies from 5.6 to 16.4 GHz.[322] The radiation efficiency of a 5.5 μm thick MXene patch antenna manufactured reached 99% at 16.4 GHz, which is about the same as that of a standard 35 μm thick copper patch antenna at about 15% of its thickness and 7% of the copper weight. Moreover, in another study, a reliable excellent Schottky junction and an ohmic contact to WSe_2 were successfully achieved using conventional device fabrication processes compatible with semiconductor industry.[323] The demonstrated 27.1 GHz cut-off frequency enabled by WSe_2 demonstrators is matched with 5G era wireless communication, being the highest cut-off frequency among reports enabled by 2D material or 3D thin-film-based diodes.

Very recently, an all-laser-fabrication approach was demonstrated for manufacturing multifunctional flexible platforms consisting of stretchable wideband antennas and rectennas for wireless communication and ambient RF energy harvesting.[19] Their holistic approach is schematically presented in Fig. 12e, that extends from individual components to integrated system, consisting of conductive traces and contact pads, various sensing modules, storage units as well as complementary communication and powering modules (*i.e.*, NFC coil for near-field and dipole antenna for far-field). The final stretchable prototype can be transferred onto stretchable substrates, as shown in Fig. 12f, while each individual component has been separately investigated. An integrated temperature sensor designed in the Archimedean spiral demonstrated linear response in the temperature range from 0–100 °C. Moreover, this sensor showed a frequency-dependent increase in the measured capacitance as the relative humidity increases, while demonstrating reliable sensing performance under deformations.

Within the prototype, a stretchable rectenna is formed by connecting the stretchable wideband dipole antenna with a rectifying circuit (Fig. 12g). To test the energy harvesting performance of the rectenna, a microwave oven was used as a convenient radiation source (Fig. 12h). This system demonstrated an impressive effective efficiency of ∼10% at a peak input power of 1 mW, as shown in Fig. 12i, taking in consideration the additional loss in the antenna and matching circuit. This value exceeds the performance of earlier reports,[13] while owing to the stretchable wideband rectenna the reported efficiency is larger than the theoretical limit of 0.1% that is estimated for RF-DC conversion of a Schottky diode at a single frequency in mW operation.

4.4 GRM enabled water-energy harvesters

Many PENG and TENG have been explored to harvest various forms of water energy stored either in oceans, rivers or even in atmosphere in the form of humidity. Notably, the potential of water-energy harvesting technology has been demonstrated as a proof of concept in small scale devices (an example was shown in Fig. 4e), however in-series connecting a multitude of tiny water-energy harvesters has strong potential towards upscaled on-grid energy generation as will be discussed in Section 5.

High electric voltages up to 1V have been reported by dipping carbon black thin sheets (mixture of graphene and multilayer graphene) into water,[304] where pulling a GRM out of a liquid surface produces an inverse voltage due to a discharging process at the boundary.[49] Notably, a power density up to 1 mW cm^{-2} can be realized in an oxide framework at a moisture variation of 80%. The evaporation- or moisture-induced electricity enabled by multiple GRM harvesters in-series connected has been demonstrated as a viable route to power various IoT devices. Examples include thin film transistor LCDs and light-emitting diode.[49] Another unconventional, emerging energy harvesting approach enabled by GRM and their interaction with liquids, is based on human biofuels cells.[324] Specific electrodes using GO were developed and incorporated in perspiration-powered electronic skin that harvests energy from human sweat. The prototype delivered a record-breaking power density of 3.5 mW cm^{-2} for using human sweat and displayed a very stable performance during a 60 hour continuous operation, opening the path for monitoring of key metabolic biomarkers.

A large-scale integration of GO power-generating device arrays enabled by a directional migration of ionized H^+ ions in moisture presence, was demonstrated by Liang *et al.*[20] The electrodes and the GO active materials were printed on a paper substrate using a three-step screen printing process. In Fig. 13a, the manufacturing procedure is schematically depicted including the printing of the bottom electrodes, the GO layers and the top electrodes. At the bottom side of Fig. 13a, a photograph is shown of the final printed demonstrator consisting of multiple in-series-connected devices. The sizes and number of the integrated devices can be adjusted on demand depending on the targeted applications, leading to upscaled output power. Two, three, four, and five in-series connected devices exhibited voltages of 0.8 V, 1.2 V, 1.6 V, and 2.0 V, respectively, following a linear law of summation. As a proof of concept, the GO-enabled prototype was used power an electric calculator, as shown in Fig. 13b, while being foldable and easily integrated into pockets (Fig. 13c) targeting wearable applications.

Yang *et al.*, recently demonstrated a series of rollable, stretchable, and even 3D space-deformable graphene-based

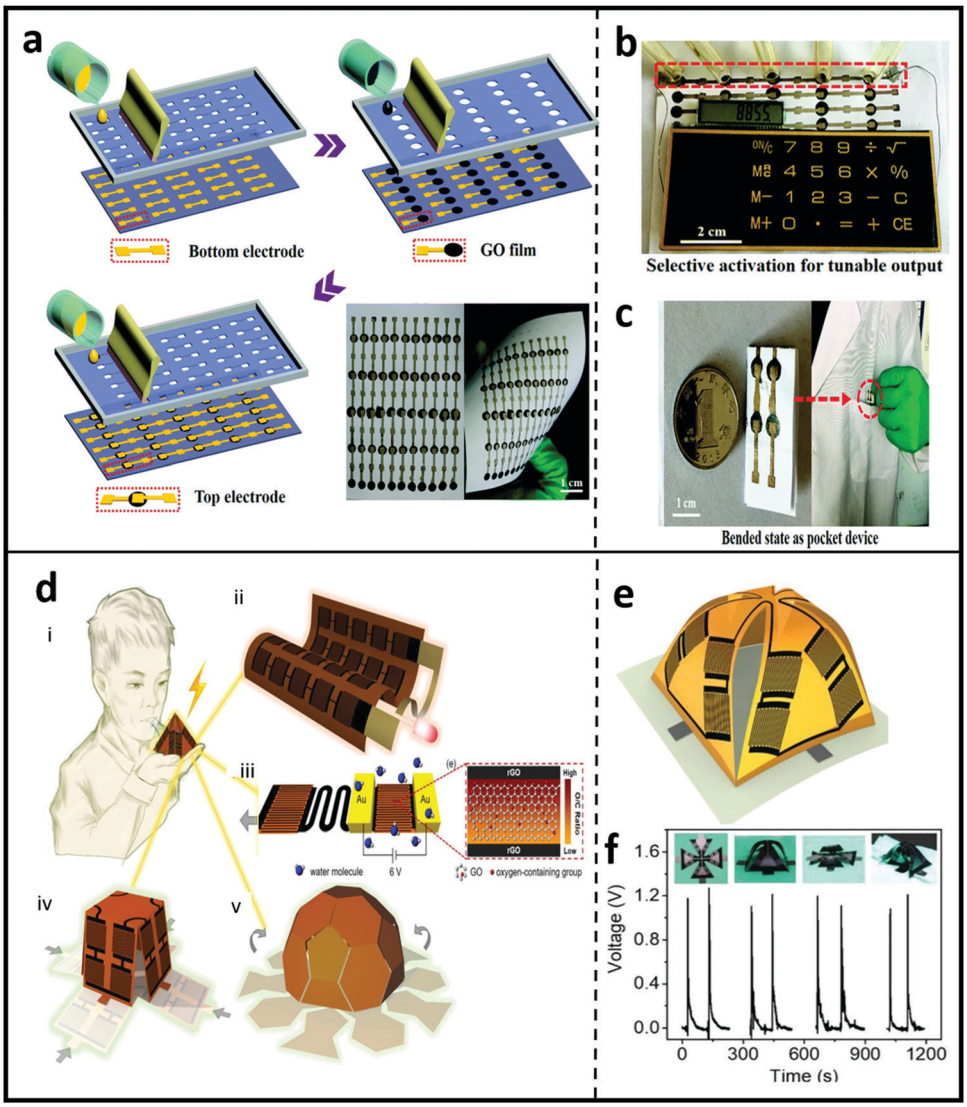

Fig. 13 GRM enabled water energy harvesting. (a) GO power-generating device arrays on paper. (b) A photograph showing a working calculator powered by five GO device units connected in series. (c) Foldable and portable performance of the device arrays. (Panels a–c are reproduced with permission.[20] Copyright 2018 Royal Society of Chemistry.) (d) Graphene based hydroelectric generators. (e) Schematic diagram of 3D-assembled generators into a pyramid structure. (f) V_{oc} of pyramidal under expanded, assembled, uniaxially stretched, and contracted states (panels d–f are reproduced with permission.[21] Copyright 2019 WILEY-VCH Verlag GmbH & Co. KGaA, Weinheim).

hygroelectric generators (Fig. 13d).[21] Serially-connected hygroelectric generators directly embedded in the flexible GO film, exhibited an excellent electricity generation ability without any significant performance under extreme bending conditions. Specifically, the schematic diagram of the operation mechanism of these generators enabled by relative humidity changes is shown in panel i. Their large-scale, rollable integration onto flexible substrates is presented in panel ii, whereas a stretchable geometry with serpentine bridge–island structure is shown in panel iii. Pivotal role in the generator operation is played by a gradient distribution of oxygen containing groups in GO film between cathode and anode induced by a moisture–electric annealing polarization process. As a proof of concept, a light-emitting diode bulb was powered in atmosphere under 100–2000% strain change. Moreover, their 3D deformable configuration of a cube (panel iv) and football structure (panel v) is also presented in Fig. 13d. Fig. 13e shows an example in which the prototype of 16 generators continuously transforms between planar film and 3D spatial pyramid structure under tension or contraction state. In the various forms of the structure, the V_{oc} is maintained between 1.05 and 1.27 V, as depicted in Fig. 13f, being a very promising performance for applications in the field of deformable power supply systems, self-folding electronics and energy harvesting under complex conditions.

5. Large-scale energy harvesting installations enabled by GRM

A prerequisite for realizing up-scaled renewable energy sources enabled by GRM is to attain large-scale batch production of

materials with high uniformity and reproducibility. In Section 2, different methods for upscaled GRM production were presented also demonstrating compatibility with established CMOS devices processing. This advancement therefore opens the path for GRM's industrial level integration targeting energy conversion applications eliminating concerns regarding the commercialization potential of this technology. Moreover, the technological progress on GRM also offers the possibility of realizing emerging device concepts not attainable by current material technologies.

Central to large-scale energy harvesting technologies is developing scalable and cost-efficient ways to utilize solar energy, which is the most abundant form of available energy. A conservative plan for the near future is the production of ~10 TW based on PV technologies by 2030, and between 30 to 70 TW by 2050. By achieving this goal, PV systems along with other complementary technologies such as fuel cells, power to gas/liquid fuels/chemicals, could almost cover the needs of global energy consumption.[9] Quite recently, GRM-enabled, large-scale PV and FC installations were demonstrated as platforms for direct solar energy harvesting and methane or H_2 generation, respectively. Moreover, novel energy harvesting methods enabled by in-series connected multiple GRM-based harvesters have shown the potential of a complementary path towards on-grid electricity generation, fulfilling the vision for the cities of the future as schematically described in Fig. 1. Smart ways of implementing simultaneously more than one energy conversion approaches in a single device configuration is presented as a promising route for upscaled output power.

5.1 GRM enabled PV modules and panels towards on-grid energy generation

The driving force in current Si PV technology is the reduction of the cost per watt while improve the watt per gram utilization. The latter urges for the active layer thickness reduction.[9,10,325] It is noteworthy to mention that thin-film, lab-scale PePV and OPV with high efficiencies have been already obtained leading to record PCE values of 25.2% and >18%, respectively.[326–331] Intensive developments are continually being made for reducing the PCE gap between small and large-area modules, while achieving a high throughput, high stability, and minimum batch-to-batch variation, at lowest possible manufacturing cost. The atomically thin bodies and high flexibility of GRM make them the obvious choice to be integrated into PePV or OPV, serving as a complementary approach to Si for future-generation PV technology. The outstanding features of scalability, modularity, and R2R-compatible fabrication of GRM promises a key role in the future ultralight PV technology.[3,41,64,131,332–335]

The production cost of the organic hole transport layer and the noble metal (Au or Ag) used as electrode in these devices, counts for about 64% of the total raw material cost of these 3rd generation PV technologies.[336] Carbon was reported to be the most suitable electrode material to replace noble metals, being earth abundant, cheap, chemically inert, highly conductive and flexible. The current certified highest PCE of carbon-based PePV is 17.8%,[337] while exhibiting a high device stability allowing for more than 10 000 hours operation at 55 °C.[338,339] In a longer term, single or few layer CVD grown graphene could be the ideal carbon-based electrode replacement. The emerging GRM-enabled PePV and OPV technologies may not replace Si but instead operate in synergy within a PV tandem configuration. Efficiencies exceeding 27.0% have been already demonstrated in monolithic tandem cells.[340] On the other hand, GRM enabled PVs may also fit well into application areas where devices need to be fabricated on flexible supports *via* inexpensive techniques.[185,325,340] Notably, semi-transparent flexible PVs are of great interest due to their attractive application in building-integrated PV.[3,335]

Very recently, di Carlo *et al.* demonstrated the incorporation of graphene and functionalized MoS_2 in PePV modules (Fig. 14a).[39,44] The GRM were incorporated across different sections of the device (electron and hole transport layers) having a positive impact both on module lifetime stability and overall PCE. Notably, the upscaling of this technology was also demonstrated by achieving a PCE of 13.4% and 15.3% on active areas of 108 cm^2 and 82 cm^2, respectively (Fig. 14b). The structure based on the $cTiO_2/mTiO_2$ + G layer and c TiO_2 + G/TiO_2 + G are named PSM-B and PSM-C, respectively, while the fully optimized 2D material-engineered structure, including the $fMoS_2$, is termed PSM-D. At the time of publication of this report, this performance was translated to a record-high active area-indexed aperture PCE of 1266.5% cm^2. On the side of device stability, the GRM-based modules showed a remarkable stability under prolonged (>1000 h) thermal stress test at 65 °C (ISOS-D2), representing a crucial advancement in the exploitation of GRM enabled PePV. Similar graphene-enabled PePV were manufactured and integrated with Si PV, within a tandem structure, using a specialized lamination process.[45] The design and assembling of the two-terminal perovskite/Silicon tandem solar cells is shown in Fig. 14c. The mechanical stacking of sub-cells was implemented by applying pressure over their contact area. The performance of the tandem cells is shown in Fig. 14d, indicating a 26.3% efficiency (25.9% stabilized) over an active area of 1.43 cm^2 laying the grounds for achieving performances beyond the established one in the market. In Fig. 14e, the EQE spectrum of the Si cell filtered by the graphene-based perovskite top cell is also shown for the analysis of the "current-matching condition."

This research effort was further developed within Graphene Flagship activities‖ leading to the worldwide first demonstration of GRM-enabled standalone Solar park that is currently installed, and under operation, in the Hellenic Mediterranean University campus. The continuous monitoring of the GRM-enabled solar park's performance is providing a better understanding of single panels reliability issues, while the concurrent benchmarking process against commercial PV technologies such as Si, CdTe and CIGS (Fig. 15a) is allowing the assessment of their possible application in future PV system for on-grid electricity generation. The solar farm is consisted of 360

‖ https://graphene.azurewebsites.net/Graphene-Flagship-Annual-Report-2020/#page=52.

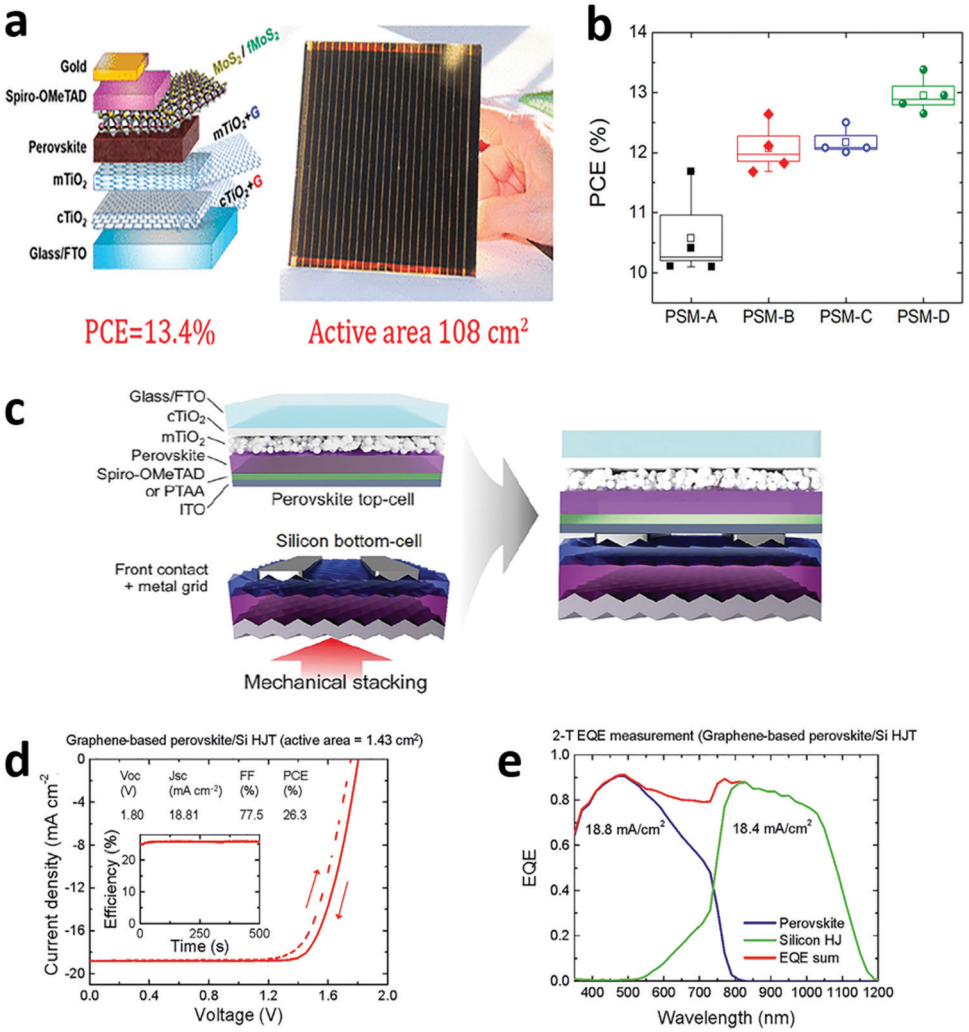

Fig. 14 Upscaled PV modules and Si-perovskite tandem PV cells enabled by GRM. (a) Photograph of a representative large-area graphene-enabled perovskite solar module. (b) PCE for the various modules extracted by the corresponding *I–V* characteristics under 1 Sun illumination. (Panels a and b are reproduced with permission.[44] Copyright 2019 American Chemical Society.) (c) Graphene enabled perovskite/silicon tandem solar cell. (d) *J–V* characteristic of graphene-based perovskite/Si tandem solar modules. The inset shows the PCE measured over time at maximum power point. (e) External Quantum efficiency spectra of the stand-alone graphene-based perovskite and Si sub-cells. (Panels c–e are reproduced with permission.[45] Copyright 2020 Elsevier.)

modules in total, integrated within nine graphene-perovskite panels with a total surface area of 4.5 m^2. The graphene-perovskite panels technology is expected to significantly decrease the manufacturing cost of energy production toward \$0.03 kW^{-1} h^{-1}.

In another application of GRM for upscaled PV energy production, graphene-based interconnects were prepared to replace conventional Ag grids, aiming to overcome sensitized solar modules degradation.[43] It was demonstrated that this approach prevented the corrosion of interconnects in contact with electrolytic species. In the process of upscaling module dimensions, an enhancement of the aperture power conversion efficiency ~+12% with respect to Ag-based modules was demonstrated, exhibiting 1000 h stability under 85 °C stress test (Fig. 15b). The performance enhancement originates in the increase of the aperture area efficiency with respect to devices with Ag-based interconnects. Moreover, the graphene-based vertical interconnects increase the number of devices passing the dry heat test by 40% (1000 h @ 85 °C), highlighting their effectiveness and mechanical stability. This study paves the way to GRM enabled dye sensitized solar modules technology in building integrated PV and indoor applications.

5.2 Low-cost fuel cells enabled by GRM

Fuel cells convert the chemical energy produced by an electrochemical reaction into electricity. The chemical energy stored within the hydrogen (or methane) that is typically used as a fuel, is directly converted to electricity exhibiting outstanding efficiency up to two-three times larger than that internal combustion engines. Moreover, the FC operation does not produce any greenhouse gas providing a very convenient way to overcome global warming effects and associated environmental issues.

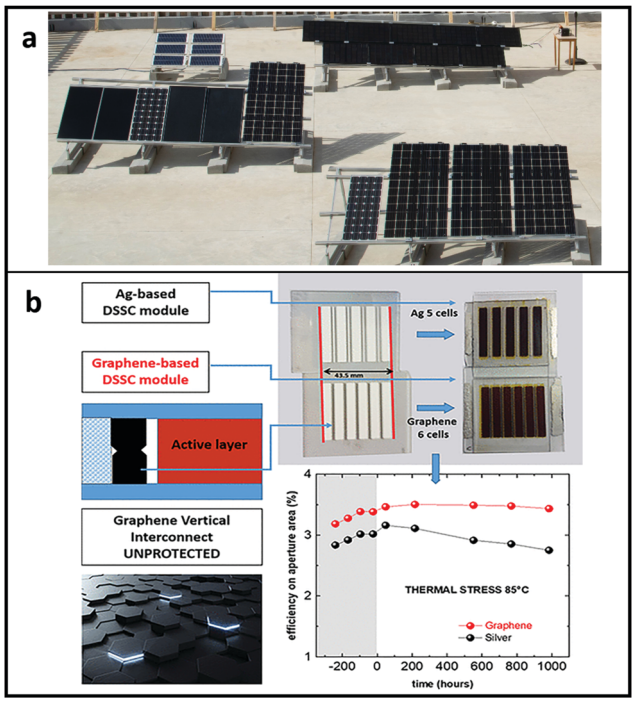

Fig. 15 Large-scale PVs enabled by GRM for on-grid electricity generation. (a) Solar farm infrastructure in Hellenic Mediterranean University for the outdoor benchmarking with traditional PV technologies. (HMU©). (b) Highly stable dye sensitized solar modules with screen printed graphene-based vertical interconnects. (Reproduced with permission.[43] Copyright 2020 American Chemical Society).

A typical FC is consisted of an electrolyte layer being sandwiched between two electrodes, constituting the membrane electrode assembly (MEA). The electrolyte has a three-fold role, namely, to serve as ion conductor, electronic insulator, and a separator for the reactant gases. The fuel is oxidized on the anode surface, and when the system is embedded in an external electrical circuit, induces an electron flow that reduces O_2 at the cathode electrode. Typical mobile charge carriers such as H^+, OH^-, $CO_2{}^{3-}$, or O^{2-} are simultaneously transferred through the electrolyte contributing to circuit conductivity. Key role in FC performance is played by the MEA that should depict high proton conductivity, electrical insulation, as well as thermal and mechanical strength, while being light weight and flexible. Other important factors are linked with low permeability to reactant species, resistance to fuel transport, and compatibility with different fuels.[51,341]

Depending on the electrolyte, FC are categorized into different types including phosphoric acid fuel cell, proton exchange membrane fuel cells (PEMFC), alkaline fuel cell, solid-oxide fuel cell, *etc.* Among the various FC configurations, PEMFC are compact and a very promising solution to power vehicles such as cars and trucks.[51,342–344] Hydrogen as a fuel and oxygen as an oxidant are the most used reactants in PEMFC. Several shortcomings, however, have long prevented the large-scale deployment of FC technology. From a technical point of view, the main drawbacks are associated with their poor durability and the high manufacturing cost of their functional components. GRM are a viable solution to these bottlenecks allowing significant cost reduction and lifetime stability enhancement. Recent studies have demonstrated the incorporation of GRM into in electrodes, electrolytes, and bipolar plates, taking in advantage of their unique chemical and physical properties.[51,54,341,342] GRM components were used in innovative FC, either based on H_2 or methanol, demonstrating an enhanced performance and reduced manufacturing cost mainly originating in the partial replacement of noble metals usage.

During initial stages of technology deployment graphene-based materials such as GO or rGO, or other GRM were incorporated in FC as a bulk feature. Recently, however, there is a lot of progress in using single layer GRM in ion exchange membranes and hydrogen or methanol evolution catalysts for electrochemical applications.[343–346] Shinde *et al.* recently reported an rGO-based composite membrane exhibiting high proton selectivity by concurrently avoiding any crossover of ionic or molecular species other than protons.[52] Central to this high performance was the dense packing of all components held by rGO sheets. The SEM image presented in Fig. 16a, depicts a film with nacre-like structure having a thickness of 11 μm. The optical image shown in Fig. 16b indicates the upscaled production or rGO-based membranes. FC incorporating the rGO enabled membrane cleary demonstrated enhanced capacity stability, as shown in Fig. 16c. Specifically, the capacity of a 30 mL vanadium flow battery cell as a function of time wasted tested when an rGO-based membrane was placed (blue data), or not (red data), between two Nafion membranes, revealing a much better performance for the GRM enabled devices. The advantages of incorporating GRM materials in up-scalable membranes was demonstrated enabled by a electrochemical pumping scheme for efficient hydrogen isotopes separation.[53] This approach was based on R2R membranes using CVD-grown graphene supported on Nafion, with an estimated graphene coverage as ~95%. This proof of concept demonstrated that GRM enabled membranes preferentially allow protons with potential for nuclear and related industries for heavy-water production.

An ultrathin gas barrier layer was successfully fabricated using a direct spin-coating process, on a PEMFC *via* reconstruction of mechanically exfoliated h-BN nanoflakes.[54] The hBN-coated layer effectively suppressed the gas crossover and inhibited the formation of reactive oxygen radicals in the electrodes without significantly reducing the proton conductivity of the membrane. It was also demonstrated that the structural advantages of h-BN-coated gas barrier layers promise high performance of a unit cell even after an V_{oc} hold test for 100 h. Specifically, the proton resistance and H_2 gas permeability of the h-BN layer-coated membranes depending on the amount of h-BN (samples h-BNO, h-BN1, h-BN3 and h-BN5) were quantitatively determined using electrochemical impedance spectroscopy and gas permeability measurement, respectively, as depicted in Fig. 16d. The impedance spectroscopy analysis shows that the proton resistance slightly increases with weight % of h-BN in the barrier layer probably attributed to multi-stacking of h-BN nanoflakes. The H_2 gas permeability measurements indicated that the permeability of

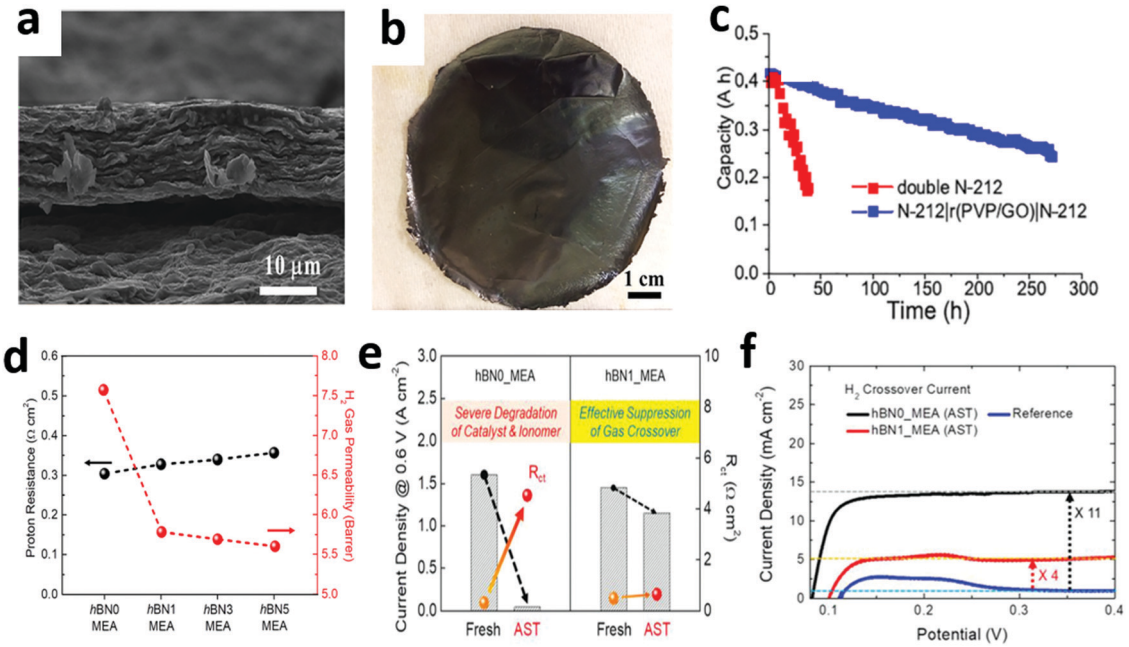

Fig. 16 Large scale GRM enabled fuel cells for on-grid electricity generation. (a) SEM and (b) optical image of rGO enabled membrane. (c) Comparison of capacity stability between reference and rGO enabled membranes. (Panels a–c are reproduced with permission.[52] Copyright 2019 American Chemical Society.) (d) Change in proton resistances (black) of h-BN-coated MEA and H_2 gas permeabilities (red) of h-BN-coated membranes depending on the amount of h-BN nanoflakes used for gas barrier layers. (e) A direct correlation between unit cell performance (current density @ 0.6 V) and charge transfer resistance of the MEA before and after accelerated stress test. (f) Comparison of H_2 crossover current densities of the MEA after accelerated test with that for a fresh MEA without gas barrier layer as a reference. (Panels d–f are reproduced with permission.[54] Copyright 2019 WILEY-VCH Verlag GmbH & Co. KGaA, Weinheim.)

h-BN0 layer, thus the sample without h-BN nanoflakes, was ~7.57 barrer, while h-BN-coated samples exhibit a drop to ~5.5 barrer indicating the beneficial role of h-BN nanoflakes in H_2 gas blocking. Under accelerated stress tests, the charge transfer resistance of h-BN0-MEA sample, as shown in Fig. 16e, was significantly increased from 0.494 to 4.535 Ω cm^2, whereas the h-BN1-MEA sample exhibited a slight increased from 0.318 to 0.652 Ω cm^2. H_2 crossover currents of the MEA were also analyzed indicating a ~11 times increase of current for h-BN0 compared to a fresh MEA, while the current of h-BN1 sample was increased only ≈4 times (Fig. 16f). These results are closely related to the gas blocking properties of the h-BN flakes.

Single-layer graphene and h-BN flakes were also used as a gas barrier layer in methanol FC.[341] This thin barrier layer showed negligible resistance to protons leading to enhanced cell performance by 50%. Uniform and well-distributed Pt nanoparticles grown on an atomic carbon layer were also explored as potential catalysts for methanol oxidation reaction.[347] The as-synthesized catalysts exhibit remarkably higher catalytic activity and much improved anti-CO poisoning ability than the commercial Pt/carbon catalysts, Pt/carbon nanotubes, and Pt/graphene catalysts, adding to the reduced Pt content. Up-scalable synthesis for hybrid Pt nanoparticles coated with GRM nanocomposites has been demonstrated, yielding high catalytic activity and remarkable stability.[54,133,344,347] Hybrid GRM enabled FC electrodes were developed within Graphene Flagship Work Package 11 demonstrating the capability to yield as much as 19 kW per gram of Pt with extended durability originating in the novel nanocomposite functional components. This study led to numerous GRM-enabled products including highly defective graphene supports (*i.e.*, "Hypergraph®" and "Hypergaph Evo®") and corresponding nanocomposites for low-Pt electrodes (*i.e.*, "Hypercat®" and "Hypercat Evo®"). These novel, GRM-enabled FC exhibited a much smaller electrochemical surface area degradation compared to optimised commercial catalyst.

5.3 Up-scalable water-based energy harvesting enabled by GRM

An all-region-applicable, continuous power supply based on GO composite was recently demonstrated.[72] Specifically, a direct-current moist-electric generator based on a porous GO and sodium polyacrylate composite is shown in Fig. 17a. The designed huge aspect ratio and hydrophilic groups collaboratively lead to a high moisture uptake, enabling feasible ion dissociation and effective transport. The harvester is composed of a pair of metal electrodes and porous GO composite. The GO composite has substantial micropores facilitating water molecule absorption and an abundant cross-linking network providing ion channels for fast carrier migration. This harvester can harvest energy from atmospheric moisture regardless of the weather conditions. It was shown to be able of spontaneously producing continuous electric output at all hours of the day and night, demonstrating a comparatively high V_{oc} of ~0.6 V for more than 120 hours. The output of multiple in-series connected

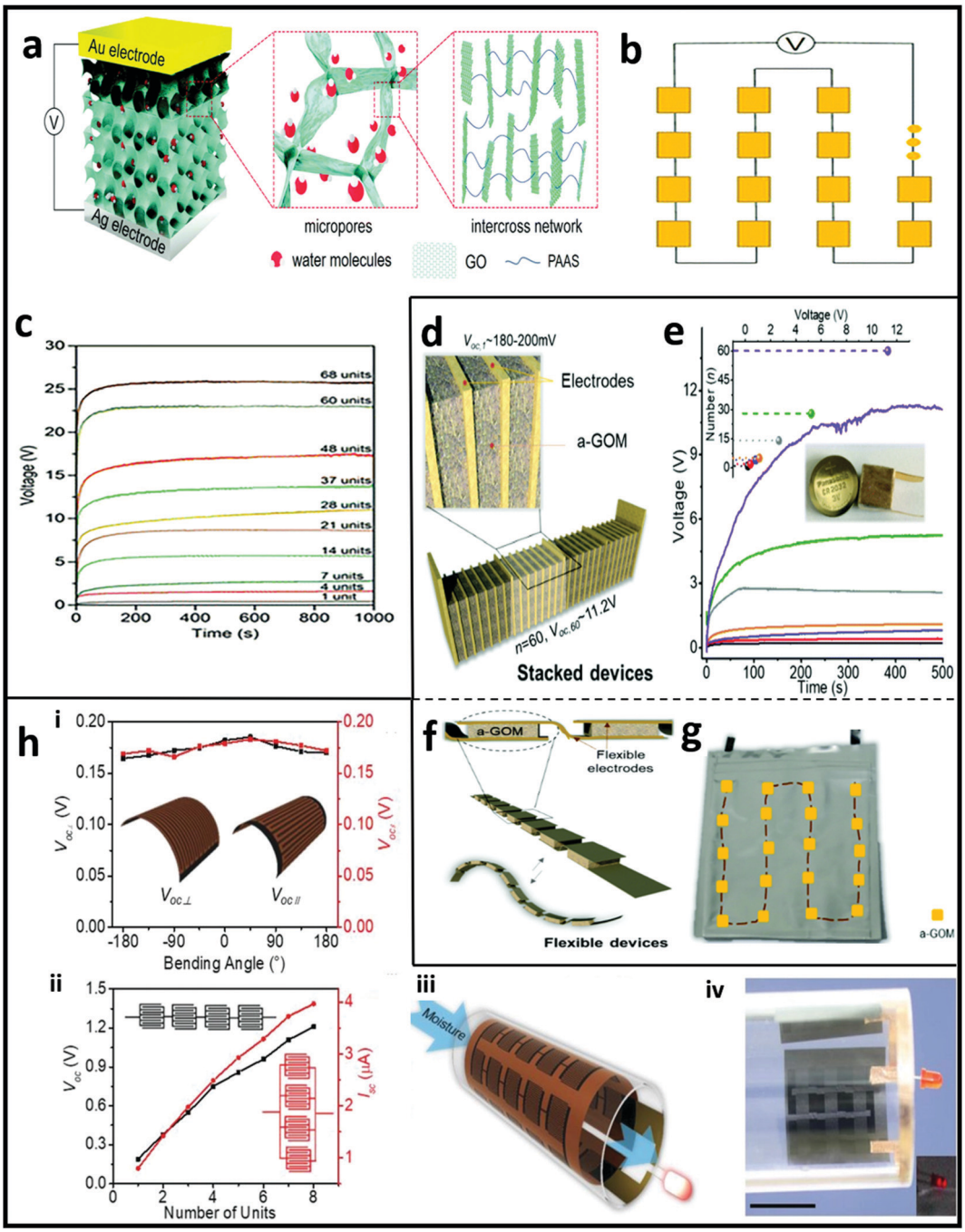

Fig. 17 Multiple harvesters in-series connected for upscaled water-energy harvesting. (a) Schematic and electric output characteristics of MEG. (b) Schematic of multiple connected in series devices. (c) The electric measurement of harvesting units with different connection numbers. (Panels a–c are reproduced with permission.[72] Copyright 2019 Royal Society of Chemistry). (d) Schematic of a MEG based on GO membrane. (e) The measured V_{oc} of stacked device of 1, 2, 4, 5, 14, 28 and 60 units. Inset curve is the V_{oc} related to the number of units in stacked device. Inset photo is the stacked device on the right of a lithium battery coin cell with a diameter of 2 cm. (f) Schematic illustration of soft generator composed of flexible carbon electrodes and GO units. (g) A device (length: 5 cm, width: 4 cm) of plane configuration containing 20 units. (Panels d–g are reproduced with permission.[73] Copyright 2019 Royal Society of Chemistry.) (h) (i) V_{oc} output of GO based MEG at different bending status with parallel ($V_{oc\parallel}$) and perpendicular ($V_{oc\perp}$) to interdigital electrodes. (ii) Series-parallel connection of units. (iii) Schematic and (iv) optical images of rolled GO film with multiple devices powering an LED bulb. (Reproduced with permission.[21] Copyright 2019 WILEY-VCH Verlag GmbH & Co. KGaA, Weinheim.)

harvesters (Fig. 17b) can be easily increased to about 26.2 V (Fig. 17c) *via* simple integration.

Using a similar GO membrane, Cheng *et al.* demonstrated a MEG exhibiting an electrical voltage of up to 450 mV in air without the need of external stimuli such as mechanical movement, light, heat, and liquid water.[73] The schematic illustration of a stacked device is composed of alternative arranged GO membrane and electrodes (Fig. 17d). It is shown that one unit can generate

180–205 mV, whereas multiple stacked devices of sixty units produced about 11.2 V (Fig. 17e), being sufficient for powering many commercial electronic components such as LCDs and light-emitting diodes. A flexible version of the generator is shown in Fig. 17f, demonstrating stable performance even after 100 bending cycles.

Another stretchable graphene-based hygroelectric generator was reported by Yang *et al.*[21] Their generators can periodically produce a peak V_{oc} of $\approx$0.18 V and a short-circuit current of $\approx$1.1 μA under 80% environmental relative humidity (RH) variation (from 15% to 95%). To evaluate the unit's performance under bending, the V_{oc} was monitored at different angles of bending in the directions parallel and perpendicular to the interdigital electrodes, as shown in Fig. 17h – panel i. The generated V_{oc} fluctuates within $\pm$0.02 V when the generator is folded between inward and outward states. As shown in Fig. 17h – panel ii, the generated voltage increases in proportion to the number of generators in series and the current also raises with increased number of parallel units. Eight units have a high V_{oc} of 1.21 V in series and I_{sc} of 3.97 μA in parallel connection, respectively. Impressively, flexible films with 32 serial units can be rolled up inside a tube (Fig. 17h – panel iii), easily powering a commercial LED bulb when a man exhales moisture through this small tube (Fig. 17h – panel iv).

6. Summary and perspectives

Vision of future green and energy sustainable cities

A vast number of experiments have been discussed in this review revealing the tremendous potential of 2D materials for emerging energy conversion technologies spanning different demonstrators' scales: from miniature harvesters to large-scale renewable energy installations. The introductory Fig. 1 schematically summarizes the output of recent literature reports on GRM incorporation in a vast number of emerging energy conversion systems. It becomes apparent based on these studies, therefore, the high potential of GRM towards energy harvesters with enhanced efficiency and significantly reduced manufacturing cost, at a very low environmental impact. For the cities of the future, one portion of the required energy can be provided by large-scale GRM-enabled solar panels installed in solar farms and rooftops. The recent realization of a Solar farm in HMU campus accommodating multiple PV panels incorporating GRMs, is paving the way for future developments. Furthermore, high-performing GRM-enabled FCs for the hydrogen or methanol economy of the future will lead to large installations associated with H_2 mobility and stationary power. The GRM miniature harvesters have the potential to provide the required power for IoT sensors integrated in smart houses (building-integrated PV). Besides, a wide variety of wearables can be operated by GRM-enabled, flexible TEG, PENG and TENG. Notably, a significant amount of energy can be harvested through the whole water cycle, contributing in on-grid electricity generation. In particular, this holistic approach includes GRM-based electricity generation through (a) natural evaporation, (b) moisture-generated electricity, (c) drawing, streaming or splashing potential on functionalized surfaces covered by GRMs (even PV panels surfaces), (d) dedicated salinity gradient plants built at the boundary between ocean/river, as well (f) waving potential taking in advantage any floating object covered by GRM.[49]

We list below some critical directions that the research related to GRM-enabled energy harvesters should be focused towards enabling energy sustainable green cities. It becomes apparent that compact, GRM-based flexible miniature harvesters apart from providing power for IoT devices, when integrated in large networks could also contribute in on-grid electricity generation. GRM integrated in upscaled energy conversion installations provide new approaches for hybrid, multi-energy harvesting allowing for an all-weather operation while maintaining constant output power under various conditions. Up-scalability for large-scale energy production can be materialized by the in-series connection of multiple harvesters.

GRM as emerging flexible energy harvesters for industry 4.0

The novel technology of smart electronics consisting of distinct subunits can create self-powered sensors, actuators, and integrated systems targeting applications from wearables, to implantable or even edible electronic. Adding to the flexibility and the ultra-thin thickness, GRM possess extraordinary emerging properties going far beyond the conventional bulk materials paradigm (Fig. 7–9). New ways of highly performing miniature energy harvesters are now available that is expected to give a boost in various technology fields including autonomous IoT sensors, electronics, healthcare, building-integrated PV and transportation (Fig. 10–13). Moreover, artificial GRM heterostructures are characterized by multiferroicity or multifunctionality that enables the realization of ultracompact multi-harvesters in a single material stack. Many smart energy harvesters based on GRM technology have been already demonstrated (Fig. 1), however some remaining bottlenecks of this technology should be addressed. Large-scale 2D-based films production with extended stability and strict control over uniformity, functionalization, hydrophobic properties, and porosity properties are utmost need. The spectacular progress in flexible electronics has opened a new era, and in synergy with IoT and Artificial Intelligence technology are expected to be one of the Industry 4.0 main pillars.

Hybrid, complementary, multi-harvesters for all-weather operation

In this review, numerous energy conversion techniques enabled by GRM were described, suitable to harvest the available ambient energy from our living environment. However, it became apparent that a single type of energy harvester is almost impossible to operate at maximum efficiency under variable atmospheric conditions. A problem to this issue could be the development of hybrid approaches by combining more than one conversion technology into a single device offering complementarity. This approach is expected to deliver higher and steady performance at variable external conditions by storing the harvested energy in battery or supercapacitor that can provide in a continuous way, when is charged, the required

output voltages for the various electrical appliances' operation.[12] As an example, solar panels require maximum solar irradiation, however the opposite is true for raindrop-induced electricity generation. RF generators operate at high frequency spectrum, while TENG or water-based energy harvesters are efficient in harvesting low frequency energy.

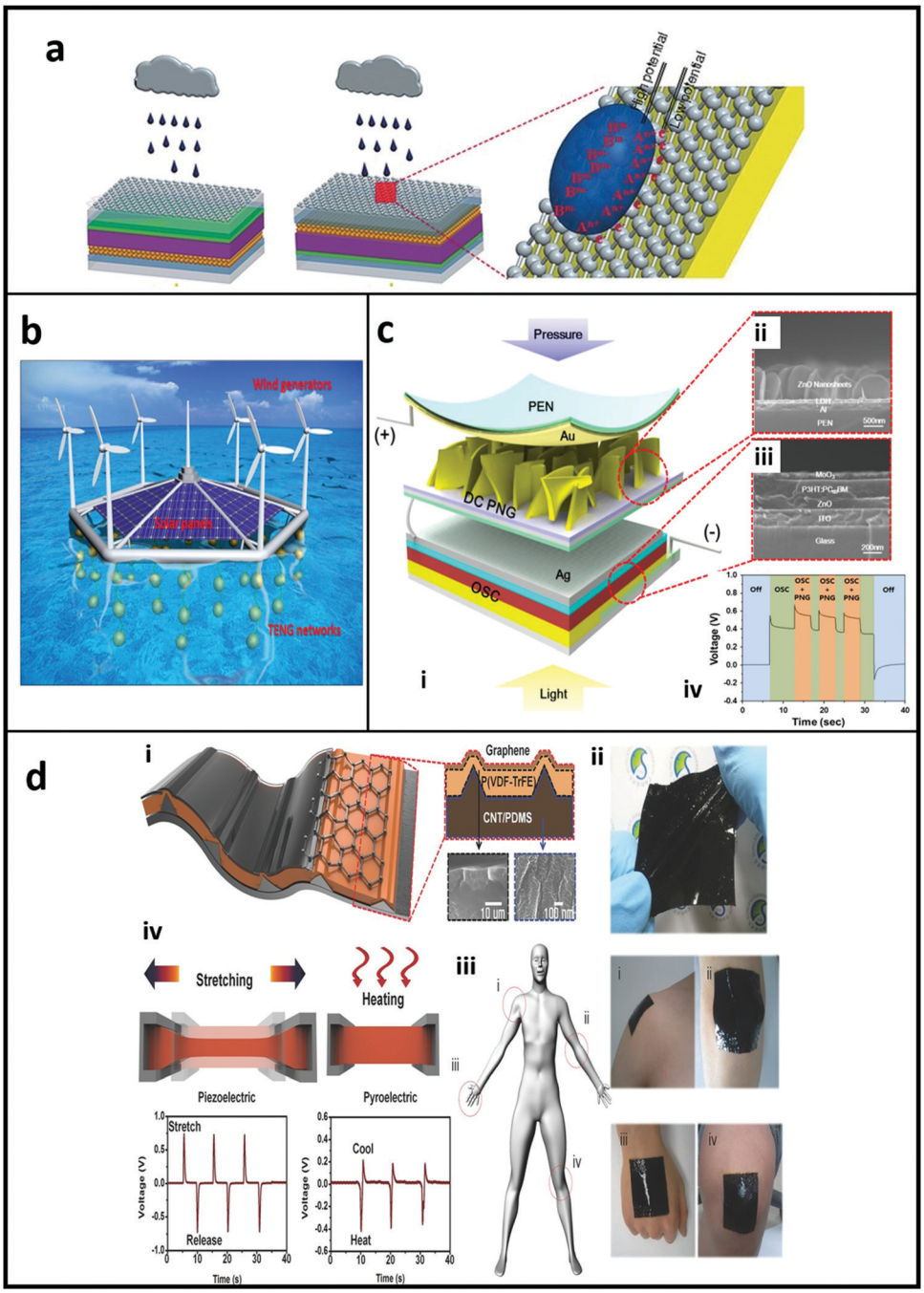

Fig. 18 Hybrid harvesters towards on-grid energy generation. (a) A flexible hybrid solar cell triggered also by raindrops energy. (Reproduced with permission.[61] Copyright 2016 WILEY-VCH Verlag GmbH & Co. KGaA, Weinheim). (b) A floating multi-energy harvesting system including PV, wind generators and multiple water based TENG. (Reproduced with permission.[8] Copyright 2017 Elsevier). (c) Design of a hybrid device for simultaneous harvesting of mechanical and solar energies under external mechanical force and light illumination. (i) 3D schematic representation of the device. (ii) Cross-sectional FE-SEM image of ZnO nanosheets grown on an Al film. (ii) Cross-sectional FE-SEM image of the inverted OPV structure. (iv) V output of the device when the pressure is applied periodically at an interval of 3.0 s for an extended period of 1.0 s. (Reproduced with permission.[348] Copyright 2015 Elsevier.) (d) (i) Schematic illustration of the device, (ii) photo image of the nanogenerator, (iii) photo images of the hybrid harvester at various locations on human body, showing good compatibility of the device with various parts of body, and (iv) piezoelectric output voltage from the hybrid harvester under stretch-release condition, and pyroelectric output voltage under a thermal gradient (heat and cool). (Reproduced with permission.[62] Copyright 2014 WILEY-VCH Verlag GmbH & Co. KGaA, Weinheim.)

A seminal work was reported by Tang *et al.* demonstrating a flexible solar cell triggered by combining an rGO electrode with a dye-sensitized solar cell (Fig. 18a). This hybrid new solar cell can be excited by incident light on sunny days and raindrops on rainy days, yielding an optimal PCE of 6.53% and current over microamps as well as a voltage of hundreds of microvolts by simulated raindrops.[61] More recently, a similar concept was demonstrated on a hybrid power generator based on silicon PVs modified by water-based energy harvester enabled by graphene TENG.[55] Furthermore, recent studies have revealed that the energy flux from the ambient environment to water vapour can be engineered to a higher level through a synergy between plasmon assisted solar energy absorption and capillary enabled rapid water diffusion.[49] Hybrid approaches such as integrating GRM-enabled superhydrophobic TENG films with self-cleaning ability on solar parks could not only boost the PV output but also enable the long-term performance of the installation. Another unconventional approach could be the combination of TEG in synergy with PV, where they could be used to take advantage of the infrared part of the solar spectra that is not absorbed by the photoactive material, as well reduce the temperature of PV cell during operation.

Floating integrated systems could be the path for realizing the blue energy dream that can provide additional power for on-grid generation while maximizing the space utilization efficiency. Fig. 18b shows a schematic illustration of a multi-energy harvesting system consisting of a three-dimensional network of TENG for water energy harnessing, wind generators and solar panels.[8] Coupling between mechanical properties and other physical properties further paves the way to novel structure with unique optoelectronic properties such as emerging piezo-phototronic effects, as well to tailor GRM-enabled energy harvesters with ideal mechanical properties. Examples include MoS_2/WSe_2[56] and p-MoS_2/n-ZnO[57] heterostructure photodiodes, and MoS_2 strain-gated adaptive photodetectors.[58] The schematic design of a hybrid power generator made a direct-current PENG based on ZnO nanosheets and an OPV is shown in the panel i of Fig. 18c.[348] A cross-sectional FE-SEM image of ZnO nanosheets grown on Ag substrate and OPV device are presented in panel ii and panel iii, respectively, whereas in panel iv the schematic design of the equivalent electrical circuit of the hybrid device is presented. The output power of the total device is higher than the corresponding performance of separate units, as shown in Fig. 18c – panel iv.

The coupling of piezoelectric and pyroelectric properties was also demonstrated in a hybrid device capable of harvesting both thermal and mechanical energy.[62] A highly stretchable nanogenerator was fabricated based on the micro-patterned piezoelectric P(VDF-TrFE) polymer, a micro-patterned PDMS-carbon nanotubes composite and graphene nanosheets. The device schematic is shown Fig. 18d – panel i, whereas an optical photo is depicted in panel ii. The hybrid nanogenerator was placed at different locations of the human body exhibiting high compatibility and adaptability. The performance of the device under various mechanical and thermal stimuli is shown in panel iv, revealing the high promise of this approach in stretchable, flexible electronics. New functionalities can arise under simultaneous solar (*i.e.* by shining light on MoS_2 sheets) and heat excitations further boosting energy conversion.[60]

Up-scalability materialized by in-series connection of multiple harvesters

The in-series or parallel connection of few miniature harvesters provides enough electric power to support the autonomous operation of commercial electric products (Fig. 13 and 17). Among the various types of nanogenerators, TENG have the potential for high voltage and power density generation. Their integration in large-scale blue energy conversion concepts has been shown as a very promising approach, although efficient system integration with the power management module and durability issues have to be resolved. This constitutes a steady pace progress that predisposes for GRM-based harvesters decisive role expected in future's renewable energy technologies. However, the establishment of a much wider network of interconnected miniature or up-scaled harvesters could also contribute in on-grid electricity generation. Notably, the recent tremendous progress reported in large scale GRM enabled PV and FC (Fig. 15 and 16) opens the path towards on-grid energy product realization in the near future, upon upscaling panels/modules production throughput.

Many high technology readiness level devices enabled by GRM have been recently demonstrated.[349] Notable examples include IoT sensors for healthcare, miniature energy harvesters integrated on clothes, high data throughput transmitters for 5G era, as well as the worldwide first Solar farm enabled by GRM-based PV panels.** Consequently, many market's products are expected in the middle term ($\sim$5 y) related to energy sector (batteries for e-vehicles, PV, *etc.*), flexible electronics, telecommunications and AI-assisted IoT sensors for automated driving.

List of definitions & abbreviations

2D	Two-dimensional
BP	Black phosphorous
CVD	Chemical vapor deposition
FC	Fuel cells
GO	Graphene oxide
GRM	Graphene and other related 2D materials
h-BN	Hexagonal boron nitride
IoT	Internet of things
LCD	Liquid crystal display
MEA	Membrane electrode assembly
MEG	Moist-electric generation
MoS_2	Molybdenum disulfide
MXenes	Transition metal carbides/carbonitrides
OPV	Organic photovoltaics
PCE	Power conversion efficiency
PEMFC	Polymer electrolyte membrane fuel cells
PDMS	Polydimethylsiloxane

** https://graphene.azurewebsites.net/Graphene-Flagship-Annual-Report-2020/#page=18.

PENG	Piezoelectric nano generator
PePV	Perovskite photovoltaics
PET	Polyethylene terephthalate
PL	Photoluminescence
PI	Polyimide
PV	Photovoltaic
R2R	Roll to roll
rGO	Reduced graphene oxide
SC	Solar cells
SGM	Structured graphene metamaterial
WS_2	Tungsten disulfide
TE	Thermoelectric
TEG	Thermoelectric generators
TENG	Triboelectric nano generator
TMDC	Transition metal dichalcogenides

Conflicts of interest

There are no conflicts to declare.

References

1 F. Yi, H. Ren, J. Shan, X. Sun, D. Wei and Z. Liu, *Chem. Soc. Rev.*, 2018, **47**, 3152–3188.
2 K. Kim, B. Kim and C. H. Lee, *Adv. Mater.*, 2020, **32**, 1902051.
3 Y. Khan, A. Thielens, S. Muin, J. Ting, C. Baumbauer and A. C. Arias, *Adv. Mater.*, 2020, **32**, 1905279.
4 S. Seo, J. Park, J. Park, K. Song, S. Cha, S. Sim, S. Choi, H. W. Yeom, H. Choi and M. Jo, *Nat. Electron.*, 2018, **1**, 512–517.
5 H. Yuan, T. Lei, Y. Qin and R. Yang, *Nano Energy*, 2019, **59**, 84–90.
6 H. Xue, Q. Yang, D. Wang, W. Luo, W. Wang, M. Lin, D. Liang and Q. Luo, *Nano Energy*, 2017, **38**, 147–154.
7 A. Ahmed, I. Hassan, M. F. El-Kady, A. Radhi, C. K. Jeong, P. R. Selvaganapathy, J. Zu, S. Ren, Q. Wang and R. B. Kaner, *Adv. Sci.*, 2019, **6**, 1802230.
8 Z. L. Wang, T. Jiang and L. Xu, *Nano Energy*, 2017, **39**, 9–23.
9 N. M. Haegel, H. Atwater, T. Barnes, C. Breyer, A. Burrell, Y.-M. Chiang, S. De Wolf, B. Dimmler, D. Feldman, S. Glunz, J. C. Goldschmidt, D. Hochschild, R. Inzunza, I. Kaizuka, B. Kroposki, S. Kurtz, S. Leu, R. Margolis, K. Matsubara, A. Metz, W. K. Metzger, M. Morjaria, S. Niki, S. Nowak, I. M. Peters, S. Philipps, T. Reindl, A. Richter, D. Rose, K. Sakurai, R. Schlatmann, M. Shikano, W. Sinke, R. Sinton, B. J. Stanbery, M. Topic, W. Tumas, Y. Ueda, J. van de Lagemaat, P. Verlinden, M. Vetter, E. Warren, M. Werner, M. Yamaguchi and A. W. Bett, *Science*, 2019, **364**, 836–838.
10 M. A. Green and S. P. Bremner, *Nat. Mater.*, 2016, **16**, 23–34.
11 A. Siria, M.-L. Bocquet and L. Bocquet, *Nat. Rev. Chem.*, 2017, **1**, 0091.
12 H. Ryu, H. Yoon and S. Kim, *Adv. Mater.*, 2019, **31**, 1802898.
13 X. Zhang, J. Grajal, J. L. Vazquez-Roy, U. Radhakrishna, X. Wang, W. Chern, L. Zhou, Y. Lin, P.-C. Shen, X. Ji, X. Ling, A. Zubair, Y. Zhang, H. Wang, M. Dubey, J. Kong, M. Dresselhaus and T. Palacios, *Nature*, 2019, **566**, 368–372.
14 Y. Wang, N. Xu, D. Li and J. Zhu, *Adv. Funct. Mater.*, 2017, **27**, 1604134.
15 J. Bai, Y. Huang, H. Cheng and L. Qu, *Nanoscale*, 2019, **11**, 23083–23091.
16 X. Zhang, Z. Bu, S. Lin, Z. Chen, W. Li and Y. Pei, *Joule*, 2020, **4**, 986–1003.
17 A. Yu, Y. Zhu, W. Wang and J. Zhai, *Adv. Funct. Mater.*, 2019, **29**, 1900098.
18 L. Wang, L. Huang, W. C. Tan, X. Feng, L. Chen, X. Huang and K.-W. Ang, *Small Methods*, 2018, **2**, 1700294.
19 J. Zhu, Z. Hu, C. Song, N. Yi, Z. Yu, Z. Liu, S. Liu, M. Wang, M. G. Dexheimer, J. Yang and H. Cheng, *Mater. Today Phys.*, 2021, **18**, 100377.
20 Y. Liang, F. Zhao, Z. Cheng, Y. Deng, Y. Xiao, H. Cheng, P. Zhang, Y. Huang, H. Shao and L. Qu, *Energy Environ. Sci.*, 2018, **11**, 1730–1735.
21 C. Yang, Y. Huang, H. Cheng, L. Jiang and L. Qu, *Adv. Mater.*, 2019, **31**, 1805705.
22 L. Yin, F. Wang, R. Cheng, Z. Wang, J. Chu, Y. Wen and J. He, *Adv. Funct. Mater.*, 2019, **29**, 1804897.
23 Y. Tokura, M. Kawasaki and N. Nagaosa, *Nat. Phys.*, 2017, **13**, 1056–1068.
24 P. Rivera, K. L. Seyler, H. Yu, J. R. Schaibley, J. Yan, D. G. Mandrus, W. Yao and X. Xu, *Science*, 2016, **351**, 688–691.
25 P. Rivera, J. R. Schaibley, A. M. Jones, J. S. Ross, S. Wu, G. Aivazian, P. Klement, K. Seyler, G. Clark, N. J. Ghimire, J. Yan, D. G. Mandrus, W. Yao and X. Xu, *Nat. Commun.*, 2015, **6**, 6242.
26 M. Dai, Z. Wang, F. Wang, Y. Qiu, J. Zhang, C.-Y. Xu, T. Zhai, W. Cao, Y. Fu, D. Jia, Y. Zhou and P.-A. Hu, *Nano Lett.*, 2019, **19**, 5410–5416.
27 Y. Liu, J. Guo, E. Zhu, L. Liao, S. J. Lee, M. Ding, I. Shakir, V. Gambin, Y. Huang and X. Duan, *Nature*, 2018, **557**, 696–700.
28 C. Zhang, Y. Nie, S. Sanvito and A. Du, *Nano Lett.*, 2019, **19**, 1366–1370.
29 X. Chen, Z. Zhou, B. Deng, Z. Wu, F. Xia, Y. Cao, L. Zhang, W. Huang, N. Wang and L. Wang, *Nano Today*, 2019, **27**, 99–119.
30 X. Wang, A. Cui, F. Chen, L. Xu, Z. Hu, K. Jiang, L. Shang and J. Chu, *Small*, 2019, **15**, 1903106.
31 H. Zhan, D. Guo and G. Xie, *Nanoscale*, 2019, **11**, 13181–13212.
32 C. Wang, Q. He, U. Halim, Y. Liu, E. Zhu, Z. Lin, H. Xiao, X. Duan, Z. Feng, R. Cheng, N. O. Weiss, G. Ye, Y.-C. Huang, H. Wu, H.-C. Cheng, I. Shakir, L. Liao, X. Chen, W. A. Goddard III, Y. Huang and X. Duan, *Nature*, 2018, **555**, 231–236.
33 D. K. Polyushkin, S. Wachter, L. Mennel, M. Paur, M. Paliy, G. Iannaccone, G. Fiori, D. Neumaier, B. Canto and T. Mueller, *Nat. Electron.*, 2020, **3**, 486–491.

34 M. Ye, Z. Zhang, Y. Zhao and L. Qu, *Joule*, 2018, **2**, 245–268.
35 S. Yun, Y. Zhang, Q. Xu, J. Liu and Y. Qin, *Nano Energy*, 2019, **60**, 600–619.
36 P. Zhang, F. Wang, M. Yu, X. Zhuang and X. Feng, *Chem. Soc. Rev.*, 2018, **47**, 7426–7451.
37 X. Chen, K. Shehzad, L. Gao, M. Long, H. Guo, S. Qin, X. Wang, F. Wang, Y. Shi, W. Hu, Y. Xu and X. Wang, *Adv. Mater.*, 2019, 1902039.
38 A. S. R. Bati, M. Batmunkh and J. G. Shapter, *Adv. Energy Mater.*, 2020, **10**, 1902253.
39 A. Di Carlo, A. Agresti, F. Brunetti and S. Pescetelli, *J. Phys. Energy*, 2020, **2**, 031003.
40 B. Wang, J. Iocozzia, M. Zhang, M. Ye, S. Yan, H. Jin, S. Wang, Z. Zou and Z. Lin, *Chem. Soc. Rev.*, 2019, **48**, 4854–4891.
41 Y. Lin, B. Adilbekova, Y. Firdaus, E. Yengel, H. Faber, M. Sajjad, X. Zheng, E. Yarali, A. Seitkhan, O. M. Bakr, A. El-Labban, U. Schwingenschlögl, V. Tung, I. McCulloch, F. Laquai and T. D. Anthopoulos, *Adv. Mater.*, 2019, **31**, 1902965.
42 S. Das, D. Pandey, J. Thomas and T. Roy, *Adv. Mater.*, 2019, **31**, 1802722.
43 P. Mariani, A. Agresti, L. Vesce, S. Pescetelli, A. L. Palma, F. Tomarchio, P. Karagiannidis, A. C. Ferrari and A. Di Carlo, *ACS Appl. Energy Mater.*, 2021, **4**, 98–110.
44 A. Agresti, S. Pescetelli, A. L. Palma, B. Martín-García, L. Najafi, S. Bellani, I. Moreels, M. Prato, F. Bonaccorso and A. Di Carlo, *ACS Energy Lett.*, 2019, **4**, 1862–1871.
45 E. Lamanna, F. Matteocci, E. Calabrò, L. Serenelli, E. Salza, L. Martini, F. Menchini, M. Izzi, A. Agresti, S. Pescetelli, S. Bellani, A. E. Del Río Castillo, F. Bonaccorso, M. Tucci and A. Di Carlo, *Joule*, 2020, **4**, 865–881.
46 C. Li, Q. Cao, F. Wang, Y. Xiao, Y. Li, J.-J. Delaunay and H. Zhu, *Chem. Soc. Rev.*, 2018, **47**, 4981–5037.
47 T. A. Shifa, F. Wang, Y. Liu and J. He, *Adv. Mater.*, 2019, **31**, 1804828.
48 D. Deng, K. S. Novoselov, Q. Fu, N. Zheng, Z. Tian and X. Bao, *Nat. Nanotechnol.*, 2016, **11**, 218–230.
49 Z. Zhang, X. Li, J. Yin, Y. Xu, W. Fei, M. Xue, Q. Wang, J. Zhou and W. Guo, *Nat. Nanotechnol.*, 2018, **13**, 1109–1119.
50 D. Pakulski, W. Czepa, S. D. Buffa, A. Ciesielski and P. Samorì, *Adv. Funct. Mater.*, 2020, **30**, 1902394.
51 M. Z. Iqbal, A.-U. Rehman and S. Siddique, *J. Energy Chem.*, 2019, **39**, 217–234.
52 D. B. Shinde, I. V. Vlassiouk, M. R. Talipov and S. N. Smirnov, *ACS Nano*, 2019, **13**, 13136–13143.
53 M. Lozada-Hidalgo, S. Zhang, S. Hu, A. Esfandiar, I. V. Grigorieva and A. K. Geim, *Nat. Commun.*, 2017, **8**, 15215.
54 S. Lee, W. Jang, M. Kim, J. E. Shin, H. B. Park, N. Jung and D. Whang, *Small*, 2019, **15**, 1903705.
55 D. Yoo, S.-C. Park, S. Lee, J.-Y. Sim, I. Song, D. Choi, H. Lim and D. S. Kim, *Nano Energy*, 2019, **57**, 424–431.
56 P. Lin, L. Zhu, D. Li, L. Xu, C. Pan and Z. Wang, *Adv. Funct. Mater.*, 2018, **28**, 1802849.
57 F. Xue, L. Chen, J. Chen, J. Liu, L. Wang, M. Chen, Y. Pang, X. Yang, G. Gao, J. Zhai and Z. L. Wang, *Adv. Mater.*, 2016, **28**, 3391–3398.
58 W. Wu, L. Wang, R. Yu, Y. Liu, S.-H. Wei, J. Hone and Z. L. Wang, *Adv. Mater.*, 2016, **28**, 8463–8468.
59 S. Liu, S. Lin, P. You, C. Surya, S. P. Lau and F. Yan, *Angew. Chem., Int. Ed. Engl.*, 2017, **56**, 13717–13721.
60 K. Xiao, L. Jiang and M. Antonietti, *Joule*, 2019, **3**, 2364–2380.
61 Q. Tang, X. Wang, P. Yang and B. He, *Angew. Chem., Int. Ed.*, 2016, **55**, 5243–5246.
62 J.-H. Lee, K. Y. Lee, M. K. Gupta, T. Y. Kim, D.-Y. Lee, J. Oh, C. Ryu, W. J. Yoo, C.-Y. Kang, S.-J. Yoon, J.-B. Yoo and S.-W. Kim, *Adv. Mater.*, 2014, **26**, 765–769.
63 B. Deng, Z. Liu and H. Peng, *Adv. Mater.*, 2019, **31**, 1800996.
64 B. N. Chandrashekar, B. Deng, A. S. Smitha, Y. Chen, C. Tan, H. Zhang, H. Peng and Z. Liu, *Adv. Mater.*, 2015, **27**, 5210–5216.
65 S. Kim, Y. C. Kim, Y. J. Choi, H. J. Woo, Y. J. Song, M. S. Kang, C. Lee and J. H. Cho, *ACS Appl. Mater. Interfaces*, 2019, **11**, 35444–35450.
66 A. Quellmalz, X. Wang, S. Sawallich, B. Uzlu, M. Otto, S. Wagner, Z. Wang, M. Prechtl, O. Hartwig, S. Luo, G. S. Duesberg, M. C. Lemme, K. B. Gylfason, N. Roxhed, G. Stemme and F. Niklaus, *Nat. Commun.*, 2021, **12**, 917.
67 G. Hu, J. Kang, L. W. T. Ng, X. Zhu, R. C. T. Howe, C. G. Jones, M. C. Hersam and T. Hasan, *Chem. Soc. Rev.*, 2018, **47**, 3265–3300.
68 A. E. Del Rio Castillo, V. Pellegrini, A. Ansaldo, F. Ricciardella, H. Sun, L. Marasco, J. Buha, Z. Dang, L. Gagliani, E. Lago, N. Curreli, S. Gentiluomo, F. Palazon, M. Prato, R. Oropesa-Nuñez, P. S. Toth, E. Mantero, M. Crugliano, A. Gamucci, A. Tomadin, M. Polini and F. Bonaccorso, *Mater. Horiz.*, 2018, **5**, 890–904.
69 C. E. Shuck, A. Sarycheva, M. Anayee, A. Levitt, Y. Zhu, S. Uzun, V. Balitskiy, V. Zahorodna, O. Gogotsi and Y. Gogotsi, *Adv. Eng. Mater.*, 2020, **22**, 1901241.
70 J. Lee, S. Kang, H. Jang, J. Moon and D. Whang, *Adv. Mater.*, 2019, **31**, 1803469.
71 B. Deng, Z. Xin, R. Xue, S. Zhang, X. Xu, J. Gao, J. Tang, Y. Qi, Y. Wang, Y. Zhao, L. Sun, H. Wang, K. Liu, M. H. Rummeli, L.-T. Weng, Z. Luo, L. Tong, X. Zhang, C. Xie, Z. Liu and H. Peng, *Sci. Bull.*, 2019, **64**, 659–668.
72 Y. Huang, H. Cheng, C. Yang, H. Yao, C. Li and L. Qu, *Energy Environ. Sci.*, 2019, **12**, 1848–1856.
73 H. Cheng, Y. Huang, F. Zhao, C. Yang, P. Zhang, L. Jiang, G. Shi and L. Qu, *Energy Environ. Sci.*, 2018, **11**, 2839–2845.
74 W. Ma, J. Lu, B. Wan, D. Peng, Q. Xu, G. Hu, Y. Peng, C. Pan and Z. L. Wang, *Adv. Mater.*, 2020, **32**, 1905795.
75 J. Wu, Y. Chen, J. Wu and K. Hippalgaonkar, *Adv. Electron. Mater.*, 2018, **4**, 1800248.
76 P. Zong, J. Liang, P. Zhang, C. Wan, Y. Wang and K. Koumoto, *ACS Appl. Energy Mater.*, 2020, **3**, 2224–2239.
77 T. Juntunen, H. Jussila, M. Ruoho, S. Liu, G. Hu, T. Albrow-Owen, L. W. T. Ng, R. C. T. Howe, T. Hasan, Z. Sun and I. Tittonen, *Adv. Funct. Mater.*, 2018, **28**, 1800480.

78 Y. Dong, S. S. K. Mallineni, K. Maleski, H. Behlow, V. N. Mochalin, A. M. Rao, Y. Gogotsi and R. Podila, *Nano Energy*, 2018, **44**, 103–110.
79 S. Lee, B. Yeom, Y. Kim and J. Cho, *Nano Energy*, 2019, **56**, 1–15.
80 M. Seol, S. Kim, Y. Cho, K.-E. Byun, H. Kim, J. Kim, S. K. Kim, S.-W. Kim, H.-J. Shin and S. Park, *Adv. Mater.*, 2018, **30**, 1801210.
81 C. Wu, T. W. Kim, J. H. Park, H. An, J. Shao, X. Chen and Z. L. Wang, *ACS Nano*, 2017, **11**, 8356–8363.
82 Z. Liu, Z. Zhao, X. Zeng, X. Fu and Y. Hu, *J. Phys. Appl. Phys.*, 2019, **52**, 314002.
83 J. Pei, J. Yang, T. Yildirim, H. Zhang and Y. Lu, *Adv. Mater.*, 2019, **31**, 1706945.
84 K. Rogdakis, Z. Viskadourakis, A. P. Petrović, E. Choi, J. Lee and C. Panagopoulos, *Appl. Phys. Lett.*, 2015, **106**, 3–8.
85 R. Thomale, *Nature*, 2020, **583**, 364–365.
86 Y. Shi, S. Xu, Y. Yang, S. Slizovskiy, S. V. Morozov, S.-K. Son, S. Ozdemir, C. Mullan, J. Barrier, J. Yin, A. I. Berdyugin, B. A. Piot, T. Taniguchi, K. Watanabe, V. I. Fal'ko, K. S. Novoselov, A. K. Geim and A. Mishchenko, *Nature*, 2020, **584**, 210–214.
87 M. Batmunkh, M. Bat-Erdene and J. G. Shapter, *Adv. Mater.*, 2016, **28**, 8586–8617.
88 I. V. Sankar, J. Jeon, S. K. Jang, J. H. Cho, E. Hwang and S. Lee, *Nano Brief Reports and Reviews*, 2019, **14**(12), DOI: 10.1142/S1793292019300093.
89 C. Jin, J. Kim, J. Suh, Z. Shi, B. Chen, X. Fan, M. Kam, K. Watanabe, T. Taniguchi, S. Tongay, A. Zettl, J. Wu and F. Wang, *Nat. Phys.*, 2017, **13**, 127–131.
90 Y. Chen, X. Wang, G. Wu, Z. Wang, H. Fang, T. Lin, S. Sun, H. Shen, W. Hu, J. Wang, J. Sun, X. Meng and J. Chu, *Small*, 2018, **14**, 1703293.
91 Y. He, A. Sobhani, S. Lei, Z. Zhang, Y. Gong, Z. Jin, W. Zhou, Y. Yang, Y. Zhang, X. Wang, B. Yakobson, R. Vajtai, N. J. Halas, B. Li, E. Xie and P. Ajayan, *Adv. Mater.*, 2016, **28**, 5126–5132.
92 Y. Ma, P. M. Ajayan, S. Yang and Y. Gong, *Small*, 2018, **14**, 1801606.
93 R. Frisenda, A. J. Molina-Mendoza, T. Mueller, A. Castellanos-Gomez and H. S. J. van der Zant, *Chem. Soc. Rev.*, 2018, **47**, 3339–3358.
94 M. Gobbi, E. Orgiu and P. Samorì, *Adv. Mater.*, 2018, **30**, 1706103.
95 Y. Xi, J. Zhuang, W. Hao and Y. Du, *ChemElectroChem*, 2019, **6**, 2841–2851.
96 X. Zhou, X. Hu, J. Yu, S. Liu, Z. Shu, Q. Zhang, H. Li, Y. Ma, H. Xu and T. Zhai, *Adv. Funct. Mater.*, 2018, **28**, 1706587.
97 Y. Liu, N. O. Weiss, X. Duan, H.-C. Cheng, Y. Huang and X. Duan, *Nat. Rev. Mater.*, 2016, **1**, 16042.
98 R. Cheng, F. Wang, L. Yin, Z. Wang, Y. Wen, T. A. Shifa and J. He, *Nat. Electron.*, 2018, **1**, 356–361.
99 Z. Zhang, P. Lin, Q. Liao, Z. Kang, H. Si and Y. Zhang, *Adv. Mater.*, 2019, **31**, 1806411.
100 L. Yang, P. Wang, J. Yin, C. Wang, G. Dong, Y. Wang and W. Ho, *Appl. Catal., B*, 2019, **250**, 42–51.
101 F. Zhao, H. Cheng, Z. Zhang, L. Jiang and L. Qu, *Adv. Mater.*, 2015, **27**, 4351–4357.
102 F. Zhao, Y. Liang, H. Cheng, L. Jiang and L. Qu, *Energy Environ. Sci.*, 2016, **9**, 912–916.
103 R. Sakamoto, N. Fukui, H. Maeda, R. Matsuoka, R. Toyoda and H. Nishihara, *Adv. Mater.*, 2019, **31**, 1804211.
104 S. Zhang, S. Guo, Z. Chen, Y. Wang, H. Gao, J. Gómez-Herrero, P. Ares, F. Zamora, Z. Zhu and H. Zeng, *Chem. Soc. Rev.*, 2018, **47**, 982–1021.
105 F. Wang, T. A. Shifa, P. Yu, P. He, Y. Liu, F. Wang, Z. Wang, X. Zhan, X. Lou, F. Xia and J. He, *Adv. Funct. Mater.*, 2018, **28**, 1802151.
106 Z. Hu, Z. Wu, C. Han, J. He, Z. Ni and W. Chen, *Chem. Soc. Rev.*, 2018, **47**, 3100–3128.
107 Y. L. Huang, Y. J. Zheng, Z. Song, D. Chi, A. T. S. Wee and S. Y. Quek, *Chem. Soc. Rev.*, 2018, **47**, 3241–3264.
108 M. Samadi, N. Sarikhani, M. Zirak, H. Zhang, H.-L. Zhang and A. Z. Moshfegh, *Nanoscale Horiz.*, 2018, **3**, 90–204.
109 W. Choi, N. Choudhary, G. H. Han, J. Park, D. Akinwande and Y. H. Lee, *Mater. Today*, 2017, **20**, 116–130.
110 K. F. Mak and J. Shan, *Nat. Photonics*, 2016, **10**, 216–226.
111 J. Pang, R. G. Mendes, A. Bachmatiuk, L. Zhao, H. Q. Ta, T. Gemming, H. Liu, Z. Liu and M. H. Rummeli, *Chem. Soc. Rev.*, 2019, **48**, 72–133.
112 M. Alhabeb, K. Maleski, B. Anasori, P. Lelyukh, L. Clark, S. Sin and Y. Gogotsi, *Chem. Mater.*, 2017, **29**, 7633–7644.
113 P. Simon and Y. Gogotsi, *Nat. Mater.*, 2020, **19**, 1151–1163.
114 Z. Guo, H. Zhang, S. Lu, Z. Wang, S. Tang, J. Shao, Z. Sun, H. Xie, H. Wang, X.-F. Yu and P. K. Chu, *Adv. Funct. Mater.*, 2015, **25**, 6996–7002.
115 C. Tan, X. Cao, X.-J. Wu, Q. He, J. Yang, X. Zhang, J. Chen, W. Zhao, S. Han, G.-H. Nam, M. Sindoro and H. Zhang, *Chem. Rev.*, 2017, **117**, 6225–6331.
116 J. W. Chen, S. T. Lo, S. C. Ho, S. S. Wong, T. H. Y. Vu, X. Q. Zhang, Y. De Liu, Y. Y. Chiou, Y. X. Chen, J. C. Yang, Y. C. Chen, Y. H. Chu, Y. H. Lee, C. J. Chung, T. M. Chen, C. H. Chen and C. L. Wu, *Nat. Commun.*, 2018, **9**, 3143.
117 F. Schwierz, J. Pezoldt and R. Granzner, *Nanoscale*, 2015, **7**, 8261–8283.
118 H. Li, X. Li, J. H. Park, L. Tao, K. K. Kim, Y. H. Lee and J. Bin Xu, *Nano Energy*, 2019, **57**, 214–221.
119 Y. Han, M. Y. Li, G. S. Jung, M. A. Marsalis, Z. Qin, M. J. Buehler, L. J. Li and D. A. Muller, *Nat. Mater.*, 2018, **17**, 129–133.
120 H. Zhang, J. Xiong, M. Ye, J. Li, X. Zhang, R. Quhe, Z. Song, J. Yang, Q. Zhang, B. Shi, J. Yan, W. Guo, J. Robertson, Y. Wang, F. Pan and J. Lu, *Phys. Rev. Appl*, 2019, **10**, 1.
121 L. Yin, F. Wang, R. Cheng, Z. Wang, J. Chu, Y. Wen and J. He, *Adv. Funct. Mater.*, 2019, **29**, 1804897.
122 A. G. Ricciardulli and P. W. M. Blom, *Adv. Mater. Technol.*, 2020, **5**, 1900972.
123 D. Sarkar, X. Xie, W. Liu, W. Cao, J. Kang, Y. Gong, S. Kraemer, P. M. Ajayan and K. Banerjee, *Nature*, 2015, **526**, 91–95.
124 W. Liao, Y. Huang, H. Wang and H. Zhang, *Appl. Mater. Today*, 2019, **16**, 435–455.

125 M. Bernardi, M. Palummo and J. C. Grossman, *Nano Lett.*, 2013, **13**, 3664–3670.
126 S. Kim, M. K. Gupta, K. Y. Lee, A. Sohn, T. Y. Kim, K.-S. Shin, D. Kim, S. K. Kim, K. H. Lee, H.-J. Shin, D.-W. Kim and S.-W. Kim, *Adv. Mater.*, 2014, **26**, 3918–3925.
127 D. X. Luong, K. V. Bets, W. A. Algozeeb, M. G. Stanford, C. Kittrell, W. Chen, R. V. Salvatierra, M. Ren, E. A. McHugh, P. A. Advincula, Z. Wang, M. Bhatt, H. Guo, V. Mancevski, R. Shahsavari, B. I. Yakobson and J. M. Tour, *Nature*, 2020, **577**, 647–651.
128 N. Briggs, S. Subramanian, Z. Lin, X. Li, X. Zhang, K. Zhang, K. Xiao, D. Geohegan, R. Wallace, L.-Q. Chen, M. Terrones, A. Ebrahimi, S. Das, J. Redwing, C. Hinkle, K. Momeni, A. van Duin, V. Crespi, S. Kar and J. A. Robinson, *2D Mater.*, 2019, **6**, 022001.
129 P. Chen, N. Li, X. Chen, W.-J. Ong and X. Zhao, *2D Mater.*, 2017, **5**, 014002.
130 A. H. Woomer, T. W. Farnsworth, J. Hu, R. A. Wells, C. L. Donley and S. C. Warren, *ACS Nano*, 2015, **9**, 8869–8884.
131 Z. Lin, A. McCreary, N. Briggs, S. Subramanian, K. Zhang, Y. Sun, X. Li, N. J. Borys, H. Yuan, S. K. Fullerton-Shirey, A. Chernikov, H. Zhao, S. McDonnell, A. M. Lindenberg, K. Xiao, B. J. LeRoy, M. Drndić, J. C. M. Hwang, J. Park, M. Chhowalla, R. E. Schaak, A. Javey, M. C. Hersam, J. Robinson and M. Terrones, *2D Mater.*, 2016, **3**, 042001.
132 J. Yu, X. Hu, H. Li, X. Zhou and T. Zhai, *J. Mater. Chem. C*, 2018, **6**, 4627–4640.
133 G. M. A. Angel, N. Mansor, R. Jervis, Z. Rana, C. Gibbs, A. Seel, A. F. R. Kilpatrick, P. R. Shearing, C. A. Howard, D. J. L. Brett and P. L. Cullen, *Nanoscale*, 2020, **12**, 16113–16122.
134 J. Liu and L. Fu, *Adv. Mater.*, 2018, 1800690.
135 D. P. Tabor, L. M. Roch, S. K. Saikin, C. Kreisbeck, D. Sheberla, J. H. Montoya, S. Dwaraknath, M. Aykol, C. Ortiz, H. Tribukait, C. Amador-Bedolla, C. J. Brabec, B. Maruyama, K. A. Persson and A. Aspuru-Guzik, *Nat. Rev. Mater.*, 2018, **3**, 5–20.
136 A. Rajagopal, K. Yao and A. K.-Y. Jen, *Adv. Mater.*, 2018, **30**, 1800455.
137 A. Kovtun, E. Treossi, N. Mirotta, A. Scidà, A. Liscio, M. Christian, F. Valorosi, A. Boschi, R. J. Young, C. Galiotis, I. A. Kinloch, V. Morandi and V. Palermo, *2D Mater.*, 2019, **6**, 025006.
138 J. Shim, H.-Y. Park, D.-H. Kang, J.-O. Kim, S.-H. Jo, Y. Park and J.-H. Park, *Adv. Electron. Mater.*, 2017, **3**, 1600364.
139 S. Yang, P. Zhang, A. S. Nia and X. Feng, *Adv. Mater.*, 2020, **32**, 1907857.
140 M. Zeng, Y. Xiao, J. Liu, K. Yang and L. Fu, *Chem. Rev.*, 2018, **118**, 6236–6296.
141 Y. Liu, Y. Huang and X. Duan, *Nature*, 2019, **567**, 323–333.
142 D. Akinwande, C. Huyghebaert, C.-H. Wang, M. I. Serna, S. Goossens, L.-J. Li, H.-S. P. Wong and F. H. L. Koppens, *Nature*, 2019, **573**, 507–518.
143 J. Wang, C. Teng, Y. Jiang, Y. Zhu and L. Jiang, *Adv. Mater.*, 2019, **31**, 1806742.
144 H. Liu, D. Li, C. Ma, X. Zhang, X. Sun, C. Zhu, B. Zheng, Z. Zou, Z. Luo, X. Zhu, X. Wang and A. Pan, *Nano Energy*, 2019, **59**, 66–74.
145 Y. Guo, P.-C. Shen, C. Su, A.-Y. Lu, M. Hempel, Y. Han, Q. Ji, Y. Lin, E. Shi, E. McVay, L. Dou, D. A. Muller, T. Palacios, J. Li, X. Ling and J. Kong, *Proc. Natl. Acad. Sci. U. S. A.*, 2019, **116**, 3437–3442.
146 J. Cheng, C. Wang, X. Zou and L. Liao, *Adv. Opt. Mater.*, 2019, **7**, 1800441.
147 Y. Wang, T. Wu, J. Barbaud, W. Kong, D. Cui, H. Chen, X. Yang and L. Han, *Science*, 2019, **365**, 687–691.
148 S. Das, D. Pandey, J. Thomas and T. Roy, *Adv. Mater.*, 2019, **31**, 1802722.
149 G. Hu, T. Albrow-Owen, X. Jin, A. Ali, Y. Hu, R. C. T. Howe, K. Shehzad, Z. Yang, X. Zhu, R. I. Woodward, T.-C. Wu, H. Jussila, J.-B. Wu, P. Peng, P.-H. Tan, Z. Sun, E. J. R. Kelleher, M. Zhang, Y. Xu and T. Hasan, *Nat. Commun.*, 2017, **8**, 278.
150 T. Carey, *Nat. Commun.*, 2017, **8**, 1202.
151 D. McManus, S. Vranic, F. Withers, V. Sanchez-Romaguera, M. Macucci, H. Yang, R. Sorrentino, K. Parvez, S.-K. Son, G. Iannaccone, K. Kostarelos, G. Fiori and C. Casiraghi, *Nat. Nanotechnol.*, 2017, **12**, 343–350.
152 L. Zhang, Q. Tan, H. Kou, D. Wu, W. Zhang and J. Xiong, *Sci. Rep.*, 2019, **9**, 9942.
153 L.-Q. Tao, K.-N. Zhang, H. Tian, Y. Liu, D.-Y. Wang, Y.-Q. Chen, Y. Yang and T.-L. Ren, *ACS Nano*, 2017, **11**, 8790–8795.
154 W. J. Hyun, E. B. Secor, C.-H. Kim, M. C. Hersam, L. F. Francis and C. D. Frisbie, *Adv. Energy Mater.*, 2017, **7**, 1700285.
155 M. S. Shawkat, H.-S. Chung, D. Dev, S. Das, T. Roy and Y. Jung, *ACS Appl. Mater. Interfaces*, 2019, **11**, 27251–27258.
156 M. A. Green, E. D. Dunlop, J. Hohl-Ebinger, M. Yoshita, N. Kopidakis and A. W. Y. Ho-Baillie, *Prog. Photovolt. Res. Appl.*, 2020, **28**, 3–15.
157 K. Yamamoto, K. Yoshikawa, H. Uzu and D. Adachi, *Jpn. J. Appl. Phys.*, 2018, **57**, 08RB20.
158 S. V. Morozov, K. S. Novoselov, M. I. Katsnelson, F. Schedin, D. C. Elias, J. A. Jaszczak and A. K. Geim, *Phys. Rev. Lett.*, 2008, **100**, 016602.
159 R. R. Nair, P. Blake, A. N. Grigorenko, K. S. Novoselov, T. J. Booth, T. Stauber, N. M. R. Peres and A. K. Geim, *Science*, 2008, **320**, 1308.
160 R. S. Sundaram, M. Engel, A. Lombardo, R. Krupke, A. C. Ferrari, P. Avouris and M. Steiner, *Nano Lett.*, 2013, **13**, 1416–1421.
161 B. Radisavljevic, A. Radenovic, J. Brivio, V. Giacometti and A. Kis, *Nat. Nanotechnol.*, 2011, **6**, 147–150.
162 H. Liu, A. T. Neal, Z. Zhu, Z. Luo, X. Xu, D. Tománek and P. D. Ye, *ACS Nano*, 2014, **8**, 4033–4041.
163 L. Li, Y. Yu, G. J. Ye, Q. Ge, X. Ou, H. Wu, D. Feng, X. H. Chen and Y. Zhang, *Nat. Nanotechnol.*, 2014, **9**, 372–377.
164 J. R. Brent, N. Savjani, E. A. Lewis, S. J. Haigh, D. J. Lewis and P. O'Brien, *Chem. Commun.*, 2014, **50**, 13338–13341.

165 F. Luo, D. Wang, J. Zhang, X. Li, D. Liu, H. Li, M. Lu, X. Xie, L. Huang and W. Huang, *ACS Appl. Nano Mater.*, 2019, **2**, 3793–3801.
166 Q. Zhang, S. Huang, J. Deng, D. T. Gangadharan, F. Yang, Z. Xu, G. Giorgi, M. Palummo, M. Chaker and D. Ma, *Adv. Funct. Mater.*, 2019, **29**, 1902486.
167 J. B. Smith, D. Hagaman and H.-F. Ji, *Nanotechnology*, 2016, **27**, 215602.
168 J. Dai and X. C. Zeng, *J. Phys. Chem. Lett.*, 2014, **5**, 1289–1293.
169 X. Chen, Y. Wu, Z. Wu, Y. Han, S. Xu, L. Wang, W. Ye, T. Han, Y. He, Y. Cai and N. Wang, *Nat. Commun.*, 2015, **6**, 7315.
170 Y. Deng, Z. Luo, N. J. Conrad, H. Liu, Y. Gong, S. Najmaei, P. M. Ajayan, J. Lou, X. Xu and P. D. Ye, *ACS Nano*, 2014, **8**, 8292–8299.
171 L. Bai, L. Sun, Y. Wang, Z. Liu, Q. Gao, H. Xiang, H. Xie and Y. Zhao, *J. Mater. Chem. A*, 2017, **5**, 8280–8286.
172 Y. Zhao, T. L. Chen, L. Xiao, M. A. Kolaczkowski, L. Zhang, L. M. Klivansky, V. Altoe, B. Tian, J. Guo, X. Peng, Y. Tian and Y. Liu, *Nano Energy*, 2018, **53**, 345–353.
173 S. Liu, S. Lin, P. You, C. Surya, S. P. Lau and F. Yan, *Angew. Chem., Int. Ed. Engl.*, 2017, **56**, 13717–13721.
174 Y. Yang, J. Gao, Z. Zhang, S. Xiao, H.-H. Xie, Z.-B. Sun, J.-H. Wang, C.-H. Zhou, Y.-W. Wang, X.-Y. Guo, P. K. Chu and X.-F. Yu, *Adv. Mater.*, 2016, **28**, 8937–8944.
175 M. Fontana, T. Deppe, A. K. Boyd, M. Rinzan, A. Y. Liu, M. Paranjape and P. Barbara, *Sci. Rep.*, 2013, **3**, 1–6.
176 M. Shanmugam, C. A. Durcan and B. Yu, *Nanoscale*, 2012, **4**, 7399–7405.
177 M. M. Furchi, A. Pospischil, F. Libisch, J. Burgdörfer and T. Mueller, *Nano Lett.*, 2014, **14**, 4785–4791.
178 C.-H. Lee, G.-H. Lee, A. M. van der Zande, W. Chen, Y. Li, M. Han, X. Cui, G. Arefe, C. Nuckolls, T. F. Heinz, J. Guo, J. Hone and P. Kim, *Nat. Nanotechnol.*, 2014, **9**, 676–681.
179 P. Jia, L. Wang, Y. Zhang, Y. Yang, X. Jin, M. Zhou, D. Quan, M. Jia and L. Cao, *Adv. Mater.*, 2021, 9.
180 T. Yang, X. Wang, B. Zheng, Z. Qi, C. Ma, Y. Fu, Y. Fu, M. P. Hautzinger, Y. Jiang, Z. Li, P. Fan, F. Li, W. Zheng, Z. Luo, J. Liu, B. Yang, S. Chen, D. Li, L. Zhang, S. Jin and A. Pan, *ACS Nano*, 2019, **13**, 7996–8003.
181 F. Zhang, H. Lu, J. Tong, J. J. Berry, M. C. Beard and K. Zhu, *Energy Environ. Sci.*, 2020, **13**, 1154–1186.
182 I. C. Smith, E. T. Hoke, D. Solis-Ibarra, M. D. McGehee and H. I. Karunadasa, *Angew. Chem., Int. Ed.*, 2014, **53**, 11232–11235.
183 J. Cho, J. T. DuBose, A. N. T. Le and P. V. Kamat, *ACS Mater. Lett.*, 2020, 565–570.
184 T. Luo, Y. Zhang, Z. Xu, T. Niu, J. Wen, J. Lu, S. Jin, S. (Frank) Liu and K. Zhao, *Adv. Mater.*, 2019, **31**, 1903848.
185 D. Kim, H. J. Jung, I. J. Park, B. W. Larson, S. P. Dunfield, C. Xiao, J. Kim, J. Tong, P. Boonmongkolras, S. G. Ji, F. Zhang, S. R. Pae, M. Kim, S. B. Kang, V. Dravid, J. J. Berry, J. Y. Kim, K. Zhu, D. H. Kim and B. Shin, *Science*, 2020, **368**, 155–160.
186 Z. Wang, Q. Lin, F. P. Chmiel, N. Sakai, L. M. Herz and H. J. Snaith, *Nat. Energy*, 2017, **2**, 1–10.
187 Y. Sun, Y. Yin, M. Pols, J. Zhong, Z. Huang, B. Liu, J. Liu, W. Wang, H. Xie, G. Zhan, Z. Zhou, W. Zhang, P. Wang, C. Zha, X. Jiang, Y. Ruan, C. Zhu, G. Brocks, X. Wang, L. Wang, J. Wang, S. Tao and W. Huang, *Adv. Mater.*, 2020, **32**, 2002392.
188 B. Jeong, H. Han and C. Park, *Adv. Mater.*, 2020, **32**, 2000597.
189 Z. Liu, L. You, N. Faraji, C. Lin, X. Xu, J. He, J. Seidel, J. Wang, H. N. Alshareef and T. Wu, *Adv. Funct. Mater.*, 2020, **30**, 1909672.
190 S. K. Behura, C. Wang, Y. Wen and V. Berry, *Nat. Photonics*, 2019, **13**, 312–318.
191 C. Xie, X. Zhang, Y. Wu, X. Zhang, X. Zhang, Y. Wang, W. Zhang, P. Gao, Y. Han and J. Jie, *J. Mater. Chem. A*, 2013, **1**, 8567–8574.
192 M. A. Rehman, S. B. Roy, D. Gwak, I. Akhtar, N. Nasir, S. Kumar, M. F. Khan, K. Heo, S.-H. Chun and Y. Seo, *Carbon*, 2020, **164**, 235–243.
193 M. N. Blonsky, H. L. Zhuang, A. K. Singh and R. G. Hennig, *ACS Nano*, 2015, **9**, 9885–9891.
194 K.-A. N. Duerloo, M. T. Ong and E. J. Reed, *J. Phys. Chem. Lett.*, 2012, **3**, 2871–2876.
195 M. M. Alyörük, Y. Aierken, D. Çakır, F. M. Peeters and C. Sevik, *J. Phys. Chem. C*, 2015, **119**, 23231–23237.
196 W. Wu, L. Wang, Y. Li, F. Zhang, L. Lin, S. Niu, D. Chenet, X. Zhang, Y. Hao, T. F. Heinz, J. Hone and Z. L. Wang, *Nature*, 2014, **514**, 470–474.
197 P. Ares, T. Cea, M. Holwill, Y. B. Wang, R. Roldán, F. Guinea, D. V. Andreeva, L. Fumagalli, K. S. Novoselov and C. R. Woods, *Adv. Mater.*, 2020, **32**, 1905504.
198 J.-H. Lee, J. Y. Park, E. B. Cho, T. Y. Kim, S. A. Han, T.-H. Kim, Y. Liu, S. K. Kim, C. J. Roh, H.-J. Yoon, H. Ryu, W. Seung, J. S. Lee, J. Lee and S.-W. Kim, *Adv. Mater.*, 2017, **29**, 1606667.
199 L. B. Drissi, S. Sadki and K. Sadki, *J. Phys. Chem. Solids*, 2018, **112**, 137–142.
200 M. Lanza, M. Reguant, G. Zou, P. Lv, H. Li, R. Chin, H. Liang, D. Yu, Y. Zhang, Z. Liu and H. Duan, *Adv. Mater. Interfaces*, 2014, **1**, 1300101.
201 Y. K. Fuh, C. C. Kuo, Z. M. Huang, S. C. Li and E. R. Liu, *Small*, 2016, **12**, 1875–1881.
202 J. K. Han, S. Kim, S. Jang, Y. R. Lim, S.-W. Kim, H. Chang, W. Song, S. S. Lee, J. Lim, K.-S. An and S. Myung, *Nano Energy*, 2019, **61**, 471–477.
203 H. Zhu, Y. Wang, J. Xiao, M. Liu, S. Xiong, Z. J. Wong, Z. Ye, Y. Ye, X. Yin and X. Zhang, *Nat. Nanotechnol.*, 2015, **10**, 151–155.
204 S. Manzeli, A. Allain, A. Ghadimi and A. Kis, *Nano Lett.*, 2015, **15**, 5330–5335.
205 H. J. Conley, B. Wang, J. I. Ziegler, R. F. Haglund, S. T. Pantelides and K. I. Bolotin, *Nano Lett.*, 2013, **13**, 3626–3630.
206 Q. Li, Q. Zhou, L. Shi, Q. Chen and J. Wang, *J. Mater. Chem. A*, 2019, **7**, 4291–4312.
207 G. Cheon, K.-A. N. Duerloo, A. D. Sendek, C. Porter, Y. Chen and E. J. Reed, *Nano Lett.*, 2017, **17**, 1915–1923.

208 J. Tan, Y. Wang, Z. Wang, X. He, Y. Liu, B. Wang, M. I. Katsnelson and S. Yuan, *Nano Energy*, 2019, **65**, 104058.
209 M. Dai, Z. Wang, F. Wang, Y. Qiu, J. Zhang, C.-Y. Xu, T. Zhai, W. Cao, Y. Fu, D. Jia, Y. Zhou and P.-A. Hu, *Nano Lett.*, 2019, **19**, 5410–5416.
210 F. Xue, J. Zhang, W. Hu, W.-T. Hsu, A. Han, S.-F. Leung, J.-K. Huang, Y. Wan, S. Liu, J. Zhang, J.-H. He, W.-H. Chang, Z. L. Wang, X. Zhang and L.-J. Li, *ACS Nano*, 2018, **12**, 4976–4983.
211 M. Dai, H. Chen, F. Wang, Y. Hu, S. Wei, J. Zhang, Z. Wang, T. Zhai and P. Hu, *ACS Nano*, 2019, **13**, 7291–7299.
212 Z. L. Wang and A. C. Wang, *Mater. Today*, 2019, **30**, 34–51.
213 X. Zhang, L. Chen, Y. Jiang, W. Lim and S. Soh, *Chem. Mater.*, 2019, **31**, 1473–1478.
214 H. Zou, Y. Zhang, L. Guo, P. Wang, X. He, G. Dai, H. Zheng, C. Chen, A. C. Wang, C. Xu and Z. L. Wang, *Nat. Commun.*, 2019, **10**, 1–9.
215 J. Liu, F. Liu, R. Bao, K. Jiang, F. Khan, Z. Li, H. Peng, J. Chen, A. Alodhayb and T. Thundat, *ACS Appl. Mater. Interfaces*, 2019, **11**, 35404–35409.
216 C. Wu, T. W. Kim and H. Y. Choi, *Nano Energy*, 2017, **32**, 542–550.
217 K. Hippalgaonkar, Y. Wang, Y. Ye, D. Y. Qiu, H. Zhu, Y. Wang, J. Moore, S. G. Louie and X. Zhang, *Phys. Rev. B*, 2017, **95**, 115407.
218 G. Tan, L.-D. Zhao and M. G. Kanatzidis, *Chem. Rev.*, 2016, **116**, 12123–12149.
219 F. J. DiSalvo, *Science*, 1999, **285**, 703–706.
220 C. B. Vining, *Nat. Mater.*, 2009, **8**, 83–85.
221 A. A. Balandin, *Nat. Mater.*, 2011, **10**, 569–581.
222 A. J. Minnich, *Phys. Rev. B: Condens. Matter Mater. Phys.*, 2015, **91**, 085206.
223 L. Liang, E. Cruz-Silva, E. C. Girão and V. Meunier, *Phys. Rev. B: Condens. Matter Mater. Phys.*, 2012, **86**, 115438.
224 J. Y. Kim and J. C. Grossman, *Nano Lett.*, 2015, **15**, 2830–2835.
225 Y. Anno, Y. Imakita, K. Takei, S. Akita and T. Arie, *2D Mater.*, 2017, **4**, 025019.
226 Q.-Y. Li, T. Feng, W. Okita, Y. Komori, H. Suzuki, T. Kato, T. Kaneko, T. Ikuta, X. Ruan and K. Takahashi, *ACS Nano*, 2019, **13**, 9182–9189.
227 S.-G. Nam, D.-K. Ki and H.-J. Lee, *Phys. Rev. B: Condens. Matter Mater. Phys.*, 2010, **82**, 245416.
228 H. Sevinçli and G. Cuniberti, *Phys. Rev. B: Condens. Matter Mater. Phys.*, 2010, **81**, 113401.
229 T. Gunst, T. Markussen, A.-P. Jauho and M. Brandbyge, *Phys. Rev. B: Condens. Matter Mater. Phys.*, 2011, **84**, 155449.
230 M. B. Lundeberg, Y. Gao, A. Woessner, C. Tan, P. Alonso-González, K. Watanabe, T. Taniguchi, J. Hone, R. Hillenbrand and F. H. L. Koppens, *Nat. Mater.*, 2017, **16**, 204–207.
231 B. S. Lee, *J. Phys.: Condens. Matter*, 2018, **30**, 295302.
232 W. Zeng, X.-M. Tao, S. Lin, C. Lee, D. Shi, K. Lam, B. Huang, Q. Wang and Y. Zhao, *Nano Energy*, 2018, **54**, 163–174.
233 D. Guo, C. Li, K. Qiu, Q. Yang, K. Li, B. Shao, D. Chen, Y. Ma, J. Sun, X. Cao, W. Zeng, Z. Wang and R. Xie, *J. Alloys Compd.*, 2019, **810**, 151838.
234 H. Sevinçli, C. Sevik, T. Caın and G. Cuniberti, *Sci. Rep.*, 2013, **3**, 1228.
235 R. Yan, J. R. Simpson, S. Bertolazzi, J. Brivio, M. Watson, X. Wu, A. Kis, T. Luo, A. R. Hight Walker and H. G. Xing, *ACS Nano*, 2014, **8**, 986–993.
236 S. Sahoo, A. P. S. Gaur, M. Ahmadi, M. J.-F. Guinel and R. S. Katiyar, *J. Phys. Chem. C*, 2013, **117**, 9042–9047.
237 A. Molina-Sánchez and L. Wirtz, *Phys. Rev. B: Condens. Matter Mater. Phys.*, 2011, **84**, 155413.
238 X. Li, J. Zhang, A. A. Puretzky, A. Yoshimura, X. Sang, Q. Cui, Y. Li, L. Liang, A. W. Ghosh, H. Zhao, R. R. Unocic, V. Meunier, C. M. Rouleau, B. G. Sumpter, D. B. Geohegan and K. Xiao, *ACS Nano*, 2019, **13**, 2481–2489.
239 M. Yarali, X. Wu, T. Gupta, D. Ghoshal, L. Xie, Z. Zhu, H. Brahmi, J. Bao, S. Chen, T. Luo, N. Koratkar and A. Mavrokefalos, *Adv. Funct. Mater.*, 2017, **27**, 1704357.
240 Y. Cai, J. Lan, G. Zhang and Y.-W. Zhang, *Phys. Rev. B: Condens. Matter Mater. Phys.*, 2014, **89**, 035438.
241 X. Liu, G. Zhang, Q.-X. Pei and Y.-W. Zhang, *Appl. Phys. Lett.*, 2013, **103**, 133113.
242 A. Jain and A. J. H. McGaughey, *Sci. Rep.*, 2015, **5**, 1–5.
243 R. Fei, A. Faghaninia, R. Soklaski, J.-A. Yan, C. Lo and L. Yang, *Nano Lett.*, 2014, **14**, 6393–6399.
244 B. Smith, B. Vermeersch, J. Carrete, E. Ou, J. Kim, N. Mingo, D. Akinwande and L. Shi, *Adv. Mater.*, 2017, **29**, 1603756.
245 Y. Saito, T. Iizuka, T. Koretsune, R. Arita, S. Shimizu and Y. Iwasa, *Nano Lett.*, 2016, **16**, 4819–4824.
246 C. J. An, Y. H. Kang, C. Lee and S. Y. Cho, *Adv. Funct. Mater.*, 2018, **28**, 1800532.
247 J. Zhang, H. J. Liu, L. Cheng, J. Wei, J. H. Liang, D. D. Fan, P. H. Jiang, L. Sun and J. Shi, *J. Mater. Chem. C*, 2016, **4**, 991–998.
248 L.-D. Zhao, S.-H. Lo, Y. Zhang, H. Sun, G. Tan, C. Uher, C. Wolverton, V. P. Dravid and M. G. Kanatzidis, *Nature*, 2014, **508**, 373–377.
249 A. T. Duong, V. Q. Nguyen, G. Duvjir, V. T. Duong, S. Kwon, J. Y. Song, J. K. Lee, J. E. Lee, S. Park, T. Min, J. Lee, J. Kim and S. Cho, *Nat. Commun.*, 2016, **7**, 1–6.
250 S. Sassi, C. Candolfi, J.-B. Vaney, V. Ohorodniichuk, P. Masschelein, A. Dauscher and B. Lenoir, *Appl. Phys. Lett.*, 2014, **104**, 212105.
251 X.-L. Shi, X. Tao, J. Zou and Z.-G. Chen, *Adv. Sci.*, 2020, **7**, 1902923.
252 J. Liu, P. Wang, M. Wang, R. Xu, J. Zhang, J. Liu, D. Li, N. Liang, Y. Du, G. Chen and G. Tang, *Nano Energy*, 2018, **53**, 683–689.
253 H. Jin, C. Guo, X. Liu, J. Liu, A. Vasileff, Y. Jiao, Y. Zheng and S.-Z. Qiao, *Chem. Rev.*, 2018, **118**, 6337–6408.
254 B. Luo, G. Liu and L. Wang, *Nanoscale*, 2016, **8**, 6904–6920.
255 X. Wang, K. Maeda, A. Thomas, K. Takanabe, G. Xin, J. M. Carlsson, K. Domen and M. Antonietti, *Nat. Mater.*, 2009, **8**, 76–80.
256 J. K. Nørskov, T. Bligaard, A. Logadottir, J. R. Kitchin, J. G. Chen, S. Pandelov and U. Stimming, *J. Electrochem. Soc.*, 2005, **152**, J23–J26.

257 B. Hinnemann, P. G. Moses, J. Bonde, K. P. Jørgensen, J. H. Nielsen, S. Horch, I. Chorkendorff and J. K. Nørskov, *J. Am. Chem. Soc.*, 2005, **127**, 5308–5309.
258 T. F. Jaramillo, K. P. Jørgensen, J. Bonde, J. H. Nielsen, S. Horch and I. Chorkendorff, *Science*, 2007, **317**, 100–102.
259 H. Li, H. Wu, S. Yuan and H. Qian, *Sci. Rep.*, 2016, **6**, 21171.
260 K. Sekar, G. Raji, L. Tong, Y. Zhu, S. Liu and R. Xing, *Appl. Surf. Sci.*, 2020, **504**, 144441.
261 R. K. Chava, J. Y. Do and M. Kang, *Appl. Surf. Sci.*, 2018, **433**, 240–248.
262 X. Liu, L. Liu, Y. Wu, Y. Wang, J. Yang and Z. Wang, *RSC Adv.*, 2019, **9**, 13820–13828.
263 G. Liao, Y. Gong, L. Zhang, H. Gao, G.-J. Yang and B. Fang, *Energy Environ. Sci.*, 2019, **12**, 2080–2147.
264 K.-T. Lin, H. Lin, T. Yang and B. Jia, *Nat. Commun.*, 2020, **11**, 1–10.
265 T. Xu, X. Ding, C. Shao, L. Song, T. Lin, X. Gao, J. Xue, Z. Zhang and L. Qu, *Small*, 2018, **14**, 1704473.
266 NiS and graphene as dual cocatalysts for the enhanced photocatalytic H2 production activity of g-C_3N_4 – ScienceDirect, https://www.sciencedirect.com/science/article/pii/S016943321833023X, accessed February 4, 2020.
267 C. Fan, Q. Feng, G. Xu, J. Lv, Y. Zhang, J. Liu, Y. Qin and Y. Wu, *Appl. Surf. Sci.*, 2018, **427**, 730–738.
268 J. Fu, B. Zhu, C. Jiang, B. Cheng, W. You and J. Yu, *Small*, 2017, **13**, 1603938.
269 Y. Wang, J. Zhang, X. Wang, M. Antonietti and H. Li, *Angew. Chem., Int. Ed.*, 2010, **49**, 3356–3359.
270 J. Ran, T. Yi Ma, G. Gao, X.-W. Du and S. Zhang Qiao, *Energy Environ. Sci.*, 2015, **8**, 3708–3717.
271 J. Fu, Q. Xu, J. Low, C. Jiang and J. Yu, *Appl. Catal., B*, 2019, **243**, 556–565.
272 L. Xu, W.-Q. Huang, L.-L. Wang, Z.-A. Tian, W. Hu, Y. Ma, X. Wang, A. Pan and G.-F. Huang, *Chem. Mater.*, 2015, **27**, 1612–1621.
273 G. Liao, Y. Gong, L. Zhang, H. Gao, G.-J. Yang and B. Fang, *Energy Environ. Sci.*, 2019, **12**, 2080–2147.
274 D. Lu, H. Fan, K. K. Kondamareddy, H. Yu, A. Wang, H. Hao, M. Li and J. Shen, *ACS Sustainable Chem. Eng.*, 2018, **6**, 9903–9911.
275 Y. Cai, J. Gao, S. Chen, Q. Ke, G. Zhang and Y.-W. Zhang, *Chem. Mater.*, 2019, **31**, 8948–8956.
276 B. Tian, B. Tian, B. Smith, M. C. Scott, R. Hua, Q. Lei and Y. Tian, *Nat. Commun.*, 2018, **9**, 1–11.
277 H. Wang, S. Jiang, W. Shao, X. Zhang, S. Chen, X. Sun, Q. Zhang, Y. Luo and Y. Xie, *J. Am. Chem. Soc.*, 2018, **140**, 3474–3480.
278 M. Zhu, S. Kim, L. Mao, M. Fujitsuka, J. Zhang, X. Wang and T. Majima, *J. Am. Chem. Soc.*, 2017, **139**, 13234–13242.
279 J. Ran, B. Zhu and S.-Z. Qiao, *Angew. Chem., Int. Ed.*, 2017, **56**, 10373–10377.
280 J. D. Wood, S. A. Wells, D. Jariwala, K.-S. Chen, E. Cho, V. K. Sangwan, X. Liu, L. J. Lauhon, T. J. Marks and M. C. Hersam, *Nano Lett.*, 2014, **14**, 6964–6970.
281 J. Pei, X. Gai, J. Yang, X. Wang, Z. Yu, D.-Y. Choi, B. Luther-Davies and Y. Lu, *Nat. Commun.*, 2016, **7**, 1–8.
282 Y. Y. Illarionov, M. Waltl, G. Rzepa, J.-S. Kim, S. Kim, A. Dodabalapur, D. Akinwande and T. Grasser, *ACS Nano*, 2016, **10**, 9543–9549.
283 J. Hu, D. Chen, Z. Mo, N. Li, Q. Xu, H. Li, J. He, H. Xu and J. Lu, *Angew. Chem., Int. Ed.*, 2019, **58**, 2073–2077.
284 W. Hu, L. Lin, R. Zhang, C. Yang and J. Yang, *J. Am. Chem. Soc.*, 2017, **139**, 15429–15436.
285 Z. Xie, Y. Duo, Z. Lin, T. Fan, C. Xing, L. Yu, R. Wang, M. Qiu, Y. Zhang, Y. Zhao, X. Yan and H. Zhang, *Adv. Sci.*, 2020, **7**, 1902236.
286 S. Liu, X. Pan and H. Liu, *Angew. Chem., Int. Ed.*, 2020, **59**, 5890–5900.
287 D. Jaque, L. Martínez Maestro, B. del Rosal, P. Haro-Gonzalez, A. Benayas, J. L. Plaza, E. Martín Rodríguez and J. García Solé, *Nanoscale*, 2014, **6**, 9494–9530.
288 Z. Sun, H. Xie, S. Tang, X.-F. Yu, Z. Guo, J. Shao, H. Zhang, H. Huang, H. Wang and P. K. Chu, *Angew. Chem., Int. Ed.*, 2015, **54**, 11526–11530.
289 J. Shao, H. Xie, H. Huang, Z. Li, Z. Sun, Y. Xu, Q. Xiao, X.-F. Yu, Y. Zhao, H. Zhang, H. Wang and P. K. Chu, *Nat. Commun.*, 2016, **7**, 1–13.
290 G. Yang, Z. Liu, Y. Li, Y. Hou, X. Fei, C. Su, S. Wang, Z. Zhuang and Z. Guo, *Biomater. Sci.*, 2017, **5**, 2048–2055.
291 K. Yang, S. Zhang, G. Zhang, X. Sun, S.-T. Lee and Z. Liu, *Nano Lett.*, 2010, **10**, 3318–3323.
292 J. T. Robinson, S. M. Tabakman, Y. Liang, H. Wang, H. Sanchez Casalongue, D. Vinh and H. Dai, *J. Am. Chem. Soc.*, 2011, **133**, 6825–6831.
293 K. Yang, J. Wan, S. Zhang, B. Tian, Y. Zhang and Z. Liu, *Biomaterials*, 2012, **33**, 2206–2214.
294 H. Lin, X. Wang, L. Yu, Y. Chen and J. Shi, *Nano Lett.*, 2017, **17**, 384–391.
295 T. Liu, C. Wang, X. Gu, H. Gong, L. Cheng, X. Shi, L. Feng, B. Sun and Z. Liu, *Adv. Mater.*, 2014, **26**, 3433–3440.
296 R. Li, L. Zhang, L. Shi and P. Wang, *ACS Nano*, 2017, **11**, 3752–3759.
297 M. Macha, S. Marion, V. V. R. Nandigana and A. Radenovic, *Nat. Rev. Mater.*, 2019, **4**, 588–605.
298 M. Graf, M. Lihter, D. Unuchek, A. Sarathy, J.-P. Leburton, A. Kis and A. Radenovic, *Joule*, 2019, **3**, 1549–1564.
299 W. Xu, H. Zheng, Y. Liu, X. Zhou, C. Zhang, Y. Song, X. Deng, M. Leung, Z. Yang, R. X. Xu, Z. L. Wang, X. C. Zeng and Z. Wang, *Nature*, 2020, **578**, 392–396.
300 Y. Wang, S. Gao, W. Xu and Z. Wang, *Adv. Funct. Mater.*, 2020, **30**, 1908252.
301 W. Tang, B. D. Chen and Z. L. Wang, *Adv. Funct. Mater.*, 2019, **29**, 1901069.
302 S. Yang, Y. Su, Y. Xu, Q. Wu, Y. Zhang, M. B. Raschke, M. Ren, Y. Chen, J. Wang, W. Guo, Y. Ron Shen and C. Tian, *J. Am. Chem. Soc.*, 2018, **140**, 13746–13752.
303 G. L. Stephens, J. Li, M. Wild, C. A. Clayson, N. Loeb, S. Kato, T. L'Ecuyer, P. W. Stackhouse, M. Lebsock and T. Andrews, *Nat. Geosci.*, 2012, **5**, 691–696.
304 G. Xue, Y. Xu, T. Ding, J. Li, J. Yin, W. Fei, Y. Cao, J. Yu, L. Yuan, L. Gong, J. Chen, S. Deng, J. Zhou and W. Guo, *Nat. Nanotechnol.*, 2017, **12**, 317–321.

305 J. Yin, Z. Zhang, X. Li, J. Yu, J. Zhou, Y. Chen and W. Guo, *Nat. Commun.*, 2014, **5**, 3582.
306 F.-R. Fan, Z.-Q. Tian and Z. Lin Wang, *Nano Energy*, 2012, **1**, 328–334.
307 Z. L. Wang, *ACS Nano*, 2013, **7**, 9533–9557.
308 S. A. Han, T.-H. Kim, S. K. Kim, K. H. Lee, H.-J. Park, J.-H. Lee and S.-W. Kim, *Adv. Mater.*, 2018, **30**, 1800342.
309 X. Wang, H. Tian, W. Xie, Y. Shu, W.-T. Mi, M. Ali Mohammad, Q.-Y. Xie, Y. Yang, J.-B. Xu and T.-L. Ren, *NPG Asia Mater.*, 2015, **7**, e154–e154.
310 Y. Liu, L. Zhao, L. Wang, H. Zheng, D. Li, R. Avila, K. W. C. Lai, Z. Wang, Z. Xie, Y. Zi and X. Yu, *Adv. Mater. Technol.*, 2019, **4**, 1900744.
311 Y. Zhang, H. Kim, Q. Wang, W. Jo, A. I. Kingon, S.-H. Kim and C. K. Jeong, *Nanoscale Adv.*, 2020, **2**, 3131–3149.
312 G.-J. Lee, M.-K. Lee, J.-J. Park, D. Y. Hyeon, C. K. Jeong and K.-I. Park, *ACS Appl. Mater. Interfaces*, 2019, **11**, 37920–37926.
313 J. K. Han, *Appl. Surf. Sci.*, 2021, **538**, 147962.
314 H. Khan, N. Mahmood, A. Zavabeti, A. Elbourne, Md. A. Rahman, B. Y. Zhang, V. Krishnamurthi, P. Atkin, M. B. Ghasemian, J. Yang, G. Zheng, A. R. Ravindran, S. Walia, L. Wang, S. P. Russo, T. Daeneke, Y. Li and K. Kalantar-Zadeh, *Nat. Commun.*, 2020, **11**, 3449.
315 S. Tiwari, *Sustainable Energy Fuels*, 2020, **4**, 2469.
316 Y. Dong, S. S. K. Mallineni, K. Maleski, H. Behlow, V. N. Mochalin, A. M. Rao, Y. Gogotsi and R. Podila, *Nano Energy*, 2018, **44**, 103–110.
317 Z. Yang, F. Dang, C. Zhang, S. Sun, W. Zhao, X. Li, Y. Liu and X. Chen, *Langmuir*, 2019, **35**, 7713–7719.
318 S. Feng, T. Yao, Y. Lu, Z. Hao and S. Lin, *Nano Energy*, 2019, **58**, 63–68.
319 J. Semple, D. G. Georgiadou, G. Wyatt-Moon, G. Gelinck and T. D. Anthopoulos, *Semicond. Sci. Technol.*, 2017, **32**, 123002.
320 F. R. Fan and W. Wu, *Research*, 2019, **2019**, 1–16.
321 G. S. Gund, M. G. Jung, K.-Y. Shin and H. S. Park, *ACS Nano*, 2019, **13**, 14114–14121.
322 M. Han, Y. Liu, R. Rakhmanov, C. Israel, M. A. S. Tajin, G. Friedman, V. Volman, A. Hoorfar, K. R. Dandekar and Y. Gogotsi, *Adv. Mater.*, 2020, 2003225.
323 S. J. Yang, K.-T. Park, J. Im, S. Hong, Y. Lee, B.-W. Min, K. Kim and S. Im, *Nat. Commun.*, 2020, **11**, 1574.
324 Y. Yu, J. Nassar, C. Xu, J. Min, Y. Yang, A. Dai, R. Doshi, A. Huang, Y. Song, R. Gehlhar, A. D. Ames and W. Gao, *Sci. Rob.*, 2020, **5**, eaaz7946.
325 I. Mathews, S. Sofia, E. Ma, J. Jean, H. S. Laine, S. C. Siah, T. Buonassisi and I. M. Peters, *Joule*, 2020, **4**, 822–839.
326 S. Park, T. Kim, S. Yoon, C. W. Koh, H. Y. Woo and H. J. Son, *Adv. Mater.*, 2020, 2002217.
327 Y. Cui, Y. Wang, J. Bergqvist, H. Yao, Y. Xu, B. Gao, C. Yang, S. Zhang, O. Inganäs, F. Gao and J. Hou, *Nat. Energy*, 2019, **4**, 768–775.
328 Y. Firdaus, V. M. Le Corre, J. I. Khan, Z. Kan, F. Laquai, P. M. Beaujuge and T. D. Anthopoulos, *Adv. Sci.*, 2019, **6**, 1802028.
329 Q. Liu, Y. Jiang, K. Jin, J. Qin, J. Xu, W. Li, J. Xiong, J. Liu, Z. Xiao, K. Sun, S. Yang, X. Zhang and L. Ding, *Sci. Bull.*, 2020, **65**, 272–275.
330 N. Park, *Adv. Energy Mater.*, 2020, **10**, 1903106.
331 J. Y. Kim, J.-W. Lee, H. S. Jung, H. Shin and N.-G. Park, *Chem. Rev.*, 2020, **120**, 7867–7918.
332 S. Razza, S. Castro-Hermosa, A. Di Carlo and T. M. Brown, *APL Mater.*, 2016, **4**, 091508.
333 A. E. Shalan, *Mater. Adv.*, 2020, **1**, 292–309.
334 F. Wang, Y. Cao, C. Chen, Q. Chen, X. Wu, X. Li, T. Qin and W. Huang, *Adv. Funct. Mater.*, 2018, **28**, 1803753.
335 H. S. Jung, G. S. Han, N.-G. Park and M. J. Ko, *Joule*, 2019, **3**, 1850–1880.
336 L. Qiu, S. He, L. K. Ono, S. Liu and Y. Qi, *ACS Energy Lett.*, 2019, **4**, 2147–2167.
337 Q.-Q. Chu, B. Ding, J. Peng, H. Shen, X. Li, Y. Liu, C.-X. Li, C.-J. Li, G.-J. Yang, T. P. White and K. R. Catchpole, *J. Mater. Sci. Technol.*, 2019, **35**, 987–993.
338 G. Grancini, C. Roldán-Carmona, I. Zimmermann, E. Mosconi, X. Lee, D. Martineau, S. Narbey, F. Oswald, F. De Angelis, M. Graetzel and M. K. Nazeeruddin, *Nat. Commun.*, 2017, **8**, 15684.
339 G. Grancini and M. K. Nazeeruddin, *Nat. Rev. Mater.*, 2019, **4**, 4–22.
340 J. Xu, C. C. Boyd, Z. J. Yu, A. F. Palmstrom, D. J. Witter, B. W. Larson, R. M. France, J. Werner, S. P. Harvey, E. J. Wolf, W. Weigand, S. Manzoor, M. F. A. M. van Hest, J. J. Berry, J. M. Luther, Z. C. Holman and M. D. McGehee, *Science*, 2020, **367**, 1097–1104.
341 S. M. Holmes, P. Balakrishnan, V. S. Kalangi, X. Zhang, M. Lozada-Hidalgo, P. M. Ajayan and R. R. Nair, *Adv. Energy Mater.*, 2017, **7**, 1601216.
342 P. Balakrishnan and S. Holmes, *Fuel Cells Bull.*, 2017, **2017**, 14.
343 S. I. Yoon, K. Y. Ma, T.-Y. Kim and H. S. Shin, *J. Mater. Chem. A*, 2020, **8**, 2898–2912.
344 M. Perez-Page, M. Sahoo and S. M. Holmes, *Adv. Mater. Interfaces*, 2019, **6**, 1801838.
345 F. Moghadam and H. B. Park, *2D Mater.*, 2019, **6**, 042002.
346 T. Yu, *J. Electrochem. Soc.*, 2020, **167**, 126502.
347 G. Bai, C. Liu, Z. Gao, B. Lu, X. Tong, X. Guo and N. Yang, *Small*, 2019, **15**, 1902951.
348 G. C. Yoon, K.-S. Shin, M. K. Gupta, K. Y. Lee, J.-H. Lee, Z. L. Wang and S.-W. Kim, *Nano Energy*, 2015, **12**, 547–555.
349 T. Reiss, K. Hjelt and A. C. Ferrari, *Nat. Nanotechnol.*, 2019, **14**, 907–910.

